Molecular motors

Fernández Landaluce, Tatiana

Molecular Motors:
From Solution to Surfaces

Tatiana Fernández Landaluce

Molecular Motors: From Solution to Surfaces

Tatiana Fernández Landaluce
Ph.D. thesis
University of Groningen, The Netherlands

Cover design by Desirée Fernández Landaluce (Landadesign@hotmail.com)
Cover explanation:
Portada basada en el libro “El ingenioso hidalgo Don Quijote de La Mancha” escrito por Miguel de Cervantes Saavedra. En la portada Don Quijote lucha contra unos gigantes, que no son otra cosa que molinos de viento.
Cover based on the book “The ingenious gentleman Don Quixote of La Mancha” written by Miguel de Cervantes Saavedra. The cover shows Don Quixote's attack on windmills that he believes to be ferocious giants.

Zernike Institute Ph.D. Thesis series 2013-10
ISSN 1570-1530
ISBN: 978-90-367-6198-7 (printed version)
ISBN: 978-90-367-6197-0 (electronic version)

This work was performed within “Top Research School” program of the Zernike Institute for Advanced Materials under the Bonus Incentive Scheme (BIS) of the Netherlands’ Ministry of Education, Science, and Culture and received additional support from the 'Stichting voor Fundamenteel Onderzoek der Materie (FOM)', which is financially supported by the 'Nederlandse Organisatie voor Wetenschappelijk Onderzoek (NWO)'.
Printed by: Ipskamp Drukkers B.V. Enschede, The Netherlands

RIJKSUNIVERSITEIT GRONINGEN

Molecular Motors: From Solution to Surfaces

Proefschrift

ter verkrijging van het doctoraat in de

Wiskunde en Natuurwetenschappen

aan de Rijksuniversiteit Groningen

op gezag van de

Rector Magnificus, Prof. Dr. E. Sterken,

in het openbaar te verdedigen op

vrijdag 24 mei 2013

om 12:45 uur

door

Tatiana Fernández Landaluce

geboren op 18 juni 1979

te Bilbao, Spanje

Promotores:	Prof. dr. P. Rudolf
	Prof. dr. B. L. Feringa
Beoordelingscommissie:	Prof. dr. K. J. Franke
	Prof. dr. S. De Feyter
	Prof. dr. W.J. Buma

Es fácil pensar en las cosas importantes de la vida, son las que siempre están ahí. Son las luces que iluminan mi camino, un camino a veces fácil y otras veces difícil. Pero el camino no es el importante, son las luces que te guían, te aconsejan y te enseñan. Sin esas luces no soy nada.

Para dos luces especiales, únicas, de esas que lo iluminan todo.

A mis abuelas Aurora y Oliva.

Contents

Chapter 1

Introduction

What is so special about nanotechnology and how can we apply it? In this chapter we will explain what nanotechnology is and we will go through the different events in history that have influence the development of this growing field. We will show various examples of nature-inspired nanotechnology systems, from rotaxanes to light-driven molecular motors. Several methods for surface-grafting of molecular motors on surfaces will be described, to control these systems in a way that preserves the possibility of movement at the molecular level.

1.1 What is Nanoscience?

The word nanotechnology comes from the word *nano* which is a prefix meaning one-billionth of something; this prefix derives from the Ancient Greek word for 'dwarf' (*nanos*). One nanometer is one-millionth of a millimeter (10^{-9} m). One may get a feeling for how small a nanometer is if one thinks of the relationship shown in Figure 1.1: the ratio between the diameters of a nanometer-sized object like a fullerene molecule and a football is about the same as that of a football compared and the earth.

Figure 1.1. Illustration of size relationships between a fullerene molecule, a football and the earth.

"Nanoscience is the study of phenomena and manipulation of materials at atomic, molecular and macromolecular scales, where properties differ significantly from those at a larger scale. Nanotechnology is the design, characterization, production and application of structures, devices and systems by controlling shape and size at the nanometer scale [1]." "Nanotechnology is (a) the creation of useful materials, devices, and systems through the control of matter on the nanometer -length scale, and (b) the exploitation of novel properties and phenomena developed at that scale [2]." "Molecular nanotechnology: Thorough, inexpensive control of the structure of matter based on molecule-by-molecule control of products and byproducts of molecular manufacturing [3]."

The beginning of nanoscience can be identified with the lecture entitled "Plenty of Room at the Bottom" given by the physicist Richard Feynman at an American Physical Society meeting at Caltech on December 29th, 1959, where he said "In my view, the principles of physics do not speak against the possibility of manoeuvring things atom by atom", thereby introducing a new concept, the control and manipulation of matter at the atomic scale [4]. For the next twenty years this concept remained at the level of "Gedankenexperiment" which for example inspired von Neumann in 1966 to study the possibility of creating systems that are self-replicating as a way to reduce costs [5]. The great breakthrough came in the 1980s when scanning tunneling microscopy (1981) and

atomic force microscopy (1986) were invented and it became possible to “see” and manipulate matter at the atomic scale [6,7]. In 1981 there was also an important conceptual advancement by Eric Drexler’s book “Molecular Engineering” [8], claiming that with molecular nanotechnology based on molecular machines it would be possible to build objects to complex atomic specifications.

While mankind still bases its engineering efforts on static or equilibrium properties of materials, nature employs nanomotors and molecular machines for essentially every significant biological process: from photosynthesis to energy storage, information transfer or chemical transport in cells, between cells and outside cells, replication, transcription, movement of muscles, etc. The molecular motors or molecular machines like myosins, kinesins and dyneins are proteins and protein assemblies that perform special motions in response to biological stimuli [9-13]. These proteins can move back and forth on actin filaments or microtubules transporting substrates while fuelled by ATP (adenosine triphosphate) [10-13].

If one wants to take inspiration from this dynamic way of realizing function and construct artificial systems as envisioned by Drexler, special strategies have to be developed to face the challenges that come with task performance via controlled molecular-level motion, and in particular with interfacing the dynamics of synthetic molecular motors and switches with the macroscopic world. This nature-inspired approach certainly has the potential to revolutionize every aspect of functional molecule and materials design [14]. In fact, molecular motors are fundamentally different from the macroscopic motors we use in our daily life: not only are they soft, work at room temperature and at surfaces or in solution, their components are also constantly in motion. This implies the need to control their directionality of movement by architectures which restrict the degrees of freedom. I shall illustrate this with a wholly synthetic molecular system that converts external energy (light) into biased Brownian motion to transport a macroscopic cargo and do measurable work [15]. The millimeter-scale directional transport of a liquid on a surface, illustrated in Figure 1.2, is achieved by using the biased Brownian motion of stimuli-responsive rotaxanes (‘molecular shuttles’). Rotaxanes are macromolecules consisting of two parts: a stiff bar-like part and a ring-shaped part, arranged around the bar. Due to hydrogen-bonding interactions, the ring prefers a distinct position but photoisomerization of the interacting part of the bar can disrupt the hydrogen bonding at the preferred site and thereby induce the ring to shift to another position. This concept was used in this example to expose or conceal fluoroalkane moieties and thereby modify surface tension. When a droplet of liquid is placed on a surface covered by rotaxanes exposing fluoroalkane moieties, the droplet does not wet the surface. If the surface in front of the droplet is then illuminated with UV light, the rotaxanes on the surface will photoisomerize and this induces a change in conformation, which conceals the fluoroalkane moieties. This creates a gradient in surface tension which will make the droplet move forward or uphill as illustrated in the

photographs of figure 1.2. The change in free energy made available by the nanometer movements of the individual machine parts is thereby transformed into work against gravity and viscous forces.

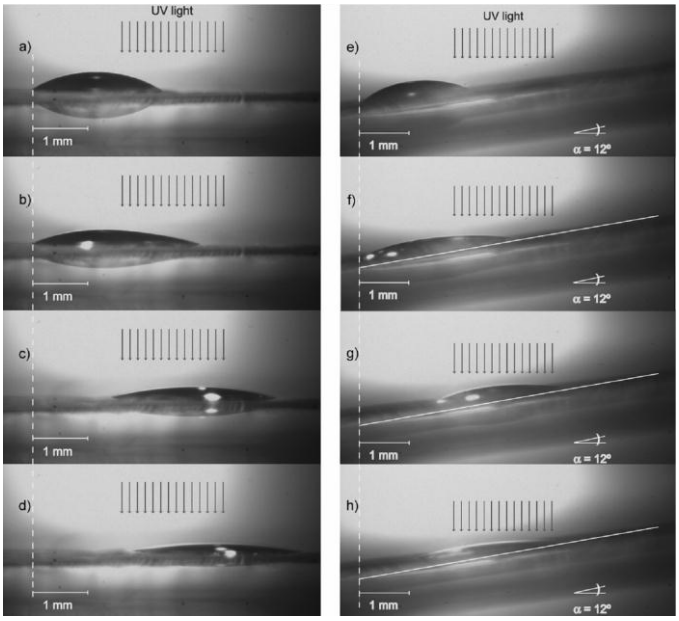

Figure 1.2. Photographs of light-driven directional transport of a 1.25 µl diiodomethane drop across the surface of a monolayer of fluorinated rotaxane on gold/mica, both horizontally (a)-(d) and up a twelve degree incline (e)-(h) [15].

Another light-driven system is the "Irie" switch, shown in Figure 1.3, a molecule which is light sensitive and can be opened or closed by two different frequencies. These diarylethenes have a high thermodynamic stability. Ring opening occurs under UV light and ring closure by light with a wavelength >600 nm [16]. In principle switching processes induced by light are easily managed compared to those using extensive and complicated chemistry.

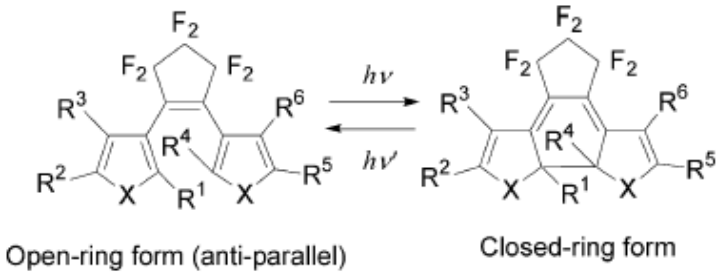

Figure 1.3. The diarylethene derivatives undergo cyclization/cycloreversion photochromic reactions upon photoirradiation [17].

Several artificial molecular machines with non-biological components have been developed during the past 3 decades. For instance, a general method to create molecular motors is the photoisomerization of substituted alkenes, provided that the process is

reversible and the two isomers are kinetically stable [18]. Koumura *et al.* found that two light-induced cis-trans isomerizations are each associated with a 180° rotation around the carbon-carbon double bond, an example is shown in Figure 1.4, where the four bulky substituents are responsible for an energy barrier at -55°C between the trans and cis configurations [18].

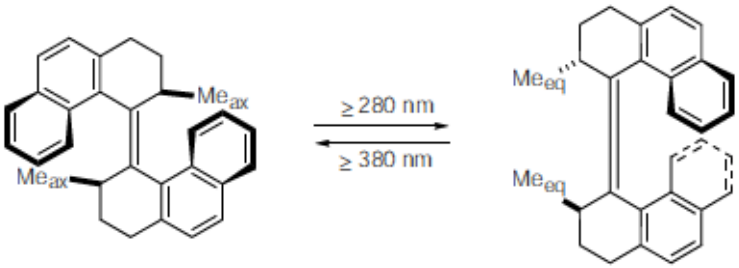

Figure 1.4. Scheme of a tetrasubstituted alkene acting as molecular motor by photoinduced isomerization [18].

These light-driven molecular motors introduced by Feringa and co-workers open the possibility of realization of a real molecular motor machine. Research has been carried out to improve the performance of these challenging systems: acceleration studies to further increases in rotation speed [19-28], but most important immobilization or anchoring investigation so that these systems can perform useful work [29-32]. In this thesis we will show the latest results to achieve anchoring of light-driven molecular motors onto surfaces.

1.2 Surface-grafting of molecular motors

A major challenge for realizing functional surfaces based on molecular motors which can be addressed with external stimuli is to anchor the motor molecules in a way that preserves the possibility of movement at the molecular level. Two different approaches are possible, either the motor is functionalized with anchoring groups that maintain it at a certain distance from the surface while assuring a stable fixation via a chemical bond, or the motor is grafted on a dense monolayer of molecules previously assembled on the surface. For the first approach several strategies can be followed depending on the type of substrate one wishes to employ as illustrated in Figure 1.5.

The second approach relies on self-assembled monolayers (SAMs) which have become a key factor of surface science research over the past decades due to their unique, highly organized structures in a wide range of chemical compositions and different substrate materials [33]. The two most widely used groups of self-assembled monolayers are alkanethiolate films on metal surfaces (Au, Ag, Cu) [34,35] and alkylsiloxane monolayers on hydroxylated oxide surfaces (SiO_2/Si, glass, metal oxides, etc) [36,37].

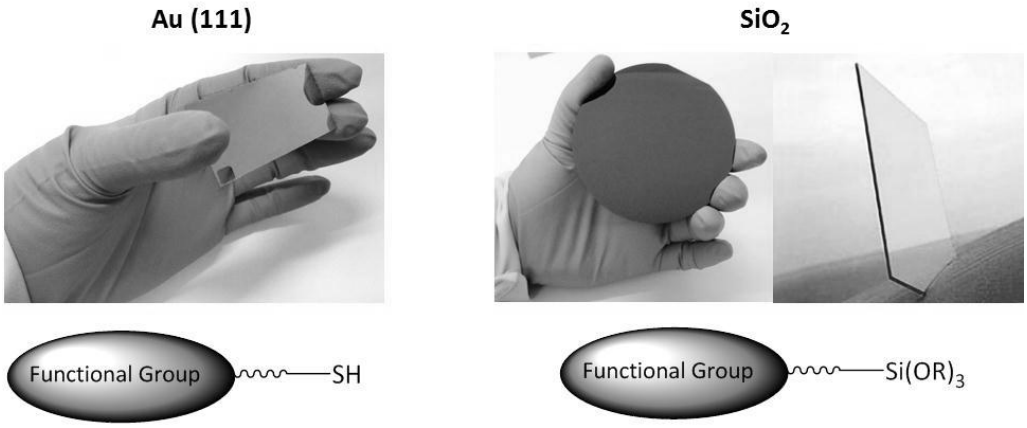

Figure 1.5. Schematic representation of anchoring groups that can be used to fix functional units to gold (left) and silicon oxide surfaces (right).

A self-assembled monolayer is a single layer of ordered molecules absorbed on a substrate due to bonding between the surface and the molecular head group as illustrated in Figure 1.6.

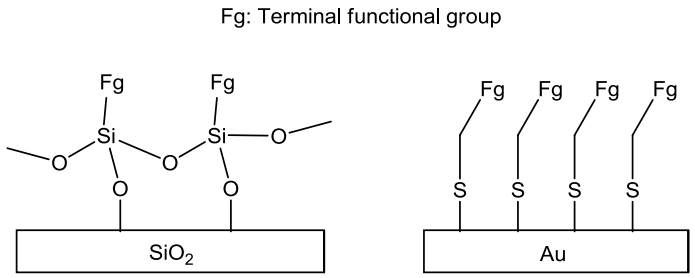

Figure 1.6. Self-assembled monolayer on silicon oxide (left) and on gold surface (right).

One example of a self-assembling molecule is shown in Figure 1.7. The *head group* is selected to specifically chemisorb on the surface of the substrate. Depending on the substrate where the self-assembled monolayer adsorbs, the molecule should contain a certain head group (*i.e.* self-assembled monolayers of silane-functionalized molecules on a silicon oxide surface and of thiol-functionalized molecules on a gold surface). The *hydrocarbon* generally comprises an alkyl chain. These alkyl chains interact via Van der Waals forces between neighbouring molecules to promote close packing and film order. The *terminal functional group* is largely responsible for the properties of the self-assembled monolayer and its eventual application.

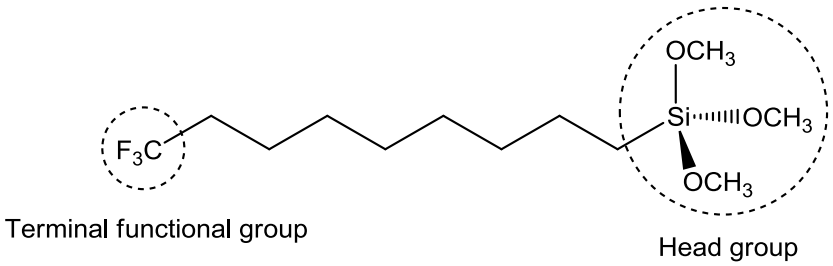

Figure 1.7. Self-assembling molecule trimethoxy(9,9,9-trifluorononyl)silane comprising a trimethoxy head group, octyl hydrocarbon chain and trifluoromethyl terminal functional group.

Self-assembled monolayers are a popular method of film/surface engineering for several reasons: the ease of preparation, low costs of solution deposition, the tenability of surface properties via modification of molecular structure and function and the use of self-assembled monolayers as building blocks in more complex structures, *e.g.* for docking additional layers to a surface.

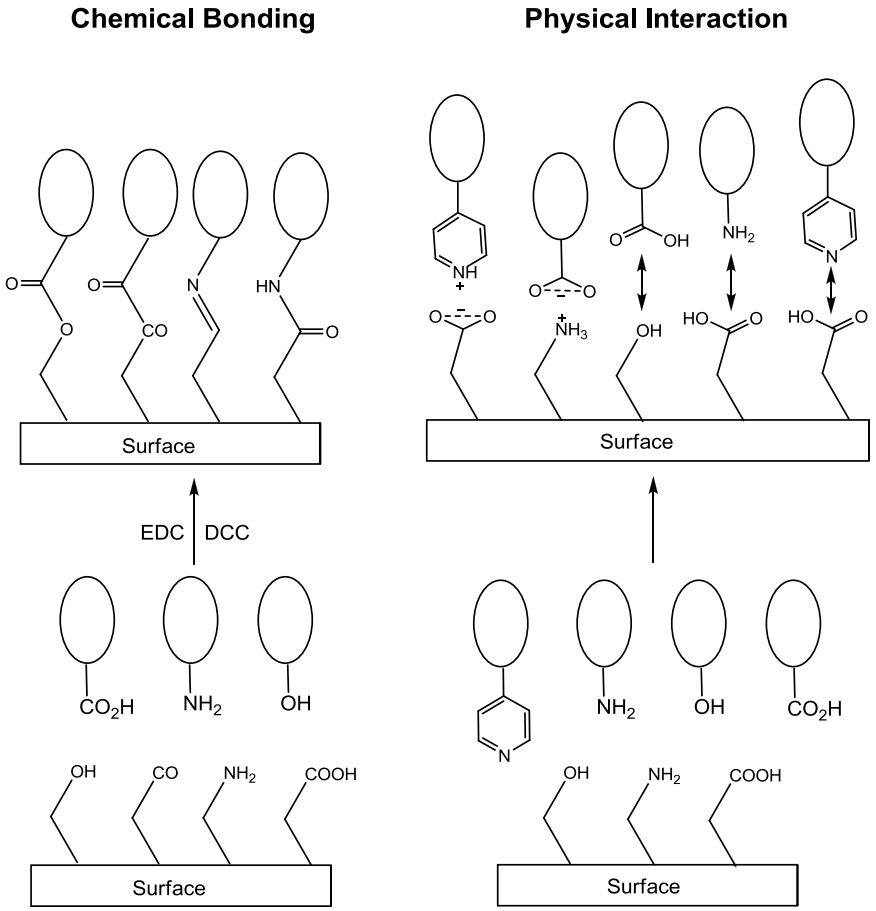

Figure 1.8. Schematic representation of bonding mechanisms that can be used to fix functional units like molecular motors to different self-assembled monolayers [38].

The latter can be exploited for fixing molecular motors to surfaces via chemical bonding or physical interaction as illustrated in Figure 1.8 [39-42]. In case of the latter

electrostatic bonding or hydrogen bonding between the head group and an appropriate anchoring group attached to the molecular motor can be realized. In the case of chemical bonding instead often a coupling agent has to be employed to bring about the reaction and this in turn may pose challenges for the stability of the motor during the coupling reaction. Moreover, if one uses light-activated motors as in the work described in this dissertation, one has to make sure that the self-assembled monolayer employed for anchoring is stable under irradiation.

1.3 The aim and outline of the thesis

The aim of the research reported in this dissertation was to study the behaviour of molecular motors on surfaces, focusing on the two most widely used surfaces, silicon oxide and gold. The study of these systems on surfaces will be discussed and compared with reported studies.

In chapter 2 we give detailed information on the experimental parameters and procedures employed for obtaining the data discussed in the thesis. The principles of X-ray photoemission spectroscopy (XPS) and contact angle measurements are explained and a full description of the procedures developed or adopted to prepare the various studied samples is given.

Chapter 3 focusses on second-generation molecular motors in solution. We show how the decrease of the size of the aromatic upper-half from a naphthalene to a thianaphthalene leads to a dramatic acceleration of the thermal helix inversion step of a light-driven rotary molecular motor. The kinetics of the various steps in the rotation of the motor are discussed and the difficulties to achieve useful applications working in the liquid phase are outlined.

In chapter 4 we detail the preparation of the azide-terminated self-assembled monolayers for gold and silicon oxide surfaces, which will later be used to anchor motor molecules on surfaces. Their stability under UV irradiation and their suitability as platform for Cu (I) catalysed 1,3-dipolar cycloadditions reactions for grafting the rotor part of the molecular motor to a solid surface is discussed. The monolayers were exposed to different doses of UV light irradiation and X-ray photoelectron spectroscopy and contact angle measurements were employed to detect radiation damage.

In Chapter 5 we give thorough information on a modified second-generation molecular motor which bears two pendant alkyne moieties at its stator part to allow for attachment to a variety of materials through a 1,3-dipolar cycloaddition. This is the most widely employed of the so-called “click”-reactions, which has shown great success in many applications including surface modification. We will show the different results obtained by X-ray photoemission spectroscopy (XPS), Ultraviolet-visible spectroscopy

(UV-Vis) and Fourier transform infrared spectroscopy (FT-IR) after anchoring this molecular motor to two different surfaces: SiO_2 and Au (111).

Chapter 6 describes the synthesis of an ultrafast molecular motor that is still functional when attached on surfaces. XPS, UV and FT-IR spectroscopy measurements will demonstrate the results obtained by different grafting pathways for the attachment of the ultrafast rotary molecular motor on gold and silicon oxide surfaces.

1.4 References

1. *"Nanoscience and Nanotechnologies: opportunities and uncertainties"*, Royal Society and The Royal Academy of Engineering, **2004**, 5, Science Policy Section, The Royal Society, London.
2. *"Nanotechnology Research Directions: IWGN Workshop Report: Vision for Nanotechnology in the Next Decade"*, Ed. M.C. Roco, R.S. Williams, P. Alivisatos, **2001**, ISBN: 0-7923-6220-9.
3. *"Unbounding the Future: Nanotechnology Revolution"*, K.E. Drexler, C. Peterson, G. Pergamit, **1992**, ISBN: 0-671-71108-3.
4. R. P. Feynmann, *Eng. Sci.* **1960**, *23*, 22.
5. J. Von Neumann, *"Theory of Self-Reproducing Automata"*, **1966**, Ed. A. W. Burks, University of Illinois Press, Urbana and London.
6. *"Scanning Tunneling Microscopy and Its Application"* C. Bai, **2000**, Springer-Verlag Berlin and Heidelberg GmbH, Germany, ISBN: 3-540-65715-0.
7. *"Atomic Force Microscopy"* P. Eaton and P. West, **2010**, Oxford University Press, ISBN: 0-199-57045-0
8. K. E. Drexler, *Proc. Nat.l Acad. Sci.* USA, **1981**, *78*, 5275.
9. M. Schliwa, "Molecular Motors" **2003**, Wiley-VCH, Weinheim.
10. M.J.A. Tyreman, J. E. Molloy, *IEE Proceedings Nanobiotechnology* **2003**, *150*, 95.
11. R.B. Vallee, P. Hook, *Nature* **2003**, *421*, 701.
12. M. Schliwa, G. Woehlke, *Nature* **2003**, *422*, 759.
13. P. Ball, *Nanotechnology* **2002**, *13*, R15.
14. E. R. Kay, D. A. Leigh and F. Zerbetto, *Angew. Chem. Int. Ed.* **2007**, *46*, 72.
15. J. Berná, D. A. Leigh, M. Lubomska, S. M. Mendoza, E. M. Pérez, P. Rudolf, G. Teobaldi and F. Zerbetto, *Nature Materials* **2005**, *4*, 704.
16. M. Irie, *Molecular Crystals and Liquid Crystals* **1993**, *227*, 263.
17. T. Yamaguchi, Y. Fujita, H. Nakazumi, S. Kobatake and M. Irie, *Tetrahedron* **2004**, *60*, 9863.
18. N. Koumura, R. W. J. Zijlstra, R.A. van Delden, N. Harada, B.L.Feringa, *Nature* **1999**, *401*, 152.
19. M. K. J. ter Wiel, R. A. van Delden, A. Meetsma, B. L. Feringa, *J. Am.Chem. Soc.* **2005**, *127*, 14208.

20. M. K. J. ter Wiel, R. A. van Delden, A. Meetsma, B. L. Feringa, *J. Am.Chem. Soc.* **2003**, *125*, 15076.
21. N. Koumura, E. M. Geertsema, M. B. van Gelder, A. Meetsma, B. L. Feringa, *J. Am. Chem. Soc.* **2002**, *124*, 5037.
22. R. A. van Delden, M. K. J. ter Wiel, H. de Jong, A. Meetsma, B. L. Feringa, *Org. Biomol. Chem.* **2004**, *2*, 1531.
23. M. M. Pollard, M. Klok, D. Pijper, B. L. Feringa, *Adv. Funct. Mater.* **2007**, *17*, 718.
24. J. Vicario, A. Meetsma, B. L. Feringa, *Chem. Commun.* **2005**, 5910.
25. E. M. Geertsema, N. Koumura, M. K. J. ter Wiel, A. Meetsma, B. L. Feringa, *Chem. Commun.* **2002**, 2962.
26. J. Vicario, M. Walko, A. Meetsma, B. L. Feringa, *J. Am. Chem. Soc.* **2006**, *128*, 5127.
27. D. Pijper, R. A. van Delden, A. Meetsma, B. L. Feringa, *J. Am. Chem. Soc.* **2005**, *127*, 17612.
28. R. A. van Delden, N. Koumura, A. Schoevaars, A. Meetsma, B. L. Feringa, *Org. Biomol. Chem.* **2003**, *1*, 33.
29. R. A. van Delden, M. K. J. ter Wiel, M. M. Pollard, J. Vicario, N. Koumura, B. L. Feringa, *Nature* **2005**, *437*, 1337.
30. M. M. Pollard, M. Lubomska, P. Rudolf, B. L. Feringa, *Angew. Chem., Int. Ed.* **2007**, *46*, 1278.
31. G. London, G. T. Carroll, T. F. Landaluce, M. M. Pollard, P. Rudolf, B. L.Feringa, *Chem. Commun.* **2009**, *13*, 1712.
32. G. T. Carroll, G. London, T. F. Landaluce, P. Rudolf, B. L. Feringa, *ACS Nano*, **2011**, *5*, 622.
33. A. Ulman, *"An Introduction to Ultrathin Organic Films"*, **1991**, Academic Press, San Diego.
34. A. N. Parikh, D. L. Allara, I.B. Azouz, F. Rondolez, *J. Phys. Chem.* **1994**, *98*, 7577.
35. S.R. Wasserman, Y.-T. Tao, G. M. Whitesides, *Langmuir* **1989**, *5*, 1074.
36. L.H. Dubois, R.G. Nuzzo, *Annu. Rev. Phys. Chem.* **1992**, *43*, 437.
37. P. E. Laibinis, G. M. Whitesides, D.L. Allara, Y.-T. Tao, A. N. Parikh, R.G. Nuzzo, *J. Am. Chem. Soc.* **1991**, *113*, 7152.
38. Adapted from the Ph.D. thesis of F. Cecchet, "Préparation et caractérisation de films ordonnés, fonctionnels et commutables de macrocycles et de rotaxanes de type amide benzylique", Facultés Universitaires Notre-Dame de la Paix, Namur, Belgium, **2003**.
39. L. H. Dubois, R. G. Nuzzo, *Annu. Rev. Phys. Chem.* **1992**, *43*, 437.
40. A. Ulman, *Chem. Rev.* **1996**, *96*, 1533.
41. F. Cecchet, M. Pilling, L. Hevesi, S. Schergna, J. Wong, G. Clarkson, D. Leigh, P. Rudolf, *J. Phys. Chem. B* **2003**, *107*, 10863.
42. S. A. DiBenedetto, A. Facchetti, M. A. Ratner, T. J. Marks, *Adv. Mater.* **2009**, *21*, 1407.

Chapter 2

Experimental Details

In this chapter we will give the description of the experimental parameters and procedures used for obtaining the data discussed in this thesis. It defines the conditions employed and the interpretation of the data in X-ray photoelectron spectroscopy (XPS) and contact angle measurements.

2.1 X-ray Photoelectron Spectroscopy (XPS)

2.1.1 General description

X-ray photoelectron spectroscopy (XPS) is a powerful spectroscopic technique that provides useful information on the elemental composition of a surface, the chemical environment of each element as well as its oxidation state [1]. This spectroscopy is important for characterizing nanomaterials, where the surface plays a dominant role in determining the material properties [2-4]. In literature we can find quite a number of studies on nanomaterials [5-9] falling mainly in two areas: 1) determination of the detailed composition, nature of surfaces, and bonding of the nanostructured materials from both qualitative and quantitative analysis of the photoemission core levels; and 2) evolution of the electronic structure as a function of size by studying the valence band/levels using both X-ray and ultraviolet photon energies.

The technique is based on the photoelectric effect, also known as the "Hertz effect", discovered by Heinrich Hertz in 1887. Then it was Albert Einstein in 1905 that developed a mathematical description of how the photoelectric effect was caused by absorption of quanta of light (now called photons). It makes use of the differences in binding energy of the core electrons of several chemical elements in various chemical environments.

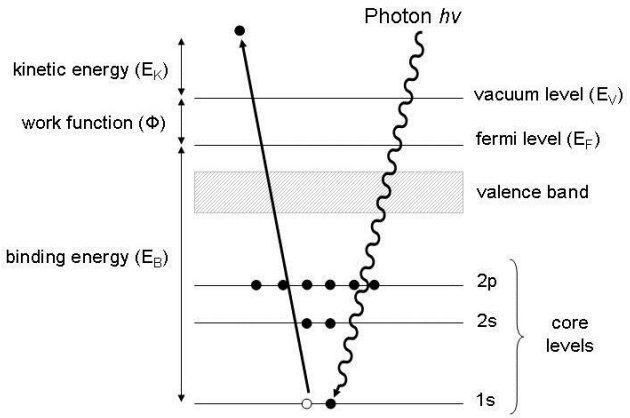

Figure 2.1. Schematic diagram of the photoelectron emission process.

In this technique, the surface to be analysed is irradiated with monochromatic X-rays while simultaneously measuring the kinetic energy (E_k) and the number of electrons escaping from the sample as shown in Figure 2.1. When a photon of energy hv interacts with an electron of a certain atom at the solid's surface, the photon energy is transferred and induces the ejection of a photoelectron with the kinetic energy E_k as well as possibly

some rearrangement of charge such as the excitation of one-electron transitions or plasmons. By measuring the kinetic energy of the photoelectron we can define the binding energy E_B of the electron as the difference between initial and final state and derive it as

$$E_k = h\nu - E_B - \Phi$$

where Φ is the work function of the spectrometer.

X-rays are generated by bombarding an anode material with high-energy electrons. The efficiency of X-ray emission from the anode is determined by the electron energy, relative to the X-ray photon energy. The most popular anode materials are aluminium and magnesium providing AlK_α or MgK_α photons of energy 1486.6 eV and 1253.6 eV, respectively.

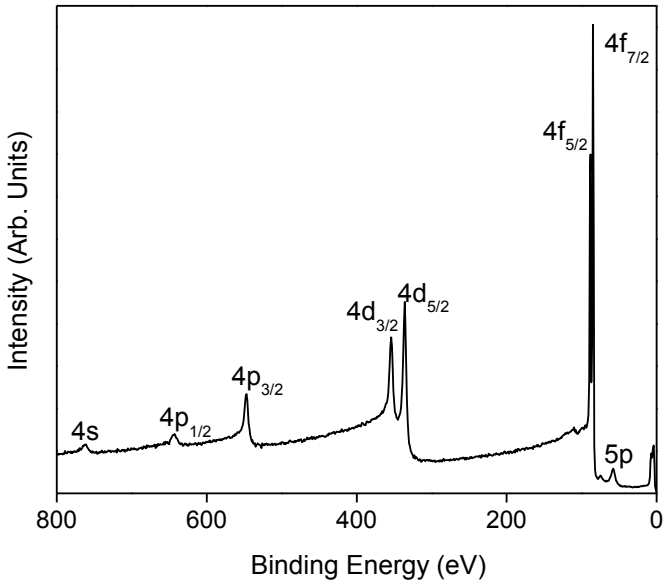

Figure 2.2. X-ray photoelectron survey spectrum of a freshly prepared gold on mica substrate.

Figure 2.2 represents the XPS survey spectrum of a gold substrate. In the spectrum, the number of electrons detected is plotted versus their binding energy. The ejected photoelectrons come mainly from core levels. Core levels are defined as the inner quantum shells, which do not participate in chemical bonding. Each element in the sample produces a characteristic set of XPS peaks at characteristic binding energies, corresponding to the electronic configuration of the atom. Like in Figure 2.2, the peaks correspond to the occupied electronic states of the electrons (*4s, 4p, 4d, 4f, 5p*) in gold. Those electrons, which are excited and escape without energy loss contribute to the characteristic peaks, while those that undergo inelastic scattering contribute to the background of the spectrum. Therefore, by analyzing the intensity of the various lines in the XPS spectrum one can deduce the elemental composition of the sample [10].

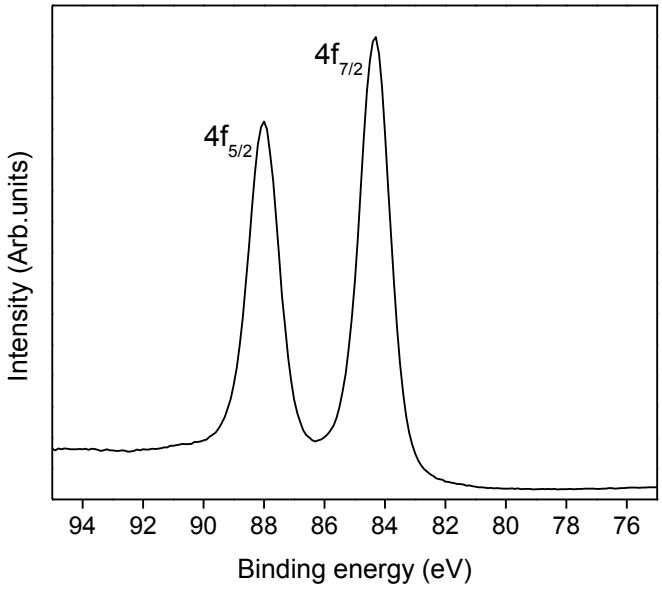

Figure 2.3. X-ray photoelectron spectrum of freshly prepared gold on mica substrate. The spectrum shows the characteristic binding energy of the gold *4f* core level.

Apart from the completely different positions of the different orbitals revealed in Figure 2.2, after photoelectron emission we can also see the spin orbit splitting in the final state. Every orbital of each element is characterized by a specific binding energy and appears in a specific region in the XPS spectrum. Figure 2.3 shows the X-ray photoelectron spectrum of the gold *4f* core level. The *4f* photoemission peak is in fact split into two peaks, one at 84.00 eV ($4f_{7/2}$) and one at 87.67 eV ($4f_{5/2}$). Due to the multiplicity of 6 for the J = 5/2 final state and the multiplicity of 8 for J = 7/2, we find them with an intensity ratio of 3:4. The energy levels of the states with lower multiplicity are lower, so the binding energy is higher and they appear more to the left side in the spectrum.

2.1.2 Ultra High Vacuum (UHV) requirements

Why are all spectrometers based on vacuum systems? There are two reasons why spectrometers used in surface analysis must operate under vacuum:

1. Electrons emitted from a sample should meet as few gas molecules as possible on their way to the analyser so that they are not scattered and thereby lost from the analysis. In other words, their mean free paths should be much greater than the dimensions of the spectrometer. Working with vacuum conditions in the range of 10^{-8} mbar would be sufficient.
2. The UHV environment is necessary because of the surface sensitivity of the technique itself. If we have a solid surface at 10^{-6} mbar, it is possible to get a monolayer of gas adsorbed in about 1s. In many experiments it is necessary to start with a well-characterized surface and small amounts of contaminant can

affect the course of the experiment. It is clearly necessary to work under conditions in which the rate of contaminants is negligible compared with the rate of change in the experiment. This determines the need for a UHV environment during analysis.

2.1.3 The depth of analysis in electron spectroscopy

The depth of analysis in XPS varies with the kinetic energy of the electrons which are detected. It is determined by a quantity known as the attenuation length (λ) of the electrons, which is related to the inelastic mean free path (IMFP). This is defined as the average distance that an electron with a given kinetic energy travels between successive inelastic collisions. In 1979 Seah and Dench from the National Physical Laboratory in UK have proposed the following equation [11]:

$$\lambda = \frac{538 a_A}{E_A^2} + 0.41 a_A (a_A E_A)^{0.5}$$

Where E_A is the energy of the electron in eV, a_A^3 is the volume of the atom in nm^3 and λ is in nm. In general the attenuation length is about 10% less than the IMFP. Various databases exist from which values of the IMFP and attenuation length can be obtained [11]. In Figure 2.4 we show calculated inelastic mean free paths for K, Al, Cu, Ag and Au [12].

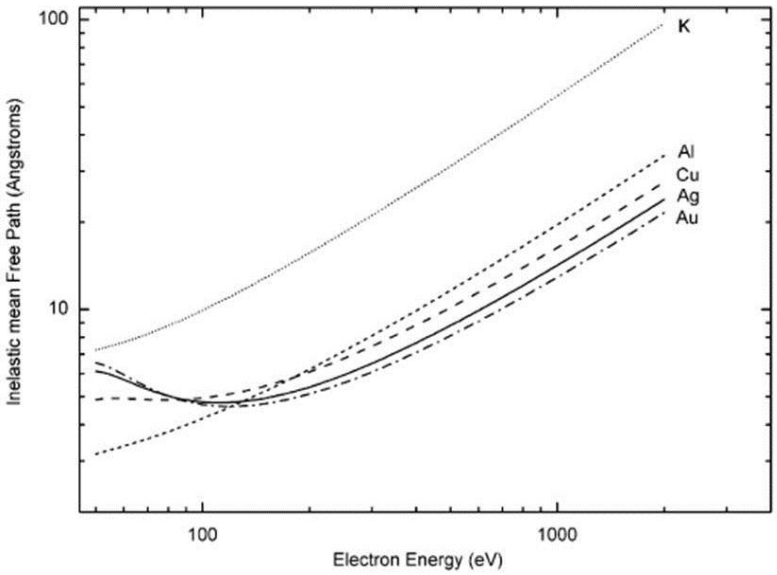

Figure 2.4. IMFPs for K, Al, Cu, Ag, and Au [12].

Since the electron mean free path for photoelectrons is very short [13], and we can no longer retrieve useful information from the kinetic energy of a photoelectron which has scattered inelastically more than once, the typical probing depth of this spectroscopy amounts to the upper 10 – 20 nm of the sample.

2.1.4 Interpretation of the spectra

The exact binding energy of an electron depends not only on the core level from which the photoelectron is emitted but also on the oxidation state of the atom and the local chemical and physical environment. As a consequence, variations in the elemental binding energy, the so-called chemical shifts, can be used to identify the chemical state or the chemical groups of the material being analysed. This is illustrated in Figure 2.5 representing the carbon *1s* spectrum of ethyl trifluoroacetate measured in the gas phase [10]. The stoichiometry of the molecule is shown above the XPS spectrum. The peaks of the spectrum correspond nicely to the binding energies of carbon in different chemical environments.

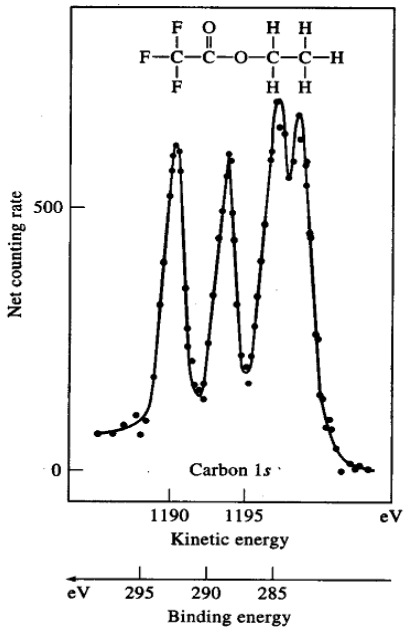

Figure 2.5. X-ray photoelectron spectrum of C 1s of ethyl trifluoroacetate [10].

The elemental quantification of a surface layer can be derived from the area under the core level peaks. To compare the amounts of different elements of the surface, the area under the peak should be divided by the relative sensitivity factor, a corrective factor that takes into account the excitation energy, the electron mean free path, the cross section and the instrumental efficiency for each element.

Once the photon flux φ is given, the photoelectron intensity I_i of the (nl) orbital of the i-th atomic species is approximately given by:

$$I_i(nl) = C_i\lambda(E_{kin})\varphi(\hbar\omega)\sigma_{nl}(\hbar\omega)T(E_{kin})$$

where φ is the photon flux, C_i the atomic concentration of the i-th species, λ is the mean escape depth, σ_{nl} the orbital cross section and T the instrumental efficiency, taken into consideration because the analyzer does not transmit electrons of different kinetic energy in the same way. We can define the sensitivity factor as:

$$S_i = \sigma_i(h\nu)T(E_{kin})$$

S_i is called the atomic sensitivity factor. Some of these factors can be calculated theoretically and others depend on the experimental conditions, the design of the spectrometer, and its electronic detection system. The relative atomic composition is determined by simply dividing each atomic core level peak intensity by the sensitivity factor [14].

Shake-up satellites

In addition to the final state where only the core electron is photoemitted, other final states are possible where in addition to the emission of the photelectron either a single valence electron is promoted to a higher unfilled level or part of the valence electrons undergoes a collective excitation (plasmon). The energy required for such a transition will also have to come from the initial photon energy and result in a discrete structure on the low kinetic energy side of the photoelectron peak, called the shake-up satellite [1].

For organic systems, conjugated and aromatic structures show shake-up satellites with intensities up to 5-10% of the primary peak. In aromatic systems this satellite structure is due to $\pi \rightarrow \pi^*$ transitions involving the two highest filled orbitals and the lowest unfilled orbital [15]. Shake-up satellites are expected to shift by 6 - 7 eV to lower kinetic energy (high binding energy) of the primary C 1s peak; these spectral features are asymmetric and sometimes distinctly double (or multiply) peaked. For fullerenes even the collective excitation of all valence electrons can occur in the C 1s photoemission (σ+π plasmon).

2.1.5 X-ray photoelectron spectroscopy measurements

For the X-ray photoelectron spectroscopy (XPS) measurements, the samples were introduced through a load lock system into an SSX-100 (Surface Science Instruments) photoemission spectrometer with a monochromatic Al Kα X-ray source (hν=1486.6 eV). The photoelectron takeoff angle was 37°. The base pressure in the spectrometer during the measurements was 10^{-10} mbar and four spots on each sample were measured to minimize the data acquisition time at each spot. The energy resolution (FWHM – full with at half maximum) measured on the substrate Au $4f_{7/2}$ core level or the Si $2p_{3/2}$ core level, depending on the surface used for the experiment, was set to minimize measuring time and to maximize the signal-to-noise ratio. For the survey spectra the resolution was set to 1.67 eV and for the detailed spectra of the different elements it was set to 1.26 eV with a spot size of 1000 µm.

XPS binding energies were referenced to the Si $2p_{3/2}$ core level with SiO_2 reference value of 103.0 eV and to the Au $4f_{7/2}$ core level set to the Au(111) reference value of

84.0 eV [16]. Spectral analysis included a Shirley background [17] subtraction* and a peak deconvolution that employed mixed Gaussian-Lorentzian functions in a least-square curve-fitting program (WinSpec), developed at the LISE laboratory of the Facultés Universitaires Notre-Dame de la Paix, Namur, Belgium. The photoemission peak areas of each element, used to estimate the amount of each species on the surface, were normalized by the sensitivity factors of each element tabulated for the spectrometer used. In practice XPS may not distinguish between the different kinds of atoms of the same element. The fitting procedure consists in reconstructing the XPS spectrum with the minimum number of peaks consistent with the raw data, the experimental resolution and the molecular structure. When we added more than one component to reproduce the raw data, the error in peak position was ± 0.1 eV. All measurements were performed on freshly prepared samples in order to guarantee the reproducibility of the results. The areas of the peaks are corrected for the photoionization cross section and the transmission of the analyser using the sensitivity factors for each element: Au 4f: 19.08, N 1s: 1.68, C 1s: 1.00, S 2p: 1.79, O: 2.49, Si 2p: 0.90 [18].

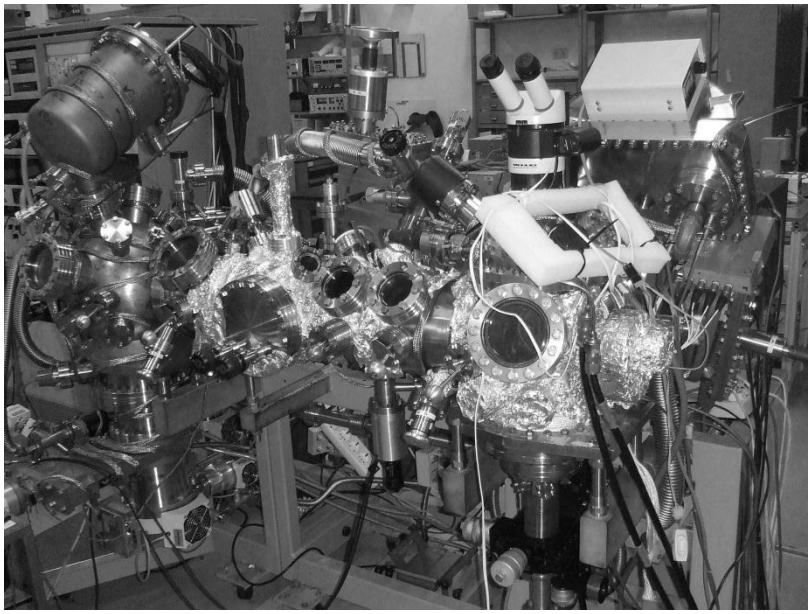

Figure 2.6. X-ray photoemission spectrometer connected with UHV chambers. Laboratory of Surfaces and Thin Films group, Zernike Institute for Advanced Materials, University of Groningen.

The error on the photoemission peak areas was estimated depending on the signal-to-noise ratio in the spectrum for each element. In general, the carbon signal is best defined and there the error was found to be 2%. The nitrogen and sulfur signals are

* In some special cases a linear background had to be taken as will be explained in the discussion of the spectra.

weaker, producing noisier spectra, and therefore a more substantial error of 10% and 15% was estimated for the peak area [19]. When more than one component was needed in the fitting to reproduce the raw data, the error in binding energy indicating the peak position was ±0.1 eV [20]. Figure 2.6 shows a picture of the X-ray photoemission spectrometer connected with UHV chambers used to perform the measurements of this dissertation.

2.2 Contact Angle Measurements

2.2.1 General description

In many industrial sectors, proper quality surfaces play an important role. In this context, the coating and painting of materials is of particular importance. Problems occur when the surfaces have relatively poor wetting and adhesion properties. This is due to the relatively low surface free energy and the absence of polar surface groups. The knowledge of the surface free energy and dispersive portions is therefore of crucial importance. In most instances when a liquid placed is placed on a solid, it will not wet it but remain as a drop having a defined contact angle (between the liquid and solid phases). This contact angle depends not only on the surface properties of solid substrates but also on the surface properties of liquids *i.e.* the surface tension of liquid. For any given solid/liquid interaction there exists a range of contact angles. The values of static contact angles are found to depend on the interaction. Two different approaches are commonly used to measure contact angles of non-porous solids: goniometry (involving the observation of a sessile drop of test liquid on a solid substrate) and tensiometry (involving measuring the forces of interaction when a solid is contacted with a test liquid) [21-26].

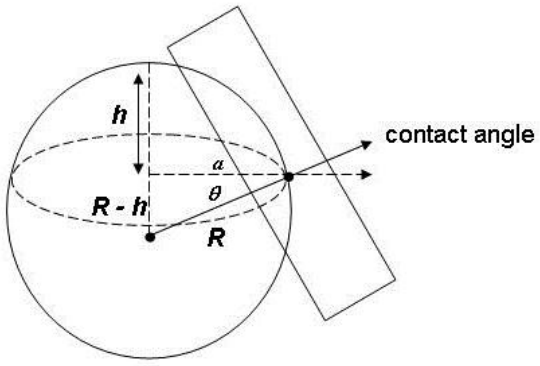

Figure 2.7. Scheme for the formation of a water contact angle [23].

As illustrated in Figure 2.7, the angle (Θ) is formed at a point on the line of contact of three phases, of which at least two are condensed phases, by the tangents to the curves obtained by intersecting a plane perpendicular to the line of contact with each of

three phases. One of the phases must be a liquid, another phase may be solid or liquid and the third phase may be gas or liquid. We can define the angle as (Θ) follows:

$$\Theta = \cos^{-1}(a/R)$$

Experimentally, when a liquid is contacted with a solid and another phase, one usually observes that the contact angle does not reach its equilibrium value instantaneously.

Most interfacial properties of liquid or solid substrates have been investigated by the contact angle technique. The relation between contact angle (Θ) and the interfacial free energy between liquid-gas (γ_{lv}), solid-gas (γ_{sv}) and solid-liquid (γ_{sl}) is given by Young's equation [23] (see Figure 2.8):

$$\gamma_{solid-gas} - \gamma_{liquid-solid} = \gamma_{liquid-gas} \cdot \cos\Theta$$

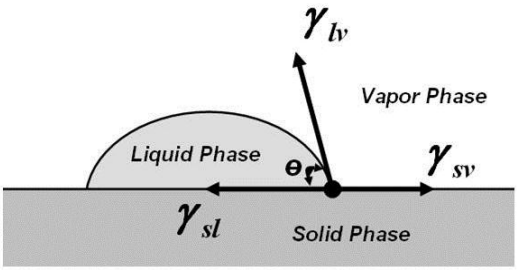

Figure 2.8. Scheme of the interfacial forces for the contact angle.

The surface energy of the solid minus the interfacial free energy between the solid and the liquid is equal to the surface free energy of the liquid times the cosine of the contact angle. This equation is derived simply from an energy balance in the horizontal direction.

The sensitivity of the contact angle is extremely high and allows to detect a fraction of a monolayer on a surface. Contact angles are extremely sensitive to the details of the surface, rather than the bulk.

Contact angle measurements respond to bonding energy rather than specific chemical compounds. Different molecules on a surface can have similar bonding energies. While contact angles determine surface energy, they do not specify chemical composition but typically it is a relatively straightforward matter to devise a set of quick experiments to sort out composition issues.

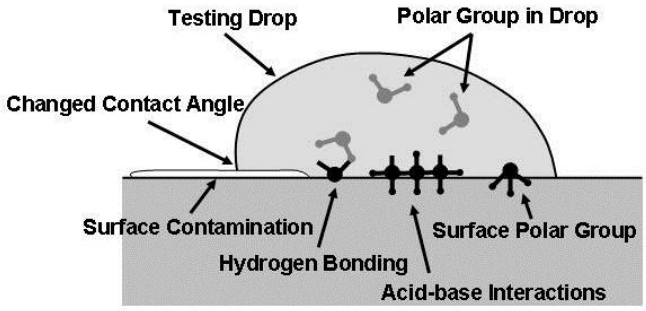

Figure 2.9. Typical factors that influence the wettability of a surface.

In typical experimental setups the drop is ultrapure water (MilliQ, 18.2 MΩ) and the wettability is actually equal to the hydrophilicity of the surface. The factors contributing to the wettability are sketched in Figure 2.9: polar bondings, hydrogen bondings, acid-base interactions, etc. Note that the measured angle can be influenced by randomly spread surface contaminations [26-27].

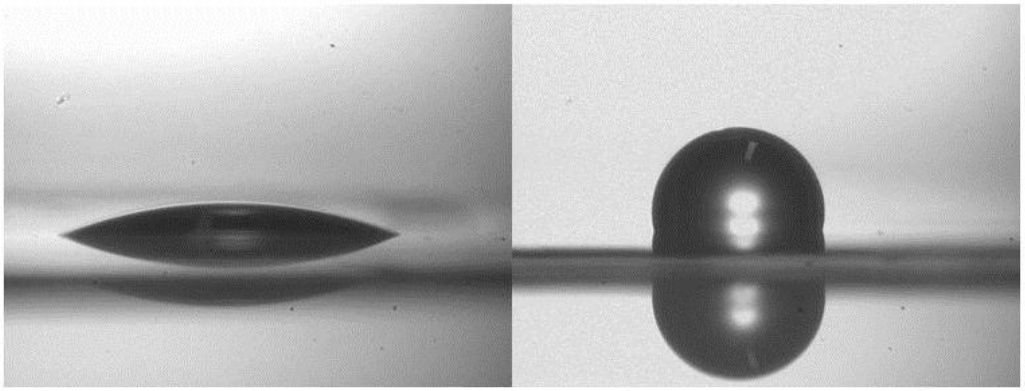

Figure 2.10. Water droplets on freshly prepared 11-hydroxyundecane-1-thiol (left) and 1-decanethiol (right) on gold, respectively [28].

The measurement of the contact angle is a useful tool to quickly check the hydrophilicity of a surface as the angles are quite specific and different between surfaces. As illustrated in Figure 2.10, the water contact angle of a self-assembled monolayer of 1-decanethiol on gold can be as high as 110° and in the order of 10° for a self-assembled monolayer of 11-hydroxyundecane-1-thiol on gold [28]. This clearly shows the effectiveness of this technique to analyse wettability effects on surfaces.

2.2.2 Contact Angle Measurements

The contact angle measurements were carried out in ambient atmosphere at room temperature (21°C) by the sessile drop method, using a custom built and remotely computer controlled microscope–goniometer system. A 1.25 µl drop of the liquid was placed on a freshly prepared sample using a Hamilton micro-syringe and the contact angle was measured after 30 and 60 s. At least three drops were measured on each

sample, and a mean value was used to describe surface properties. The standard deviation from the average value of the contact angle measured for each system was ±2°.

2.3 Substrate preparation

2.3.1 Gold on mica

The gold substrates were prepared in a custom-built vacuum chamber. The substrates were prepared by sublimation of 99.99% gold (Umicore materials AG) on mica. Freshly cleaved mica sheets (Ted Paella, Inc.) were heated at a pressure of 10^{-7} Torr to 375°C for 16 hours in order to eliminate water and environmental impurities. Then 150 nm of gold was deposited keeping the mica substrate at 375°C. Finally, the substrate was cooled down to room temperature over a period of 5 hours. With this method, atomically flat Au(111) substrates could be obtained [20]. Semitransparent gold on mica substrates were prepared following the same procedure but depositing only 10 nm of gold.

The substrates that were not used immediately after removal from the evaporation chamber were annealed by hydrogen flame. An air-hydrogen torch flame reaches 2045°C but this value is subject to considerable uncertainty and depends on the mixture used. Hydrogen flame annealing produces contaminant-free reconstructed Au (111) surfaces [20].

2.3.2 Silicon oxide

The silicon wafers were Si (100), p-type, doped with boron, with a resistivity of 1 to 10 Ω cm^{-1}, purchased from Silicon Quest International, USA. First they were cut into small pieces (usually 10 x 10 mm) and prior to exposing the surfaces to any solution, they were cleaned for 1h using a 3:7 ratio of 30% H_2O_2 in H_2SO_4 (so-called piranha solution) at a temperature of 90°C. The samples were then cleaned by sonication in deionised water (Milli-Q, 18.0 MΩ) (3 times 2 min), rinsed in methanol (2 times), and then dried under a stream of argon.

2.4 General remarks

2.4.1 UV-Vis spectroscopy measurements

UV spectra were obtained using Hewlet-Packard HP 8543 FT diode array or a JASCO V-630 spectrophotometer in a 1 cm quartz cuvette.

2.4.2 Circular Dichroism measurements

Circular Dichroism (CD) spectra were recorded using a JASCO J-715 spectropolarimeter and a JASCO PFD350S/350L Peltier-type FDCD attachment with a temperature control with a 1.0 cm cell with the following conditions: speed 100 nm/min, response time, 1 s; bandwidth 1 nm (solution) or 10 nm (surface).

2.4.3 Infrared measurements

ATR FTIR spectra were collected on a Perkin Elmer FT-IR/F-FIR Spectrometer "Spectrum 400" using a UATR attachment and liquid N_2 cooled MCT detector.

2.5 References

1. D. Briggs, M.P. Seah, "*Practical Surface Analysis"*, 2nd ed., Vol.1 John Wiley & Sons Ltd., New York **1990**.
2. H. Weller, Angew. Chem. Int. Ed. Engl. **1993**, *32*, 41.
3. A. P. Alivisatos, *J. Phys. Chem.* **1996**, *100*, 13.
4. S. A. Majetich, A.C. Carter, *J. Phys. Chem.* **1993**, *97*, 8727.
5. J. E. Bowen Katari, V. L. Colvin, A. P. Alivisatos, *J. Phys Chem.* **1994**, *98*, 4109.
6. J. Nanda, D. D. Sarma, *J. Appl. Phys.* **2001**, *90*, 2504.
7. J. Nanda, B. A. Kuruvilla, D. D. Sarma, *Phys. Rev. B* **1999**, *59*, 7473.
8. U. Winkler, D. Eich, Z. H. Chen, R. Fink, S. K. Kulkarni, E. Umbach, *Chem. Phys. Lett.* **1999**, *306*, 95.
9. C. McGinley, M. Riedler, T. Möller, H. Borchet, S. Haubold, M. Hasse, H. Weller, *Phys. Rev. B* **2002**, *65*, 245308.
10. U. Gelius, E. Basilier, S. Svensson, T. Bergmark, K.T. Siegbahn, *J. Elec. Spect. Rel. Phen.* **1974**, *2*, 405.
11. J.F. Watts, J. Wolstenholme, "*An Introduction to Surface Analysis by XPS and AES"*, John Wiley & Sons Ltd. **2003**, Chichester, England.
12. C.J. Powell, A. Jablonski, *Nucl. Instr. and Meth. A* **2009**, *601*, 54.
13. N.D. Mermin, N.W. Ashcroft, *Solid State Physics* **1976**, Holt, Rinehart & Winston, New York.

14. J. Nanda, S.S.D.D. Sarma, "*X-ray Photoelectron Spectroscopy of Nanostructured Materials",* Encyclopedia of Nanoscience and Nanotechnology **2004**, H.S. Nalwa, *Vol 10*, 711.
15. D.T. Clark, A. *J.* Dilks, *Polym. Sci., Polym. Chem. Ed.* **1977**, *15*, 15.
16. J.K. Moulder, W.F. Stickle, P.E. Sobol, K.D. Bomben, "*Handbook of X-ray Photoelectron Spectroscopy",* **1995**, Physical Electronics, Inc.
17. (a) D. A. Shirley, *Phys. Rev.* B **1972**, *5*, 4709 (b) J. Vegh, *J. Elec. Spect. Rel. Phen.* **1988**, *46*, 411.
18. P. Louette, "*Tableau des facteurs de sensibilité corrigés SSX-100"*, annex to technical documentation of the spectrometer.
19. M. M. Pollard, M. Lubomska, P. Rudolf, B. L. Feringa, *Angew. Chem., Int. Ed.* **2007**, *46*, 1278.
20. S.M. Mendoza, "*Exploiting Molecular Machines on Surfaces"*, Ph.D. thesis, University of Groningen, **2007**.
21. A. Ulman, *Thin Solid Films* **1996**, *273*, 48.
22. B. Janczuk, W. Wojcik, A. Zdziennicka, J. Morales Bruque, *Powder Technol.* **1996**, *86*, 229.
23. A. W. Adamson, A. P. Gast, *"Physical Chemistry of Surfaces"*, **1997**, John Wiley & Sons, Inc.
24. B. P. Binks, J. H. Clint, *Langmuir* **2002**, *18*, 1270.
25. G. McHale, M. I. Newton, *Colloid Surface A* **2002**, *206*, 193.
26. A. Marmur, *Soft Matter* **2006**, *2*, 12.
27. D.Y. Kwok, T. Gietzelt, K. Grundke, H.J. Jacobasch, A.W. Neumann, *Langmuir* **1997**, *13*, 2880.
28. A. Ulman, S. D. Evans, Y. Shnidman, R. Sharma, J. E. Eilers, *Adv. Colloid Interf.* **1992**, *39*, 175.

Chapter 3

Molecular motors in solution

In this chapter the design, synthesis and solution characterization of light-driven rotary motors is presented. The molecule proposed in this chapter undergoes a large increase in speed through a small change in design; we suggest that the origin of this acceleration could be the reduction of the steric interactions between the upper and lower-halves of the molecule in the fjord region.[*]

[*] This chapter is based on the results published in:

T. Fernández Landaluce, G. London, M. M. Pollard, P. Rudolf, B. L. Feringa, *J. Org. Chem.* **2010**, *75*, 5323.

3.1 Introduction

Biological nanoscale rotary motors are used to perform crucial cellular tasks including ion pumping and cellular translocation [1]. The design and construction of synthetic motors with comparable or superior speed and efficiency is one of the key challenges in contemporary chemistry [2-5]. Several approaches that synthetic molecular motors can be harnessed to perform macroscopic work have been demonstrated recently [6-8].

The so-called second-generation light-driven rotary motors based on overcrowded alkenes are able to undergo repetitive unidirectional rotation around the central olefin (the rotary axle) involving two photochemical geometric isomerizations of the alkene, each followed by a thermal helix inversion [9]. The speed of the rotary motion is limited by the thermal helix inversion step since the photochemical isomerisation of the alkene is extremely fast [10-14]. One of the key steps towards using the motion generated by synthetic light-driven rotary molecular motors to perform a useful task is to make their rotary action fast enough to compete with the surrounding Brownian motion and convert energy into controlled motion.

3.2 Rotary molecular motor: A large increase in speed through a small change in design

To achieve precise control over the rotary motion, the interplay between stereochemical, electronic, conformational and steric factors in the design of these light-driven rotary motors has been the subject of extensive research [15-16]. It has been shown that the steric hindrance in the fjord region* and the nature of the substituent at the stereogenic centre are key factors that control the speed of the thermal isomerization step [17-22]. For example, it was previously shown that contracting the ring-system fused to the central alkene from a 6-membered to a 5-membered ring (*i.e.* **1**→**2**, Figure 3.), reduced the steric interaction between the upper-half and the lower-half in the fjord region, which in turn reduced the Gibbs energy of activation of the thermal step which leads to an increase of the speed [20]. Additionally, introducing bulkier substituents to the stereogenic centre leads to the acceleration of the rate-limiting thermal isomerisation step by increasing the strain-energy of the unstable isomer more than that of the stable isomer [19]. Surprisingly however, it was also shown that the

* Fjord region: in a molecule, an area with highly restricted rotation (*i.e.* polycycles) forming a narrow inlet substructure.

removal of one of the upper-half arene moieties lead to a *deceleration* in the rate of thermal isomerization. This change was attributed to a change in the energy of the ground-state conformation, wherein the truncation allowed the molecule to adopt a conformation with less strain [22].

As an attempt to tune further the speed of the rotary motion by reducing the steric hindrance in the fjord region, a novel second-generation molecular motor **3** with a benzothiophene upper-half was designed, and its dynamic behaviour upon illumination was investigated and compared to analogs **1** and **2** (Figure 3.1) [18-19].

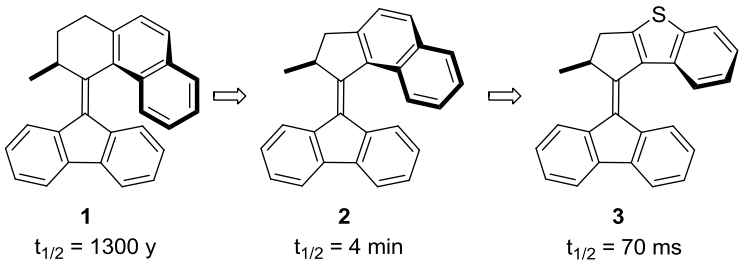

Figure 3.1. Effect of the steric interactions in the fjord region on the speed of the rotation at 25°C.

3.3 Results and discussion

Alkene **3** was prepared in a short synthetic sequence starting from benzothiophene (Scheme 3.1) [23]. A one-pot tandem Friedel-Crafts/Nazarov reaction of methacryclic acid with benzothiophene **4** in polyphosphoric acid at 80°C gave the isomeric ketones **5** and **6** in 31% and 10% yield, respectively. Ketone **5** was then treated with P_2S_5 in toluene at 45°C for 2.5 h to give thioketone **7** in 88% yield. Treatment of this thioketone with an excess of diazofluorenone in toluene at 80°C for 2 h initiated the expected [2+3]-cycloaddition with rapid subsequent extrusion of N_2 [24-29], and finally spontaneous extrusion of the sulfur atom afforded the product alkene **3** in 16% yield. The spontaneous extrusion of sulfur from similar thiiranes has been observed previously [30-31].

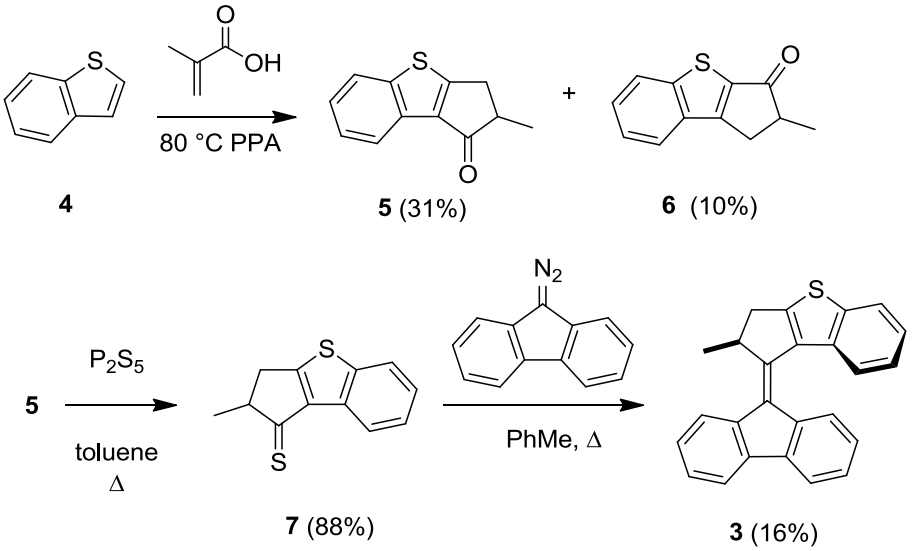

Scheme 3.1. Synthesis of molecular motor **3**.

Based on its structural similarity to known second-generation light-driven rotary molecular motors [18], we anticipated that **3** would also perform unidirectional rotation of the upper-half relative to the lower-half when illuminated with UV-light (Figure 3.2).

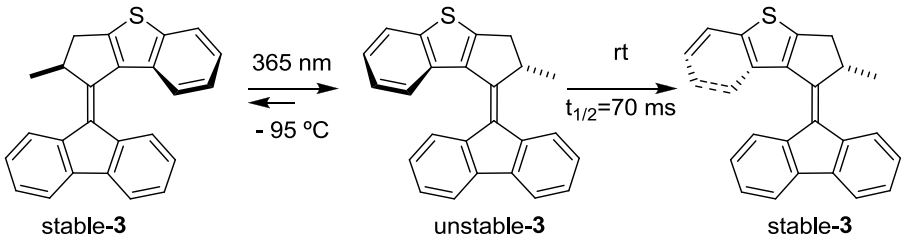

Figure 3.2. Photochemical and thermal steps in the rotary cycle of **3**.

When irradiated at a suitable temperature, these chiral overcrowded alkenes isomerize through a 4-step cycle involving two pairs of degenerate photochemical and thermal isomerizations. Initially, the stable isomer (*i.e.*, stable-**3,** Figure 3.2) undergoes a photoisomerization of the central overcrowded olefin, which leads to the formation of the unstable isomer. After the photoisomerization, the methyl group at the stereogenic center gets trapped in a high-energy conformation where it is positioned on the opposite side of the fluorene as is the benzothiophene moiety. In the rate-limiting second (thermal) step, the conformational strain is released as the benzothiophene ring slips past the lower-half arene to regenerate stable-**3**. A repetition of these steps leads to a complete 360° rotation of the upper-half relative to the lower-half.

The photochemical and thermal behaviour of alkene **3** was determined by UV-vis and ^{1}H-NMR spectroscopies [23]. A sample of **3** (0.06 mmol/L) in a 1:1 mixture of methylcyclohexane and methylcyclopentane was irradiated (λ_{max} = 365 nm) at -153°C

until no further changes were observed in its UV-vis spectrum. Upon irradiation the longer wavelength absorption of stable-**3** centred at 355 nm red-shifted to a broader absorption band centred at 410 nm (see Figure 3.3). Based on data gathered on related overcrowded alkenes, this change is consistent with the formation of unstable-**3** [17-18]. After allowing the solution to warm to room temperature, the UV-vis spectrum of the sample was identical to the spectrum of stable-**3**, which is consistent with the regeneration of the stable isomer through a thermal isomerization step.

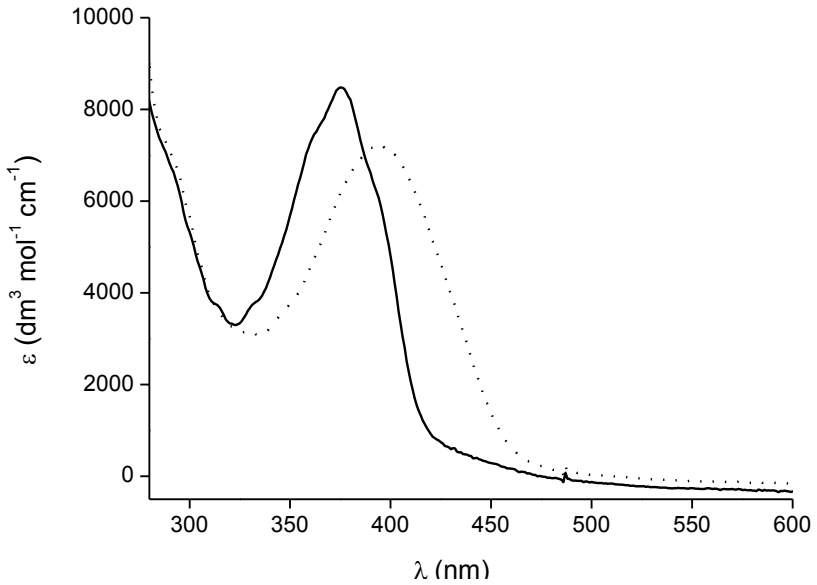

Figure 3.3. UV-vis spectrum of **3** in methylcyclohexane/ methylcylopentane at -153°C (black) and after irradiation at 365 nm for 30 min (dotted).

^{1}H NMR spectroscopy was used to verify that low-temperature irradiation of **3** led to the isomerization of stable-**3** to unstable-**3** [23]. A solution of **3** in THF-d_8 was irradiated at 365 ± 10 nm at *T*= -95°C until no further changes in the spectrum were observed. Over the course of 2 h, a new set of absorptions appeared in the ^{1}H NMR spectrum (taken at -98°C) of the sample. By comparison with chemical shifts observed in the photolysis of **2**, these changes were consistent with the clean formation of unstable-**3**. The most diagnostic changes include the downfield shift of the absorption from the methine proton at the stereogenic centre from 4.57 to 4.81 ppm, as well as the downfield shift of the absorption from the methyl group at the stereogenic centre from 1.40 to 1.62 ppm. Comparison of the integrations of the stable and unstable isomers showed that the photostationary state (PSS) at -95°C comprised both unstable-**3** and stable-**3** in 2/1 ratio. After allowing the sample to warm to room temperature, only absorptions from the stable isomer were observed in the ^{1}H NMR spectrum; this indicates that the molecule had thermally isomerized to give exclusively stable-**3**.

3.4 Kinetics and Eyring equation

In order to understand the kinetic process of the thermal helix inversion of unstable-**3** to stable-**3** we have to explain the Eyring equation, a theoretical construct based on the transition state model, which is used to study gas, solution and mixed phase reactions [32].

Let us start by briefly recalling the principles of the transition state theory (for more details see ref. 33):

1. Rates can be calculated by focussing attention on the activated complexes, which lie at a saddle point of the potential energy surface; the details of what happens before the transition state is reached are irrelevant if one is content with obtaining an expression for the overall rate.
2. The activated complexes are in a state of quasi-equilibrium with the reactants. This means that for a system at complete equilibrium the complexes are also at equilibrium, and since the concentration of complexes passing from reactants to products will be unchanged by removing products, that concentration can be calculated by using equilibrium theory.
3. The motion of the system at the saddle point, along a particular reaction coordinate, can be treated as a free translational motion and expressed by using kinetic theory.

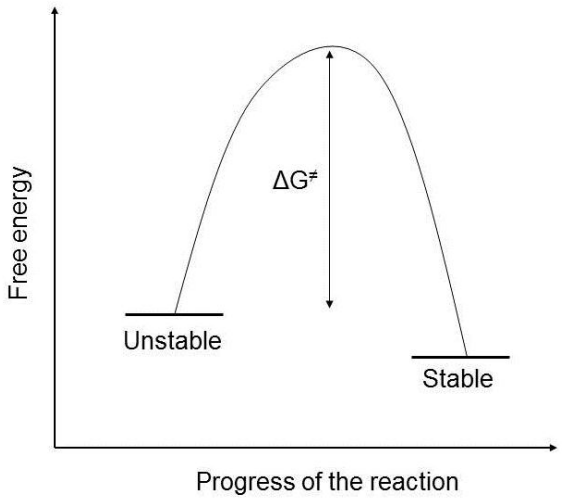

Figure 3.4. Progress of the reaction from an unstable to a stable form.

To progress from unstable-**3** to stable-**3** (Figure 3.4), the system has to overcome an energy barrier on the pathway between the unstable isomer and the stable isomer. This activation energy is the energy necessary to permit the release of the conformational strain. As indicated in Figure 3.4 a transition state is formed at the potential energy maximum. This high-potential-energy complex represents an unstable

molecular arrangement. Once the energy barrier is surmounted, the isomers will proceed downhill to the stable form.

If we assume that the molecules in the unstable form [UN] are in unimolecular equilibrium with the molecules in the stable form [ST] and call the rate constants k_1 and k_{-1}, we can define the equilibrium as presented below:

$$[UN] \underset{k_{-1}}{\overset{k_1}{\rightleftharpoons}} [ST] \qquad (1)$$

At any given time, only a subset of the molecules of [UN] has sufficient energy to undergo conversion to [ST]. If we assume that these reactive molecules (which we treat as populating the transition state) are in equilibrium with the unreactive molecules, we can relate the relative populations by an equilibrium constant $K^{\neq}$:

$$[UN] \underset{k_{-1}^{\neq}}{\overset{k_1^{\neq}}{\rightleftharpoons}} [UN]^{\neq} \xrightarrow{k^{\neq}} [ST] \qquad (2)$$

$$[UN]^{\neq} = (k_1^{\neq} / k_{-1}^{\neq}) \cdot [UN] = K^{\neq} \cdot [UN] \qquad (3)$$

where $k_1^{\neq}$ and $k_{-1}^{\neq}$ stand for the rate constants from [UN] to $[UN]^{\neq}$ and viceversa. Since we assumed that only the reactive molecules, $[UN]^{\neq}$, undergo transformation to [ST], we can associate the rate constant as follows:

$$k_1 [ST] = k^{\neq} \cdot [UN]^{\neq} \qquad (4)$$

$$k_1 = k^{\neq} \cdot \frac{[UN]^{\neq}}{[ST]} = k^{\neq} \cdot K^{\neq} \qquad (5)$$

By statistical thermodynamics, a molecular level interpretation of macroscopic thermodynamic quantities such as work, heat, free energy and entropy, we can express the so-called universal constant for a transition state as follows:

$$k^{\neq} = \frac{k_B \cdot T}{h} \qquad (6)$$

where k_B is the Boltzmann constant ($k_B = 1.381 \cdot 10^{-23}$ J/K), h is the Plank constant ($h = 6.626 \cdot 10^{-34}$ J·s) and *T* is the absolute temperature in degrees Kelvin (K).

Comparing 5 and 6 one obtains

$$k_1 = \frac{k_B \cdot T}{h} K^{\neq} \qquad (7)$$

Thermodynamics gives us a description of the equilibrium constant in terms of $\Delta G^{\neq}$ free activation enthalpy (KJ·mol^{-1}) (Gibb's free energy).

$$\Delta G^{\neq} = -R \cdot T \cdot \ln K^{\neq} \qquad (8)$$

where R is the universal gas constant = 8.3145 J/mol·K

Furthermore $\Delta G^{\neq}$ is given by

$$\Delta G^{\neq} = \Delta H^{\neq} - T \cdot \Delta S^{\neq} \qquad (9)$$

where $\Delta H^{\neq}$ is the activation enthalpy ($KJ \cdot mol^{-1}$) and $\Delta S^{\neq}$ the activation entropy ($J \cdot mol^{-1} \cdot K^{-1}$)

Combining equations 8 and 9 gives

$$\ln K^{\neq} = -\frac{\Delta H^{\neq}}{R \cdot T} + \frac{\Delta S^{\neq}}{R} \qquad (10)$$

If we substitute 10 into 7, we obtain

$$k_1 = \frac{k_B \cdot T}{h} \cdot e^{-\frac{\Delta H^{\neq}}{R \cdot T}} \cdot e^{\frac{\Delta S^{\neq}}{R}} \qquad (11)$$

$$\ln k = \ln\left(\frac{k_B}{h}\right) \cdot T - \frac{\Delta H^{\neq}}{R \cdot T} + \frac{\Delta S^{\neq}}{R} \qquad (12) \quad \text{Eyring equation}$$

$$\ln\left(\frac{k}{T}\right) = -\frac{\Delta H^{\neq}}{R} \cdot \frac{1}{T} + \ln\left(\frac{k_B}{h}\right) + \frac{\Delta S^{\neq}}{R} \qquad (13)$$

After transforming the latter expression of the Eyring Equation (eq.12), we can extract the values for $\Delta H^{\neq}$ and $\Delta S^{\neq}$ from kinetic data by plotting ln(k/*T*) vs. (1/*T*). Such a plot should provide a straight line, shown in Figure 3.5, however it is necessary to extrapolate the data to 1/*T* = 0 to obtain the latter value (eq. 14).

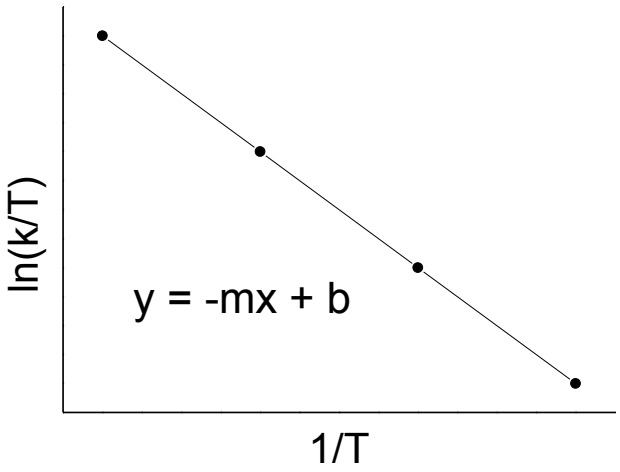

Figure 3.5. Arrhenius method, a plot of ln(k/*T*) versus 1/*T* produces a straight line.

If y = -mx + b (Figure 3.5), where x = 1/*T*, y = ln (k/*T*), $m = -\frac{\Delta H^{\neq}}{R}$ and b = y (x = 0)

Then $\Delta H^{\neq}$ can be calculated from the slope m of this line: $\Delta H^{\neq} = -m \cdot R$

With x = 0, this gives:

$$y(x = 0) = \ln\frac{k_B}{h} + \frac{\Delta S^{\neq}}{R} \qquad (14)$$

From equation 14 we can now calculate the value of $\Delta S^{\neq}$.

Once we know $\Delta H^{\neq}$ and $\Delta S^{\neq}$ we can calculate the Gibb's free energy:

$$\Delta G^{\neq} = \Delta H^{\neq} - T \cdot \Delta S^{\neq}$$

In practice the kinetic parameters of the thermal helix inversion of unstable-**3** to stable-**3** were determined by monitoring the change of the UV-Vis absorption at 418 nm as a function of different temperatures (T = 180, 190, 200, 220 K), as shown in Figure 3.6 left. A 380 nm cut-off filter was placed between the light source of the spectrometer and the sample, in order to eliminate photochemical processes induced by shorter wavelength light.

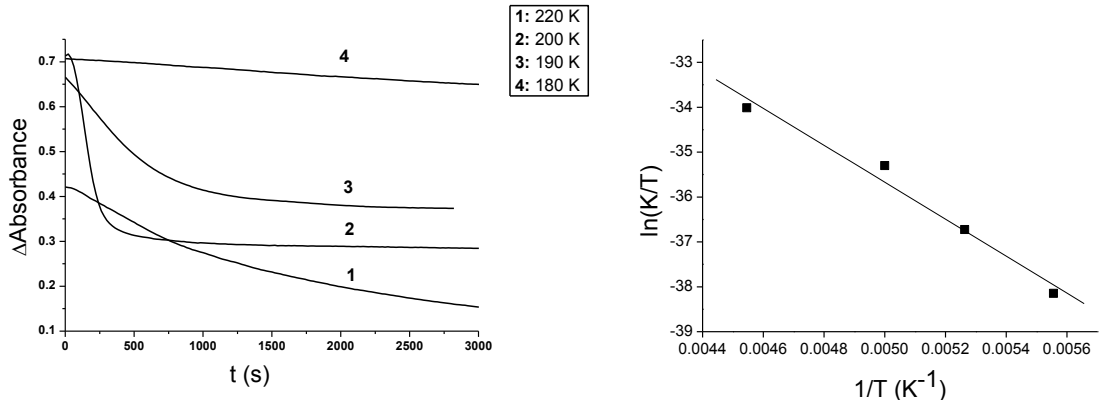

Figure 3.6. Thermal conversion of unstable-**3** to stable-**3** at 180, 190, 200, 220 K monitored by UV-vis spectroscopy in 1: 1 methylcyclohexane-methylcyclopentane mixture (left), and the Arrhenius plot based on these data (right).

Based on the rate constants (k) of the first order process the Gibbs energy of activation ($\Delta G^{\neq}$) could be determined using an Eyring plot (Figure 3.6 right) and calculated to be 66 kJ mol^{-1}. By extrapolation the half-life ($t_{1/2}$) of motor **3** was determined to be 70 ms at room temperature.

3.5 Conclusions

To quantitatively determine how much faster this new motor turns compared to **2**, we applied the Eyring equation to determine a Gibbs energy of activation ($\Delta^{\ddagger}G°$) of 66 kJ mol^{-1}. From this data, we extrapolated that the half-life of this unstable isomer at room temperature is ~70 ms, showing that the isomerization is $3.5 \cdot 10^3$ times faster than that of its predecessor **2**.

We found that truncating the size of the aromatic upper-half from a naphthalene moiety (as in **2**) to a benzothiophene moiety (as in **3**) leads to a dramatic acceleration in the thermal helix inversion. We suggest that the origin of this acceleration could be the reduction of the steric interactions between the upper and lower-halves of the molecule in the fjord region. One challenge that has to be addressed is that the synthesis of functionalized derivatives of **3** to allow for attachment to surfaces and integration in complex molecular machines.

3.6 References

1. M. Schliwa, "*Molecular Motors"*, Ed. Wiley-VCH **2003**, Weinheim.
2. W. R. Browne, B. L. Feringa, *Nat. Nanotech.* **2006**, *1*, 25.
3. B. L. Feringa, *J. Org. Chem.* **2007**, *72*, 6635.
4. S. Saha, J. F. Stoddart, *Chem. Soc. Rev*. **2007**, *36*, 77.
5. E. R. Kay, D. A. Leigh, F. Zerbetto, *Angew. Chem., Int. Ed.* **2007**, *46*, 72.
6. Y. Liu, A. H. Flood, P. A. Bonvallet, S. A. Vignon, B. H. Northrop, H.-R. Tseng, J. O. Jeppensen, T. J. Huang, B. Brough, M. Baller, S. Magonov, S. D. Solares, W. A. Goddard, C.-M. Ho, J. F. Stoddart, *J. Am. Chem. Soc.* **2005**, *127*, 9745.
7. J. Berná, D. A. Leigh, M. Lubomska, S. M. Mendoza, E. M. Pérez, P. Rudolf, G. Teobaldi, F. Zerbetto, *Nat. Mater.* **2005**, *4*, 704.
8. R. Eelkema, M. M. Pollard, J. Vicario, N. Katsonis, B. S. Ramon, C. W. M. Bastiaansen, D. J. Broer, B. L. Feringa, *Nature* **2006**, *440*, 163.
9. N. Koumura, E. M. Geertsema, A. Meetsma, B. L. Feringa, *J. Am. Chem. Soc.* **2000**, *122*, 12005.
10. D. H. Waldeck, *Chem. Rev.* **1991**, *91*, 415.
11. H. Meier, *Angew. Chem.,Int. Ed.* **1992**, *31*, 1399.
12. R. W. J. Zijlstra, P. T. van Duijnen, B. L. Feringa, T. Steffen, K. Duppen, D. A. Wiersma, *J. Phys. Chem. A* **1997**, *101*, 9828.
13. W. Schuddeboom, S. A. Jonker, J. M. Warman, M. P. de Haas, M. J. W. Vermeulen, W. F. Jager, B. de Lange, B. L. Feringa, R. W. Fessenden, *J. Am. Chem. Soc.* **1993**, *115*, 3286.

14. J. Conyard, K. Addison, I. A. Heisler, A. Cnossen, W. R. Browne, B. L. Feringa, S. R. Meech, *Nature Chem.* **2012**, *4*, 547.
15. M. M. Pollard, M. Klok, D. Pijper, B. L. Feringa, *Adv. Funct. Mat.* **2007**, *17*, 718.
16. M. Klok, N. Boyle, M. T. Pryce, A. Meetsma, W. R. Browne, B. L. Feringa, *J. Am. Chem. Soc.* **2008**, *130*, 10484.
17. N. Koumura, E. M. Geertsema, M. B. van Gelder, A. Meetsma, B. L. Feringa, *J. Am. Chem. Soc.* **2002**, *124*, 5037.
18. J. Vicario, A. Meetsma, B. L. Feringa, *Chem. Commun.* **2005**, 5910.
19. J. Vicario, M. Walko, A. Meetsma, B. L. Feringa, *J. Am. Chem. Soc.* **2006**, *128*, 5127.
20. M. M. Pollard, A. Meetsma, B. L. Feringa, *Org. Biomol. Chem.* **2008**, *6*, 507.
21. A. Cnossen, D. Pijper, T. Kudernac, M. M. Pollard, N. Katsonis, B. L. Feringa, *Chem. Eur. J.* **2009**, *15*, 2768.
22. E. M. Geertsema, N. Koumura, M. K. J. ter Wiel, A. Meetsma, B. L. Feringa, *Chem. Comm.* **2002**, 2962.
23. T. Fernández Landaluce, G. London, M. M. Pollard, P. Rudolf, B. L. Feringa, *J. Org. Chem.* **2010**, *75*, 5323.
24. D. H. R. Barton, B. J. Willis, *J. Chem. Soc., Chem. Commun.* **1970**, 1225.
25. D. H. R. Barton, E. H. Smith, B. J. Willis, *J. Chem. Soc.,Chem.Commun.* **1970**, 1226.
26. D. H. R. Barton, B. J. Willis, *J. Chem. Soc., Perkin Trans. 1*, **1972**, 305.
27. R. M. Kellogg, *Tetrahedron* **1976**, *32*, 2165.
28. J. Buter, S. Wassenaar, R. M. Kellogg, *J. Org. Chem.* **1972**, *37*, 4045.
29. H. Staudinger, J. Siegwart, *Helv. Chim. Acta* **1920**, *3*, 833.
30. C. Warren, D. N. Harpp, *J. Org. Chem.* **1993**, *58*, 4405.
31. M. M. Pollard, P.V. Wesenhagen, D. Pijper, B. L. Feringa, *Org. Biomol. Chem.* **2008**, *6*, 1605.
32. D. W. Urry, *Mathematical Modelling* **1982**, *3*, 503.
33. K. J. Laidler, M. C. King, *J. Phys. Chem.* **1983**, *87*, 2657.
34. J. H. Beynon, J. R. Gilbert, *"Application of Transition State Theory to Unimolecular Reactions"*, **1984**, Ed. Wiley.

Chapter 4

Stability under UV-light irradiation: azide- terminated self-assembled monolayers for click chemistry reactions

As the molecular structure and function of the rotor is controlled by UV irradiation and the rotor function has to be exploited on a solid surface, the stability of the surface-anchoring part for the rotor under UV irradiation should be demonstrated.

In this chapter we discuss the preparation of the azide-terminated self-assembled monolayers for gold and silicon oxide surfaces, their stability under UV irradiation and their suitability as platform for copper (I) catalysed 1,3-dipolar cycloadditions reactions for grafting the rotor part of the molecular motor to a solid surface. The investigation of the stability is not trivial because the thiolate group attached to gold or the silane group attached to silicon oxide can be oxidized under UV-light, and furthermore the azide group present in both systems can decompose photochemically. The monolayers were exposed to different doses of UV-light; X-ray photoelectron spectroscopy and contact angle measurements were performed to detect radiation damage. We found that the azide-terminated self-assembled monolayers on gold and on silicon oxide without the motor are stable for at least 1 hour under UV-light and this proves that these systems provide indeed a promising surface for copper (I) catalysed 1,3-dipolar cycloadditions reactions.

4.1 Introduction

The goal of the research described in this dissertation is to create new functional surfaces that harness and reveal mechanical motion at the single molecule level and at the macroscopic scale. Towards this goal molecular motors have to be assembled on surfaces. A method frequently used to graft macromolecular units onto a solid surface is the functionalization of a self-assembled monolayer (SAM) of alkanethiols [see for example 1-13]. As already explained in Chapter 1, the success of SAMs is due to the straightforwardness of the experimental procedure to assemble the films, their excellent reproducibility and the possibility to create a wide range of surfaces *via* the incorporation of different head groups at the end of the alkyl chains. These head groups allow grafting of different types of molecules onto a surface and serve therefore as a base from which to construct more complex molecular architectures.

For our project we chose to pursue this approach for anchoring molecular motors both on gold and on silicon oxide surfaces. Among the various reactions that one can use for forming a chemical bond between the functional group of the SAM and an appropriate functional group attached to the motor molecule, we selected "click chemistry", a term which refers to copper (I) catalysed 1,3-dipolar cycloadditions in which an azide and an alkyne form a five-membered ring [14]. The reasons for this choice will be explained in more detail in Chapter 5, where different strategies for grafting the motor molecules are described. Here we focus on a different issue: since the molecular structure and function of the molecular motor is controlled by UV irradiation, the stability of the surface-anchoring SAM under UV irradiation has to be demonstrated.

In this chapter we report on the effects of UV exposure on 11-azidoundecane-1-thiol self-assembled monolayers on gold and on 11-azidoundecyltrimethoxysilane self-assembled monolayers on an oxidized Si wafer. The monolayers were exposed to different doses of UV-light; X-ray photoelectron spectroscopy and contact angle measurements were employed to detect radiation damage.

4.2 Experimental Procedures

4.2.1 Substrate preparation

The gold and silicon substrates were prepared as explained in Chapter 2.

4.2.2 Preparation of self-assembled monolayers

a) 11-azidoundecane-1-thiol self-assembled monolayer

A solution of 1 mM of 11-azidoundecane-1-thiol in ethanol (99.9%, purchased from Merck) was prepared and the gold substrate was left in the solution overnight in the dark. The samples were taken out of the solution just before further use. They were rinsed in fresh ethanol twice and dried under argon flow.

b) 11-azidoundecyltrimethoxysilane self-assembled monolayer

A solution of 1 mM of 11-azidoundecyltrimethoxysilane in a mixture 20:1 of cyclohexane:THF was prepared, containing a small quantity of H_2O and HCl [15]. The silica substrates were left in the solution overnight and after the assembly process the azide-functionalized substrates were rinsed extensively by sonication in DMF, toluene and methanol (2 min in each) and then dried under a stream of Ar.

4.2.3 UV irradiation

For the irradiation of the sample a UV lamp of Spectroline was used. The wavelength was 365 nm and the intensity was 6.8 Wm^{-2}, measured with a Laser-MateQ SW78 laser power sensor from Coherent. The sample was placed at 7 cm from the lamp (where the intensity was measured) and left there for 1, 2, 4, 8, 16 or 24 hours.

4.2.4 X-ray photoelectron spectroscopy measurements

The X-ray photoelectron spectra (XPS) were measured in a small spot photoelectron spectrometer of Surface Science Laboratories as explained in Chapter 2. In chapter 2 we also discussed that XPS is a surface analysis technique where the probing depth is not limited by the penetration of the X-rays into the sample but by the mean free path of the photoelectrons emitted at a certain distance from the sample surface. The attenuation of the photoelectrons can also be used to determine the thickness of the layer they traversed on their way to the surface.

The attenuation of the photoelectrons when passing through an alkanethiol monolayer on Au can be calculated from the following formula [16]:

$$\ln(I_{att}) = -\frac{d}{\lambda \cos(\theta)} + const$$

In this formula, I_{att} is the intensity of the photoelectron peak, d is the effective thickness of the monolayer, λ is the attenuation length (which is found to be 42±1 Å for Au 4f electrons) [16] and ϑ is the take-off angle of the photoelectrons (*i.e.* the angle at which the detector is placed) with respect to the surface normal; in our case ϑ =37°.

From the intensities before and after irradiation we can calculate the change in effective thickness of the monolayer.

4.2.5 Contact angle measurements

The contact angle (CA) measurements were performed as described in detail in Chapter 2.

4.3 Results and discussion on gold surfaces

4.3.1 As prepared 11-azidoundecane-1-thiol self-assembled monolayer on gold

The gold substrate with a self-assembled monolayer of 11-azidoundecane-1-thiol was investigated using contact angle measurements and X-ray photoemission spectroscopy. The contact angle of the sample of pure gold on mica was 73±1°. The contact angle of the self-assembled monolayer was significantly different: 78±2°, which is in accordance with literature [17] and indicates that the surface had become more hydrophobic.

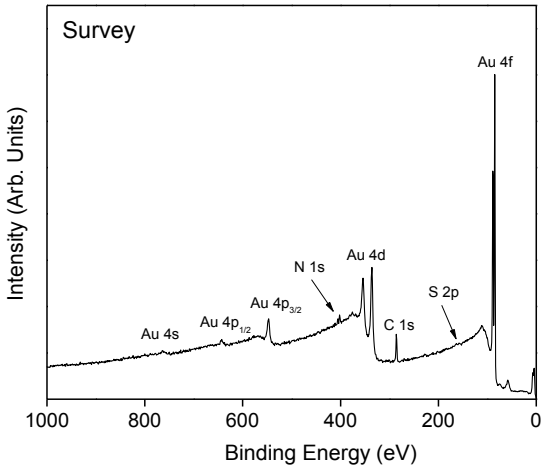

Figure 4.1. X-ray photoelectron survey spectrum of the freshly assembled 11-azidoundecane-1-thiol self-assembled monolayer on gold.

Figure 4.1 shows the XPS survey spectrum of the 11-azidoundecane-1-thiol self-assembled monolayer on gold. All the peaks are assigned to the corresponding elements

and orbitals. The gold orbitals give the largest contributions to the spectrum but the elements carbon, sulfur and nitrogen also give peaks which can be studied one by one when their region is scanned separately with a larger number of scans.

The areas of the peaks of Au 4f, N 1s, C 1s and S 2p were measured and corrected with the sensitivity factors. This gave the empirical elementary ratio C : N : S = 14.1: 4.6 : 1.0 whereas the theoretical ratio for 11-azidoundecane-1-thiol is 11 : 3 : 1. The difference between the theoretical and empirical ratio is the effect of the attenuation of the photoelectrons when they pass through the organic layer. Self-assembled monolayers on gold are in general very well-packed [18] which means that the S 2p photoelectrons will be attenuated when they travel through the organic layer and this causes the observed peak areas of nitrogen and carbon to be larger than expected in comparison to sulfur. The ratio between the Au 4f and C 1s photoemission intensities is Au : C = 1.0 : 2.0.

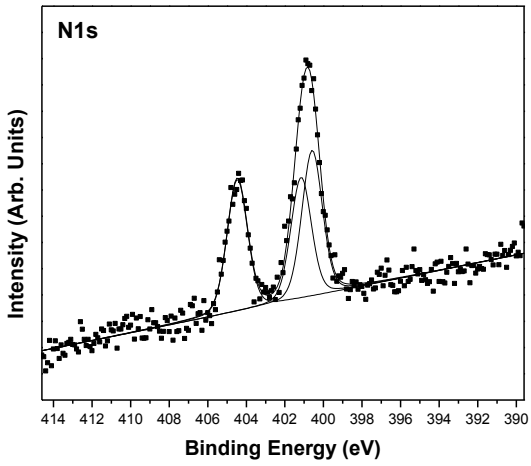

Figure 4.2. X-ray photoelectron spectrum of N 1s core level region of the freshly assembled 11-azidoundecane-1-thiol self-assembled monolayer on gold and fit of the experimental lines.

Figure 4.2 shows the XPS spectrum of the N 1s core level region, together with a fitting with three mixed singlets. The peak is superimposed on the large secondary electron background following the Au 4d peak as can be seen from Figure 4.1 and therefore the background for the fitting was taken as linear instead of as Shirley background.

The binding energy positions and relative intensities of the various components contributing to the N 1s line are summarized in Table 4.1. The azide group itself is represented below:

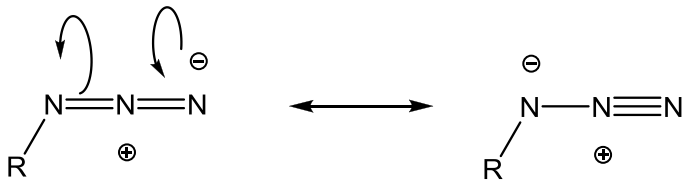

Binding energy	Relative area (sum = 100%)	Assignment
404.5 eV	36.6%	N+
401.2 eV	30.4%	N0
400.6 eV	33.1%	N-

Table 4.1. Components of the N 1s core level photoemission line of the as-prepared azide-terminated self-assembled monolayer.

At 404.5 eV we find the N 1s peak which corresponds to the electron-deficient nitrogen atom in the middle of the azide group. The peaks at 401.2 eV and 400.6 eV correspond to the neutral and electron-rich nitrogen atoms, respectively [17, 19-21]. These attributions are also listed in Table 4.1, where the relative areas are all around 33.3%, giving the exact composition of the azide group.

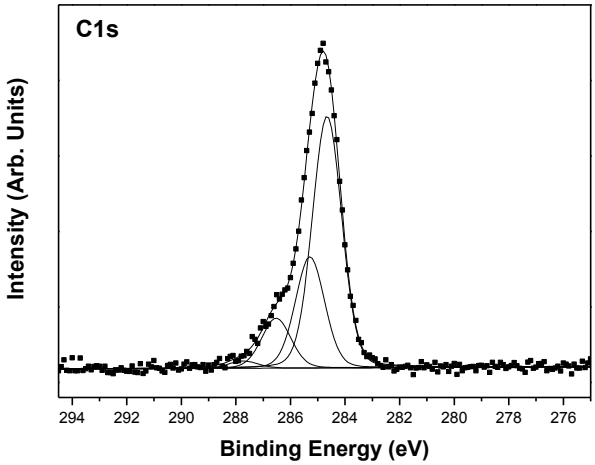

Figure 4.3. X-ray photoelectron spectrum of the C 1s core level region of the freshly prepared 11-azidoundecane-1-thiol self-assembled monolayer on gold and fit of the experimental lines.

Figure 4.3 shows the carbon 1s core level photoemission of the as-prepared self-assembled monolayer of 11-azidoundecane-1-thiol. The fitting is included in the figure. In the case of carbon there are four components: the nine aliphatic carbon atoms attached only to other carbon atoms are the most electron-rich so the low binding energy peak at 284.6 eV is assigned to them; the aliphatic carbon atom attached to the sulfur is the most electron-deficient because sulfur itself is negatively charged in the sulfur-gold bond and therefore contributes the peak at 286.4 eV; the aliphatic carbon

atom attached to the azide group gives rise to the intermediate peak at 285.2 eV. The small peak at the highest binding energy (287.6 eV) can be attributed to carbon attached to oxygen, which is due to some traces of solvent (ethanol) or air contamination.

The components and assignments are summarized in Table 4.2; the labels (1, 2, and 3) refer to the molecule drawn below:

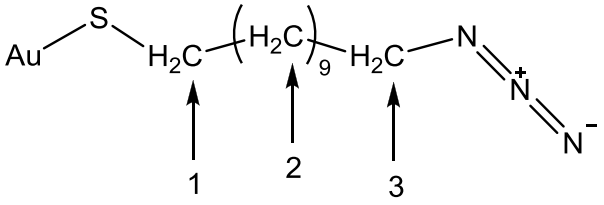

Binding energy	Relative area (sum = 100%)	Assignment
287.6 eV	1.7%	C-**C**-O
286.4 eV	11.9%	C-**C**-S (1)
285.2 eV	26.5%	C-**C**-N (3)
284.6 eV	59.9%	C-**C**-C (2)

Table 4.2. Components of the C 1s core level photoemission line of the as-prepared azide-terminated self-assembled monolayer.

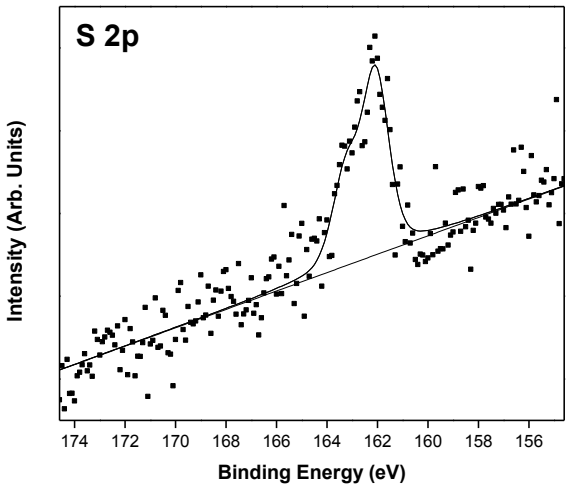

Figure 4.4. X-ray photoelectron spectrum of the S 2p core level region of the freshly prepared 11-azidoundecane-1-thiol self-assembled monolayer on gold and fit of the experimental lines.

The photoemission intensity ratios of the three carbon types that are part of the monolayer were found to be: C-**C**-S : C-**C**-C : C-**C**-N = 1 : 6 : 3. The theoretical ratio is 1: 9: 1 and the C-**C**-N component is expected to be more prominent than the C-**C**-S component

because of the attenuation of the photoelectrons when passing through the organic layer.

The X-ray photoelectron spectrum of the S 2p core level region is shown in Figure 4.4, together with a fitting with a mixed doublet. The background was taken as linear because it is dominated by the secondary electrons on the left of the Au 4f peak (See Figure 4.1). The binding energy of the S $2p_{3/2}$ peak is 162.1 eV, in good accordance with the literature values for thiolate on gold [22].

4.3.2 11-azidoundecane-1-thiol self-assembled monolayer on gold after 24 hours of UV irradiation

After 24 hours of UV irradiation (λ=365 nm) in air the 11-azidoundecane-1-thiol self-assembled monolayer can be considered as completely degraded. This can be seen from the X-ray photoelectron spectrum of the S 2p core level region which is shown in Figure 4.5.

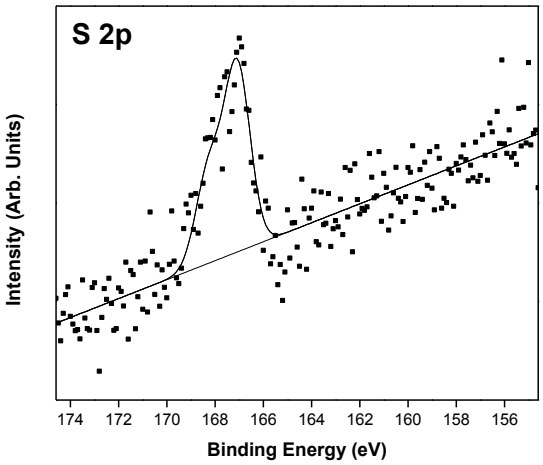

Figure 4.5. X-ray photoelectron spectrum of the S 2p core level region of the 11-azidoundecane-1-thiol self-assembled monolayer on gold after 24 hours UV irradiation in air and fit of the experimental lines.

The S $2p_{3/2}$ peak at 162.1 eV corresponding to thiolate on gold has completely disappeared. There is a new peak at 167.1 eV which corresponds to sulfonate, the resulting product of the thiolate oxidation [23]. The reaction is shown below.

$$2R-\bar{S}\ \overset{+}{Au} + 3\,O_2 \longrightarrow 2R-S\bar{O}_3\ \overset{+}{Au}$$

Literature reports that this oxidation of the thiolate takes place in air and that it is independent of light [24] but we found (data not shown) that after two hours storage in air in the dark there was no damage recognizable by XPS. The observation that the

self-assembled monolayer is degraded after 24 hours of irradiation is also supported by the CA measurement: we found a CA value of 58±3° which is significantly different from 78±2° of the as-prepared SAM of 11-azidoundecane-1-thiol, a more hydrophilic monolayer indeed expected for a layer terminated with sulphonate groups.

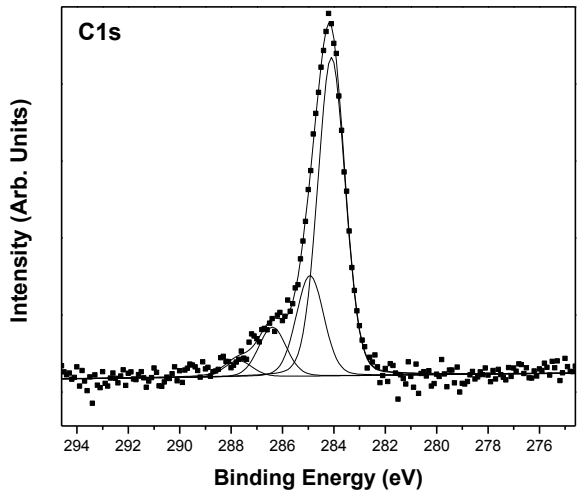

Figure 4.6. X-ray photoelectron spectrum of the C 1s core level region of the 11-azidoundecane-1-thiol self-assembled monolayer on gold after 24 hours UV irradiation and fit of the experimental lines.

As can be seen from Figure 4.6 above that the X-ray photoelectron spectrum of the C 1s core level region did not change dramatically after 24 hours of UV irradiation. The positions and relative intensities of the various components are summarized in Table 4.3.

Binding energy	Relative area (sum = 100%)	Assignment
287.8 eV	2.8%	C-**C**-O
286.3 eV	11.0%	C-**C**-S
285.0 eV	30.2%	C-**C**-N
284.3 eV	55.6%	C-**C**-C

Table 4.3. Components of the C 1s core level photoemission line of the azide-terminated self-assembled monolayer after 24 hours UV irradiation.

From these data we can conclude that the carbon chains which remain on the surface after irradiation are not oxidized. Figures 4.7 and 4.8 show the X-ray photoelectron spectra of the N 1s and O 1s core level regions, respectively. The areas of the peaks of the four elements give the empirical ratio for the self-assembled monolayer: C : N : S : O = 10.6 : 1.5 : 1.0 : 4.0. The ratio between Au and C is 1.0 : 1.2, *i.e.* it has changed with respect to 1.0 : 2.0 before irradiation. This means that the loss of carbon chains is 40% of the original amount, which is in accordance with experiments reported in the literature [24] for oxidation in the presence of visible light. It should be noted that 40% is not the actual amount but only an upper limit - a part of the signal change is also

due to the lower attenuation of the C 1s photoelectrons due to the oxidation of the azide group.

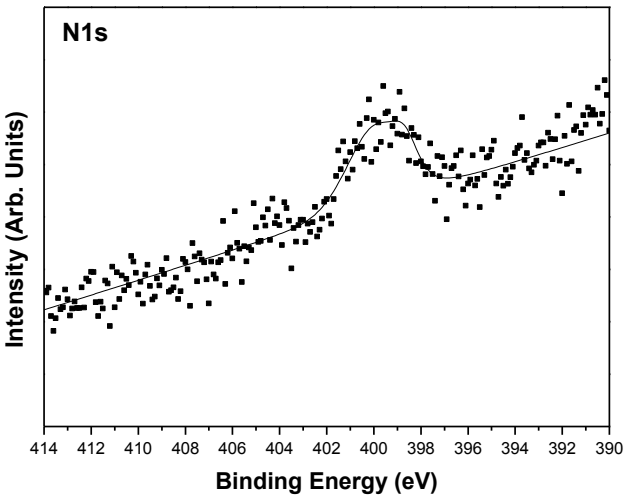

Figure 4.7. X-ray photoelectron spectrum of N 1s core level region of the self-assembled monolayer of 11-azidoundecane-1-thiol on gold after 24 hours UV irradiation.

From the N 1s region in Figure 4.7 it can be seen that the azide structure has been damaged because the peak of the central electron-deficient nitrogen atom has vanished. Furthermore, the spectrum shows that new compounds have formed. The photoemission intensity ratio N : S changes from 4.6 : 1.0 to 1.5 : 1.0, hence the amount of nitrogen after irradiation is three times lower than before irradiation. This suggests that the degradation of the azide takes place via the photolysis of the azide group resulting in elimination of molecular nitrogen. The residue at the self-assembled monolayer is a nitrene group: a single-bound nitrogen atom with two lone pairs. As the nitrogen atom in nitrene is neutral, the peak at lower binding energy in Figure 4.7 (position comparable to the electron-rich nitrogen atoms in the azide group) corresponds to a nitrene group. The photolysis of the azide group to give a nitrene is shown below [25].

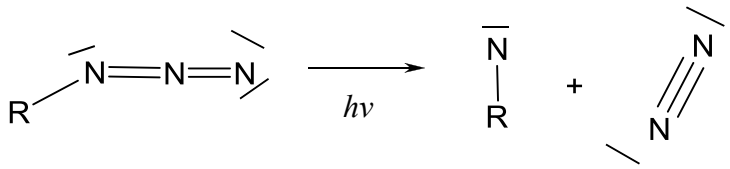

The absolute intensity of the gold peaks for the 11-azidoundecane-1-thiol self-assembled monolayer after 24 h of UV irradiation is 2.8±0.5% lower than for the as prepared SAM. This means that the effective thickness of the self-assembled monolayer has increased by about 1.0 Å. This is not what is expected when there is a loss of material from the self-assembled monolayer but could be due to oxygen attached to sulfur, *i.e.* sulphate formation, and to physisorbed water molecules.

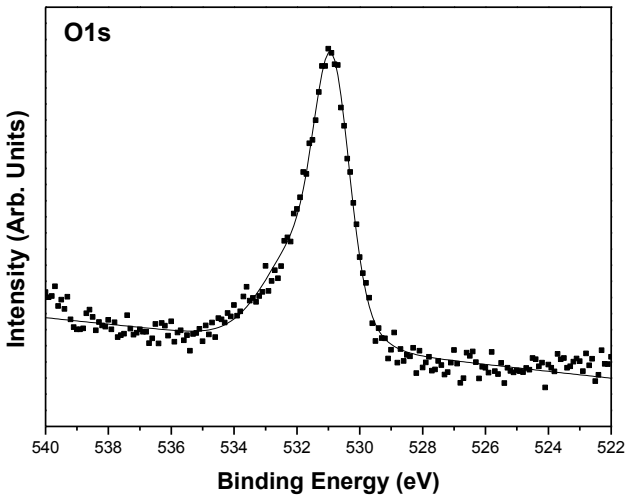

Figure 4.8. X-ray photoelectron spectrum of O 1s core level region of the self-assembled monolayer of 11-azidoundecane-1-thiol on gold after 24 hours UV irradiation.

The presence of oxygen stems most probably from the degradation of the thiolate attached to gold. However, this only accounts for a ratio S : O = 1 : 3. The rest of the detected oxygen stems from traces of physisorbed compounds, such as water.

4.3.3 Time evolution of the 11-azidoundecane-1-thiol self-assembled monolayer on gold under UV light irradiation

So far we discussed the degradation of the self-assembled monolayer after 24 hours of 365 nm UV irradiation in air as seen in the X-ray photoelectron spectra. In Figure 4.9 the X-ray photoelectron spectra of the sulfur 2p and nitrogen 1s core level regions, which are the ones where the damage is more clearly visible, are shown after different irradiation times.

These spectra show that the degradation due to the UV irradiation takes place gradually. The sulfur peak looks unchanged after 1 hour irradiation but after 2 hours the thiolate is clearly damaged. It is also apparent that for the thiolate the degradation proceeds quicker than for the azide group, where in the first hours the peak corresponding to the electron-deficient nitrogen is still present. From 8 hours of irradiation onwards the spectrum of the N 1s core level region resembles the one of 24 hours, which means that the degradation of the azide group is completed by then. These reaction times for azide photolysis agree with literature values for comparable systems in solution [26].

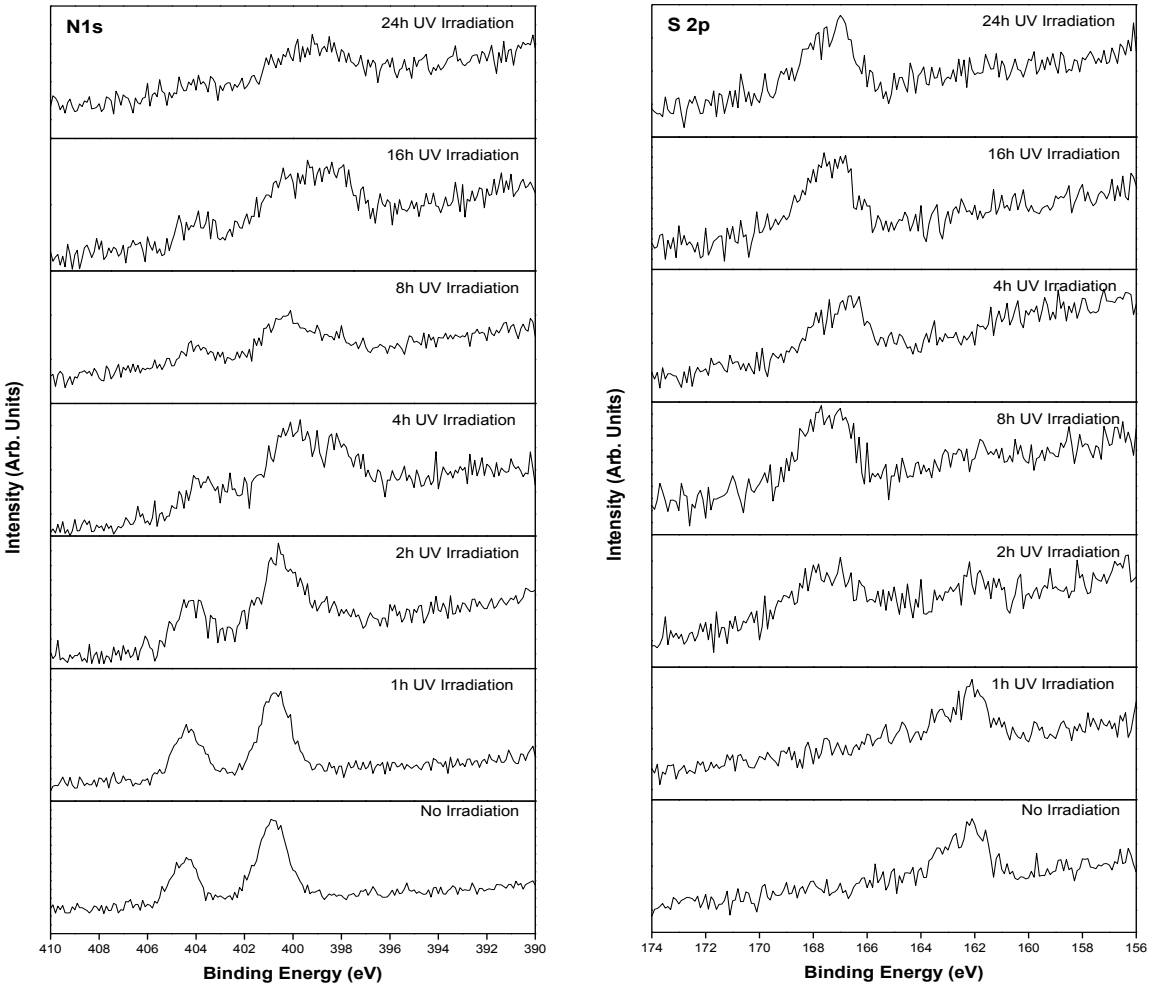

Figure 4.9. X-ray photoelectron spectra of the N 1s (left) and S 2p core level regions (right) of the 11-azidoundecane-1-thiol self-assembled monolayer on gold after different times of UV irradiation.

The contact angle evolution with irradiation time is plotted in Figure 4.10. Typical water contact angles of the freshly prepared azide self-assembled monolayers before UV light irradiation were 77±1°, as reported in the literature for other azide functionalized surfaces [27-29]. The constant decrease in contact angle during the UV irradiation can be explained by the fact that the lone pair of electrons on the nitrene nitrogen atom can easier form hydrogen bonds with water than the azide group. An increase in disorder could also contribute.

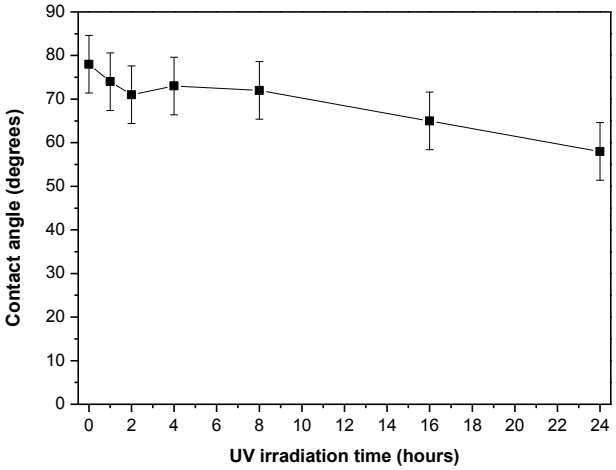

Figure 4.10. Contact angle measurements on the 11-azidoundecane-1-thiol self-assembled monolayer on gold after different times of UV irradiation.

The stability of the azide group is less important for this surface to be suitable for click chemistry than the stability of the sulfur-gold connection because the azide group is no longer present in the self-assembled monolayer after of the click reaction.

The fact that the self-assembled monolayer without the motor is stable for at least 1 hour under UV light implies that the 11-azidoundecane-1-thiol self-assembled monolayer is indeed a promising surface for click reactions with light-driven molecular motors with dialkyne legs for surface attachment.

4.4 Results and discussion on silicon oxide surfaces

4.4.1 As prepared 11-azidoundecyltrimethoxysilane self-assembled monolayer on silicon oxide

The silicon oxide substrate with a self-assembled monolayer of 11-azidoundecyltrimethoxysilane was investigated using contact angle measurements and X-ray photoemission spectroscopy. The water contact angle of the cleaned silicon oxide substrate was lower than 5°, indicating that the surface was fully covered with silanol (Si-OH) groups and completely hydrophilic [30,31]. After the self-assembly process explained in section 4.2.2.b the contact angle of the 11-azidoundecyltrimethoxysilane self-assembled monolayer was 77±2°, which is in accordance with literature [17] showing that the surface had become more hydrophobic.

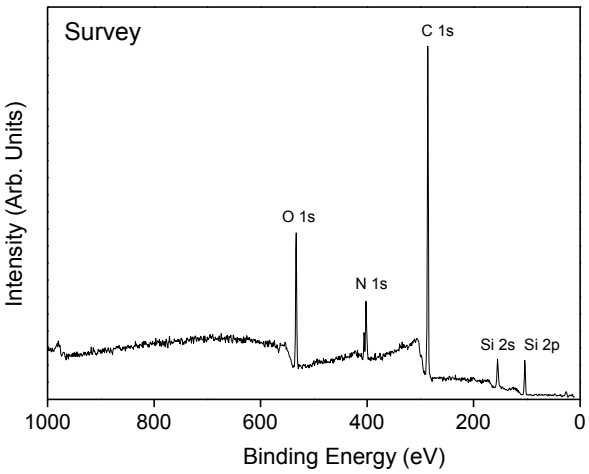

Figure 4.11. X-ray photoelectron survey spectrum of the freshly assembled 11-azidoundecyltrimethoxysilane self-assembled monolayer on silicon oxide.

Figure 4.11 shows the XPS survey spectrum of the 11-azidoundecyl-trimethoxysilane self-assembled monolayer on silicon oxide. All the peaks are assigned to the corresponding elements and orbitals, showing the composition of the monolayer and the silicon oxide substrate. Carbon, silicon and nitrogen also give peaks which can be studied one by one when their region is scanned separately with a larger number of scans.

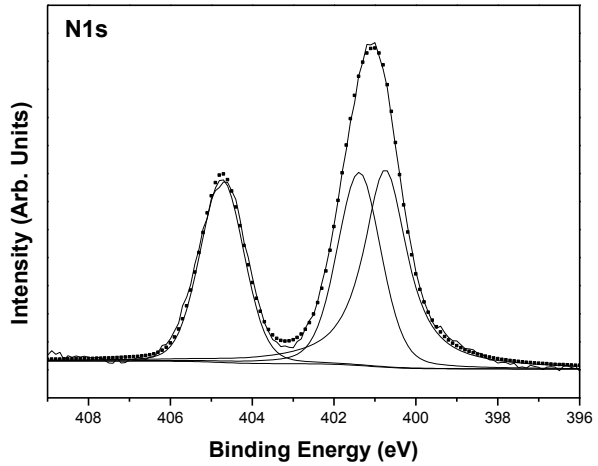

Figure 4.12. X-ray photoelectron spectrum of N 1s core level region of the freshly assembled 11-azidoundecyltrimethoxysilane self-assembled monolayer on silicon oxide and fit of the experimental lines.

Figure 4.12 shows the XPS spectrum of the N 1s core level region, together with a fitting with three mixed singlets. The binding energy positions and relative intensities of the various components contributing to the N 1s line are summarized in Table 4.4. The azide group itself is represented below:

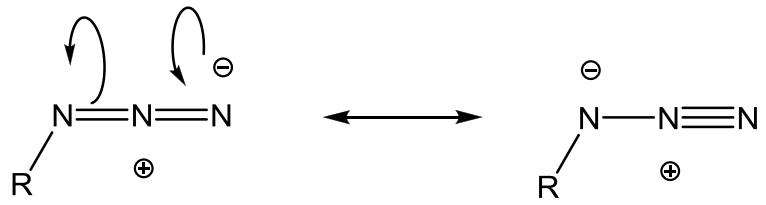

Binding energy	Relative area (sum = 100%)	Assignment
404.7 eV	33.3%	N^+
401.4 eV	33.8%	N^0
400.8 eV	32.9%	N^-

Table 4.4. Components of the N 1s core level photoemission line of the as-prepared azide-terminated self-assembled monolayer.

At 404.7 eV we find the N 1s peak which corresponds to the electron-deficient nitrogen atom in the middle of the azide group. The peaks at 401.4 eV and 400.8 eV correspond to the neutral and electron-rich nitrogen atoms, respectively [17, 19-21]. Table 4.4 also lists the relative intensities of the three N1s components; they are all around 33.3%, in accordance with the composition of the azide group.

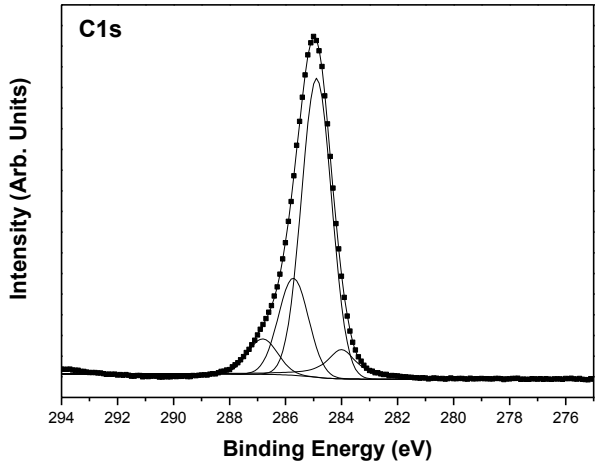

Figure 4.13. X-ray photoelectron spectrum of C 1s core level region of the freshly assembled 11-azidoundecyltrimethoxysilane self-assembled monolayer on silicon oxide and fit of the experimental lines.

Figure 4.13 shows the carbon 1s core level photoemission of the as-prepared 11-azidoundecyltrimethoxysilane self-assembled monolayer. The fitting of the C 1s spectrum shows four components: the nine aliphatic carbon atoms attached only to other carbon atoms are at a binding energy peak at 284.8 eV; the aliphatic carbon atom attached to the silicon is the most electron-rich with a binding energy of 283.7 eV, as silicon is less electronegative than nitrogen and carbon [32], the aliphatic carbon atom attached to the azide group gives rise to the intermediate peak at 285.5 eV. The small

peak at the lower binding energy (286.5 eV) can be attributed to carbon attached to oxygen due to some traces of free methoxy groups from the self-assembly process and traces of contamination; both peaks are observed at the same binding energy [33].

The components and assignments are summarized in Table 4.5; the labels (1, 2, and 3) refer to the molecule drawn below:

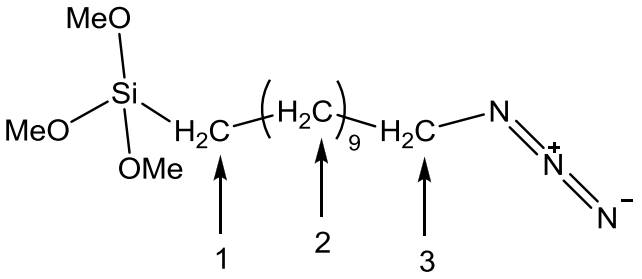

Binding energy	Relative area (sum = 100%)	Assignment
286.5 eV	14%	C-**C**-O
285.5 eV	20%	C-**C**-N (3)
284.8 eV	60%	C-**C**-C (2)
283.7 eV	6%	C-**C**-Si (1)

Table 4.5. Components of the C 1s core level photoemission line of the as-prepared azide-terminated self-assembled monolayer.

The photoemission intensity ratios of the three carbon types that are part of the monolayer were found to be: C-**C**-Si : C-**C**-C : C-**C**-N = 1:10:3. The theoretical ratio is 1:9:1, the difference in ratio can be assigned to the effect of the attenuation of the photoelectrons when passing through the organic layer.

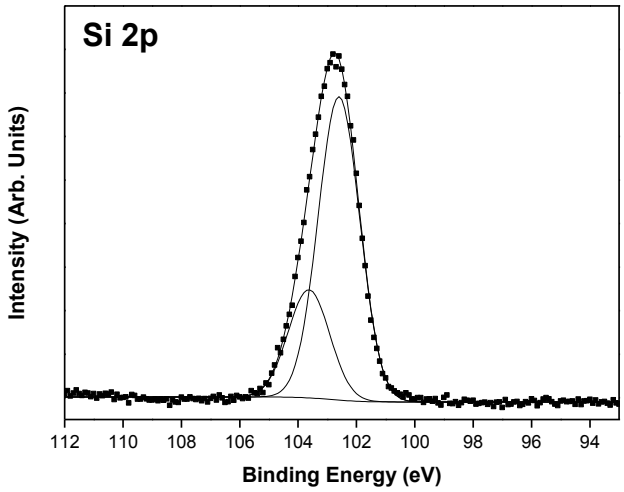

Figure 4.14. X-ray photoelectron spectrum of Si 2p core level region of the freshly assembled 11-azidoundecyltrimethoxysilane self-assembled monolayer on silicon oxide and fit of the experimental lines.

Binding energy	Relative area (sum = 100%)	Assignment
102.7 eV	74%	C-Si-O_3
103.6 eV	26%	O-Si-O

Table 4.6. Components of the Si 2p core level photoemission line of the as-prepared 11-azidoundecyltrimethoxysilane self-assembled monolayer.

The X-ray photoelectron spectrum of the Si 2p core level region is shown in Figure 4.14, together with a fitting that shows two components. The first component at a binding energy of 102.7 eV (see Table 4.6) corresponds to the Si from the 11-azidoundecyltrimethoxysilane molecule. The second peak at 103.6 eV corresponds to the Si contribution from the silicon oxide substrate; both values are in accordance with literature [34, 35].

4.4.2 11-azidoundecyltrimethoxysilane self-assembled monolayer on silicon oxide after 4 hours of UV irradiation

After 4 hours of UV irradiation (λ=365 nm) in air the 11-azidoundecyltrimethoxysilane self-assembled monolayer can be considered as degraded. The N 1s region in Figure 4.15 shows that the azide structure has been damaged, since there are two components at new binding energies. The degradation of the azide takes place via the photolysis of the azide group resulting in elimination of molecular nitrogen, as mentioned for the azide monolayer on gold.

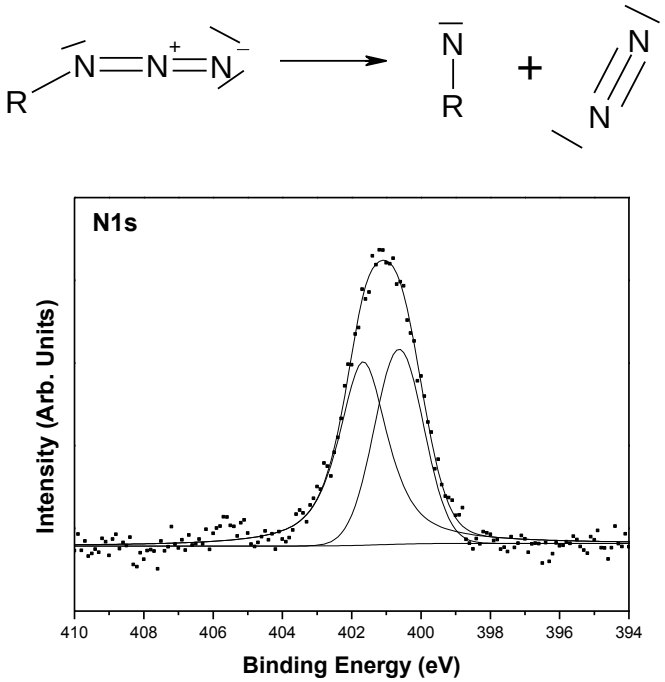

Figure 4.15. X-ray photoelectron spectrum of N 1s core level region of 11-azidoundecyltrimethoxysilane self-assembled monolayer on silicon oxide after 4 hours UV irradiation.

The residue at the self-assembled monolayer is a nitrene group: a single-bounded nitrogen atom with two lone pairs. As the nitrogen atom in nitrene is neutral, the peak at lower binding energy in Figure 4.15 (position comparable to the electron-rich nitrogen atoms in the azide group) corresponds to a nitrene group. The photolysis of the azide group to give a nitrene was shown above when discussing the degradation of the self-assembled monolayer of 11-azidoundecane-1-thiol on gold [25].

Figure 4.16 shows the X-ray photoelectron spectra of Si 2p after 4h of UV light irradiation. We can fit the Si 2p with two components, the first one at 103.6 eV corresponds to the silicon oxide substrate and the second component at 104.5 eV can be assigned to the silane group after the photolysis process, which means a higher oxidation state for the silicon.

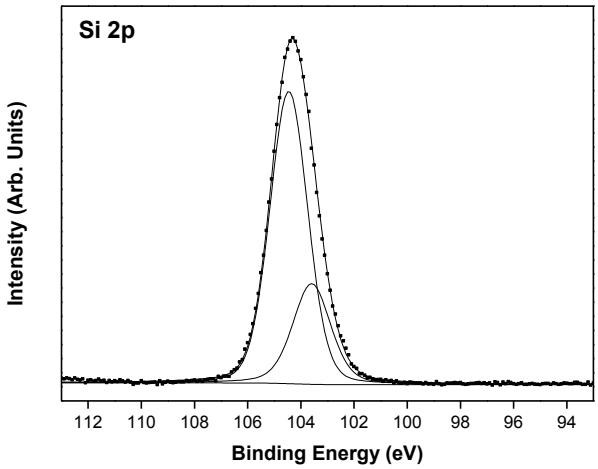

Figure 4.16. X-ray photoelectron spectrum of Si 2p core level region of 11-azidoundecyltrimethoxysilane self-assembled monolayer on silicon oxide after 4 hours UV irradiation.

4.4.3 Time evolution of the 11-azidoundecyltrimethoxysilane self-assembled monolayer on silicon oxide under UV light irradiation

We studied the degradation of the 11-azidoundecyltrimethoxysilane self-assembled monolayer after 4 hours of UV irradiation. Figure 4.17 shows the Si 2p and N 1s X-ray photoelectron spectra of the 11-azidoundecyltrimethoxysilane self-assembled monolayer on silicon oxide after different times of UV irradiation. We can clearly see how the photolysis of the silane group and the azide group already starts to take place after 2h of UV light irradiation.

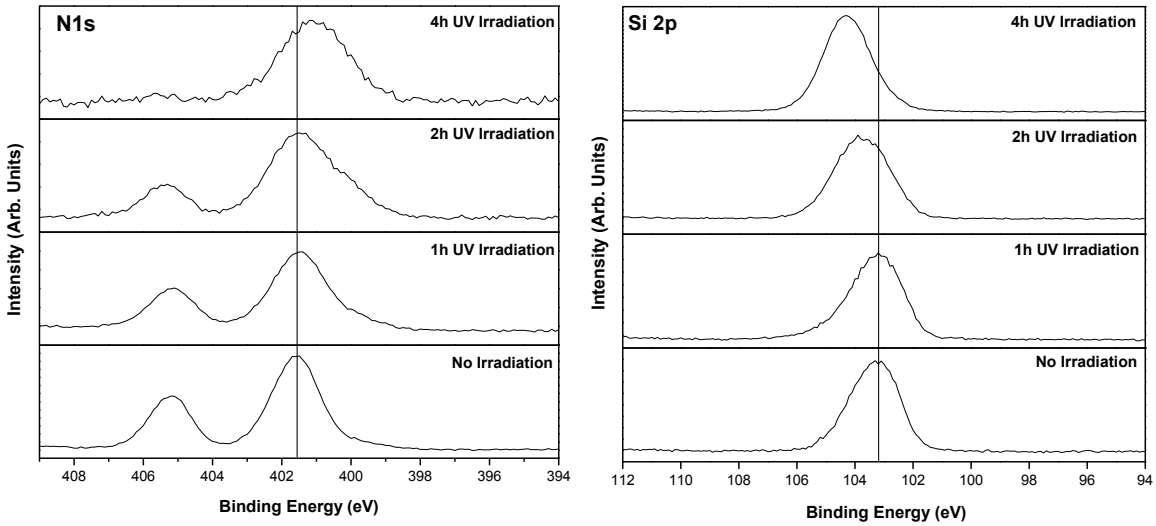

Figure 4.17. X-ray photoelectron spectrum of the N is core level region (left) and the Si 2p core level region (right) of the 11-azidoundecyltrimethoxysilane self-assembled monolayer on silicon oxide after different times of UV irradiation.

The contact angle evolution with irradiation is plotted in Figure 4.18. Typical water contact angles of the freshly prepared azide self-assembled monolayers before UV light irradiation were 77±1°, as reported in literature for other azide functionalized surfaces [27-29] and for the self-assembled monolayer of 11-azidoundecane-1-thiol on gold discussed above. The constant decrease in contact angle during the UV irradiation can be explained by the fact that the lone electron pairs on the nitrene nitrogen atom can easier form hydrogen bonds with water than those of the azide group.

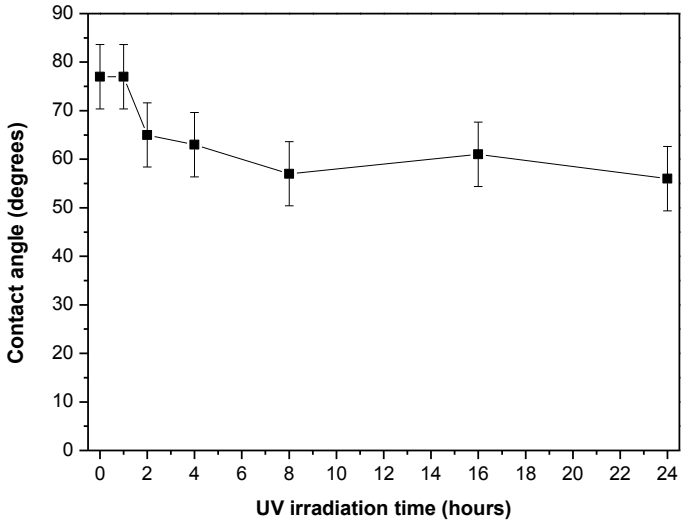

Figure 4.18. Progress of the contact angle of the 11-azidoundecyltrimethoxysilane SAM on silicon oxide during different UV irradiation times.

The stability of the azide group is less important for this surface to be suitable for click chemistry than the stability of the silane-silicon oxide connection because the azide

group is no longer present in the self-assembled monolayer after of the click reaction. The fact that the self-assembled monolayer without the motor is stable for at least 1 hour implies that the 11-azidoundecyltrimethoxysilane self-assembled monolayer like the self-assembled monolayer of 11-azidoundecane-1-thiol on gold is indeed a promising surface for click reactions.

4.5 Conclusions

Self-assembled monolayers of 11-azidoundecane-1-thiol were prepared on gold on mica and 11-azidoundecyltrimethoxysilane self-assembled monolayers were formed on silicon oxide surfaces. Both self-assembled monolayers were analysed using contact angle measurements and X-ray photoelectron spectroscopy, showing the self-assembled monolayer formation. To study the stability of these monolayers under UV light, the samples were irradiated for different times. After irradiation the SAMs were again studied by contact angle measurements and XPS. Both the sulfur atom attached to gold and the azide group were found to be degraded significantly after 2 hours of irradiation. In the case of silicon oxide surfaces the silicon atom attached to silicon oxide and the azide group were also degraded after 2 hours of exposure to UV light. As the typical irradiation time for the light-driven molecular motor is 30 minutes, we can conclude that these self-assembled monolayers are suitable platforms to attach molecular motors to gold and silicon oxide surfaces, respectively.

4.6 Appendix: Synthesis of compounds (by Dr. G. London)

a) 11-azidoundecyltrimethoxysilane

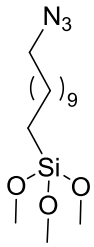

NaN_3 (130 mg, 2.0 mmol) was added to a DMF (3 mL) solution of 11-bromo undecyltrimethoxysilane (0.5 mL, 1.58 mmol). After stirring overnight at room temperature, the reaction was quenched with water (10 mL) and the aqueous solution was extracted with Et_2O (3x10 mL). The organic phase was washed with water (2x50 mL) and brine and dried (Na_2SO_4). The solvent was evaporated under reduced pressure to give 490.5 mg (1.55 mmol, 98%) of a pale yellow oil. The product was used without further purification. ^1H NMR (400 MHz, $CDCl_3$) δ 0.62-0.66 (m, 2H), 1.26 (br s, 14H), 1.36-1.40 (m, 2H), 1.59 (quin, J= 7.2 Hz, 2H), 3.25 (t, J= 6.8 Hz, 2H), 3.57 (s, 9H); ^{13}C NMR (100 MHz, $CDCl_3$) δ 9.0, 22.5, 26.6, 28.7, 29.0, 29.1, 29.3, 29.4, 33.0, 50.3, 50.4. (3 C could not observed due to overlap) HRMS (ESI) calculated for $C_{14}H_{31}N_3O_3Si$ 340.2027, found 340.2024 [36].

4.7 References

1. N. Higashi, M. Takahashi, M. Niwa, *Langmuir* **1999**, *15*, 111.
2. H. Azehara, W. Mizutani, Y. Suzuki, T. Ishida, Y. Nagawa, H. Tokumoto, K. Hiratani, *Langmuir* **2003**, *19*, 2115.
3. S. Ferretti, S. Paynter, D. A. Russell, K. E. Sapsford, D. J. Richardson, *Trend. Anal. Chem*. **2000,** *9*, 19.
4. D. Allara, *Biosens. Bioelectron.* **1995**, *10*, 771.
5. J. Madoz, B. A. Kuznztzov, F. J. Medrano, J. L. Garcia, V. M. Fernandez, *J. Am. Chem. Soc.* **1997**, *119*, 1043.
6. R. Blonder, I. Willner, F. Buckmann, *J. Am. Chem. Soc.* **1998**, *120*, 9335.
7. C. E. Jordan, B. L. Frey, S. Kornguth, R. M. Corn, *Langmuir* **1994**, *10*, 3642.
8. E. Ostuni, L. Yan, G. M. Whitesides, *Colloids Surf. B* **1999**, *15*, 3.
9. J. J. Gooding, D. B. Hibbert, *Trend. Anal. Chem*. **1999**, *8*, 18.
10. N. Patel, M. C. Davies, M. Hartshorne, R. J. Heaton, C. J. Roberts, S. J. B. Tendler, P. M. Williams, *Langmuir* **1997**, *13*, 6485.
11. L. Jiang, A. Glidle, A. Griffith, C. J. McNeil, J. M. Cooper, *Bioelectroch. Bioener.* **1997**, *42*, 15.
12. H. C. Yang, D. L. Dermody, C. Xu, A. J. Ricco, R. M. Crooks, *Langmuir* **1996**, *12*, 726.
13. T. Strither, W. Cai, X. Zhao, R. J. Hamers, L. M. Smith, *J. Am. Chem. Soc.* **2000**, *122*, 1205.
14. W.H. Binder, R. Sachsenhofer, *Macromol. Rapid Comm.* **2007**, *28*, 15.
15. C.R. Kessel, S. Granick, *Langmuir* **1991**, *7*, 532.
16. P.E. Laibinis, C.D. Bain, G.M. Whitesides, *J. Phys. Chem*. **1991**, *95*, 7017.
17. J.P. Collman, N.K. Devaraj, T.P.A. Eberspacher, C.E.D. Chidsey, *Langmuir* **2006**, 2457.
18. C. Vericat, M.E. Vela, G.A. Benitez, J.A. Martin Gago, X. Torrelles, R.C. Salvarezza, *J. Phys.-Condens. Mat.* **2006**, *18*, R867.
19. G. London, G.T. Carroll, T. Fernández Landaluce, M.M. Pollard, P. Rudolf, B.L. Feringa, *Chem. Comm.* **2009**, *13*, 1712.
20. E.W. Wollman, D. Kang, C.D. Frisbie, I.M. Lorkovic, M.S. Wrighton, *J. Am. Chem. Soc.* **1994**, 4395.
21. A. Devadoos, C.E.D. Chidsey, *J. Am. Chem. Soc.* **2007**, *129*, 5370.
22. D.G. Castner, K. Hinds, D.W. Grainger, *Langmuir* **1996**, 5083.
23. J.R. Scott, L.S. Baker, W.R. Everett, C.L. Wilkins, I. Fritsch, *Anal. Chem.* **1997**, 2636.
24. T.M. Willey, A.L. Vance, T. van Buuren, C. Bostedt, L.J. Terminello, C.S. Fadley, *Surf. Sci.* **2005**, 188.
25. E.V. Anslyn, D.A. Dougherty, "*Modern Physical Organic Chemistry"* **2006**, University Science Books, Sausalito, California.
26. R.S. Murthy, S. Muthukrishnan, S. Rajam, S.M. Mandel, B.S. Ault, A.D. Gudmundsdottir, *J. Photoch.Photobio. A* **2009**, 157.

27. S. Prakash, T. M. Long, J. C. Selby, J.S. Moore, M.A. Shannon, *Anal. Chem.* **2007**, *79*, 1661.
28. G. E. Fryxell, P. C. Rieke, L. L. Wood, M. H. Engelhard, R. E. Williford, G. L. Graff, A. A. Campbell, R. J. Wiacek, L. Lee; A. Halverson, *Langmuir* **1996**, *12*, 5064.
29. A. Heise, M. Stamm, M. Rauscher, H. Duschner, H. Menzel, *Thin Solid Films* **1998**, *327*, 199.
30. R. N. Lamb, D.N. Furlong, *J. Chem. Soc. – Faraday Trans. I* **1982**, *78*, 61.
31. L. T. Zhuravler, *Colloid Surface A* **2000**, *173*, 1.
32. L.Pauling, *J. Am. Chem. Soc.* **1932**, *54*, 3570.
33. J.F. Moulder, W.F. Stickle, P.E. Sobol, K.D. Bomben, "*Handbook of X-ray Photoelectron Spectroscopy"*, **1995**, Physical Electronics Inc. Eden Prairie, Minnesota.
34. L. S. Kasten, V. N. Balbyshev, M. S. Donley, *Prog. Org. Coat.* **2003**, *47*, 214.
35. C. D. Wagner, D. E. Pasoja, H. F. Hillery, T. G. Kinisky, H. A. Six, W. T. Jansen, J. A. Taylor, *J. Vacuum Sci. Technol.* **1982**, *21*, 933.
36. The data and results presented in this section are explained in detail in the dissertation of G. London, *"Light-driven molecular motors and switches in confined environments"*, Ph.D. thesis, University of Groningen, **2011**.

Chapter 5

Attachment of light-driven molecular motors on surfaces

In this chapter we will describe the investigation of the surface attachment of altitudinal rotary molecular motors via click chemistry reactions on gold and silicon oxide surfaces. Moreover, direct attachment of these systems using different functionalities in the anchoring "legs" of the rotary molecular motors has been studied in search of new procedures for surface grafting.[*]

[*] Part of the results presented in this chapter have been published in:

G. London, G. T. Carroll, T. F. Landaluce, M. M. Pollard, P. Rudolf, B. L. Feringa, *Chem. Commun.* **2009**, *13*, 1712.

G. T. Carroll, G. London, T. F. Landaluce, P. Rudolf, B. L Feringa, *ACS Nano* **2011**, *5*, 622.

5.1 Introduction

5.1.1 Light-driven molecular motors

Molecular motors are systems that incorporate several molecular components working in concert to perform complex and integrated functions at different hierarchical levels [1]. Inspired by biological concepts like this, nanoscientists are driven to mimic those structures and to synthesize synthetic molecular motors [1-5]. Most of these motors are investigated in solution but there the motion of the individual molecules is incoherent, so no collective effect is achieved. With molecular motors on a surface, however, such an effect can be realized, leading to macroscopic changes in the surface properties [6]. Creating a concerted motion requires architectures which restrict degrees of freedom because molecular components are constantly in Brownian motion and one needs to control their directionality of movement to get a measurable result and (even more importantly) to get an effect so that the motor can produce work. In the case of light-driven molecular rotors the energy input is light.

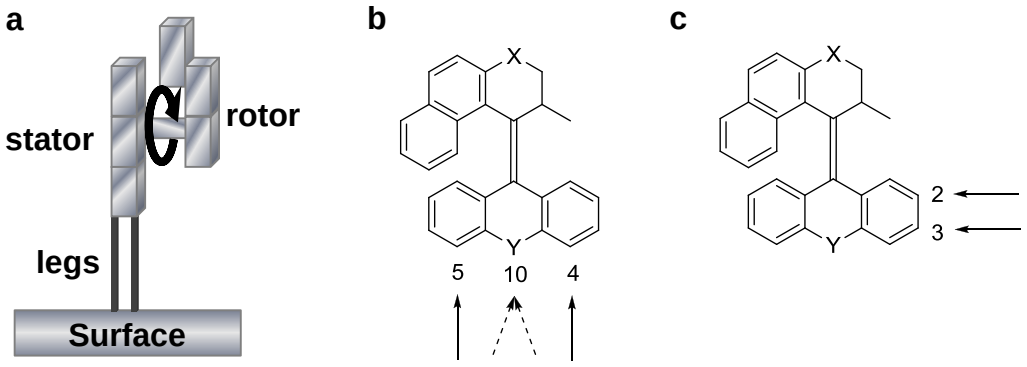

Figure 5.1. Scheme of a rotary molecular motor (a). Azimuthal (b) and altitudinal (c) substitution pattern on second generation molecular motors.

In Figure 5.1a we can see the schematic representation of the different parts of a rotary molecular motor. The motor should have at least two connections ("legs") to the surface to prevent thermal rotations of the part that should not move. Above the legs there is the static part, the stator. This part does not move upon irradiation. On the other side of the axle there is the rotor, which is the part that moves. The rotor can bear a functional group; in that case the rotor is not symmetric and the rotation can bring about a macroscopic effect when we have a monolayer of this molecule on the surface since the functional groups are collectively either exposed or hidden.

The rotation of the molecular motors can occur in two different orientations with respect to the surface: azimuthal or altitudinal motors (Figure 5.1b and 5.1c). For an azimuthal motor the axis of rotation is perpendicular to the surface while for an

altitudinal one, the axis is parallel [7-10]. The advantage of using an altitudinal rotor is that if the motor bears a functional group the character of the surface can change with rotation. As can be seen from Figure 5.1b and 5.1c, the same molecule can be used for both azimuthal and altitudinal motion if the position of the legs is changed.

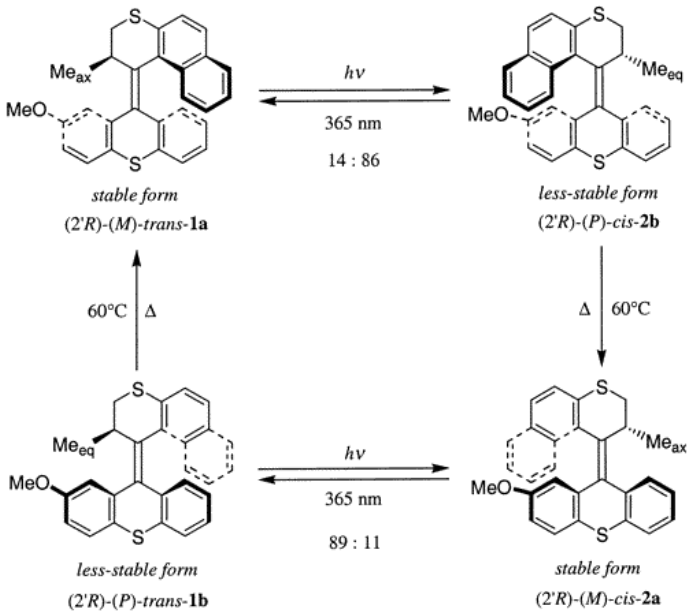

Figure 5.2. Four-step rotary cycle of a molecular motor [11].

The operation of these light-driven rotors is based on carbon-carbon double bonds that can rotate under irradiation (photoisomerization). An example of this motion is shown in Figure 5.2 [11]. The stable isomer of the motor molecule possesses a single stereogenic centre bearing a methyl group that dictates the direction of rotation, and adopts a pseudoaxial conformation to minimize steric strain. The motor functions by absorption of a photon (energy input) leading to a cis→trans isomerization of the central double bond which is the motor's axis of rotation. This isomerization leaves the molecule in a high-energy conformation in which the methyl group adopts a pseudoequatorial orientation where it experiences steric crowding with the lower half of the molecule. A thermodynamically favourable helix inversion relieves the strain as both the methyl group and the naphthalene ring slip past the aromatic moieties of the lower half, regenerating the stable conformation with a pseudoaxial methyl group and finishing 180° of rotation. Repeating this cycle results in a complete 360° unidirectional rotation [7]. The motor shown in Figure 5.2 has been successfully attached in an azimuthal orientation to quartz and silicon surfaces in 2007 by Pollard *et al.* [7].

As explained in Chapter 1, for the surface attachment of molecular motors 2 different strategies can be followed. Functionalized rotary molecular motors with anchoring groups can be directly grafted to the surface via a chemical bond, or molecular motors can be anchored on a dense self-assembled monolayer previously prepared on the surface as introduced in Chapter 4. To gain control over the bound molecular

structures on the surface few criteria have to be taken into consideration when attaching these molecules to a surface. A concept that accomplishes these requirements is the so-called “click chemistry”, a method widely used for surface modification [12-21].

5.1.2 “Click Chemistry”

The term “click chemistry” refers to copper (I) catalysed 1,3-dipolar cycloadditions in which an azide and an alkyne form a five-membered ring [16]. It can be used to “click” two building blocks of a complex molecule together. Since the reactants are stable and the reaction takes place under mild conditions, there are in general no side-reactions and the synthesis proceeds quite easily. The general reaction scheme is shown in Figure 5.3.

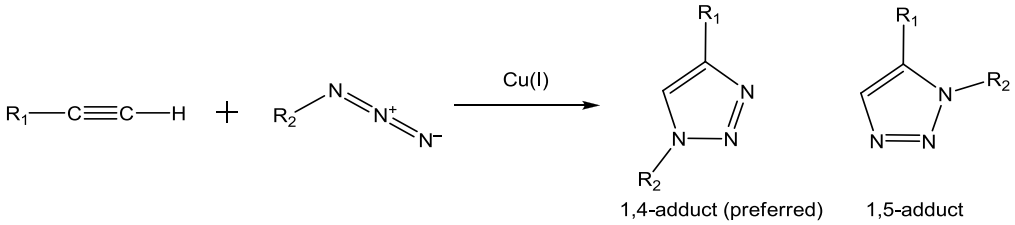

Figure 5.3. General scheme of 1,3 dipolar cycloaddition ("click reaction").

The copper (I) catalysed 1,3-dipolar cycloaddition can be used to click complex molecules onto a self-assembled monolayer containing the azide end group, for example on a gold surface [16,17]. This has the advantage that the self-assembled monolayer can be more densely packed because the bulky groups of the molecules to be anchored are introduced after the preparation of the self-assembled monolayer. One of the first examples has been ethynyl ferrocene [16], which was successfully connected to a self-assembled monolayer consisting of 11-azidoundecane-1-thiol and 1-decanethiol.

In a later study the same authors extended this concept to different mixtures of the solution from which the self-assembled monolayer was prepared [17], mixed self-assembled monolayers were formed from azidoundecanethiol $N_3(CH_2)_{11}SH$ and various diluent alkanethiols; octanethiol $CH_3(CH_2)_7SH$, decanethiol $CH_3(CH_2)_9SH$, hexadecanethiol $CH_3(CH_2)_{15}SH$, mercaptoundecanoic acid $HO_2C(CH_2)_{10}SH$, and mercaptoundecanol $HO(CH_2)_{11}SH$. Using these methods, the authors observed that the azides couplings are free of side reactions and can react quantitatively and rapidly with acetylene-bearing species. The major limitation on these reactions is steric hindrance but Collman *et al.* [17] were able to make the azide sterically accessible for reaction by forming mixed monolayers having longer chain diluents and thereby showed that surfaces containing organic azides are excellent platforms for further modification. One can control and measure the amount of a surface-bound azide that, once incorporated, reacts quantitatively with an acetylene. In addition the presence of the azide can be monitored to ensure completeness of the reaction. Collman *et al.* [17] concluded that azide

monolayers are nearly ideal interfaces for the immobilization of functional molecules on surfaces.

As mentioned above, "click chemistry" reactions are expected to be a useful tool for functionalization of surfaces with rotary molecular motors. In this study we will investigate surface attachment of altitudinal and azimuthal rotary molecular motors via click chemistry reactions. Moreover, direct attachment of these systems using different functionalities in the anchoring "legs" of the rotary molecular motors will be studied in search for new procedures for surface grafting.

5.2 Experimental Procedures

5.2.1 Substrate preparation

The gold and silicon substrates were prepared as explained in Chapter 2.

5.2.2 Preparation of self-assembled monolayers

a) 11-azidoundecane-1-thiol self-assembled monolayer

The 11-azidoundecane-1-thiol SAMs on Au were prepared as detailed in Chapter 4. For the samples with a mixed monolayer the solution contained different ratios of 11-azidoundecane-1-thiol and 1-decanethiol (purchased from Aldrich) (1:1, 1:10) and the preparation of the films was as for the 11-azidoundecane-1-thiol SAMs described in Chapter 4.

b) 11-azidoundecyltrimethoxysilane self-assembled monolayer

The 11-azidoundecyltrimethoxysilane SAMs on silica substrates were prepared as described in Chapter 4.

5.2.3 Motor attachment

a) Copper (I) catalysed azide-alkyne cycloaddition

For the copper (I) catalysed azide-alkyne cycloaddition, a solution of 1 mM of the dialkyne-motor **5.2**, 0.02 mM $CuSO_4 \cdot 5H_2O$ (99.0%, purchased from Aldrich) and 0.01 mM sodium ascorbate (99.0%, purchased from Sigma) was prepared in dimethylformamide (DMF) (99.0%, purchased from Acros). The sample with the self-assembled monolayer was left in this solution for at least 36 hours for the reaction to be completed. Before characterization the samples were rinsed in DMF, water and methanol and dried under argon flow.

b) Self-assembly of dithiol-motor on a gold surface

A solution 1 mM of the di-thiol molecular motor in a mixture 1:2 of ethanol:DCM was prepared. Freshly prepared gold substrates were left in the solution for 2 days. The

samples were taken out of the solution just before further use. They were rinsed in fresh ethanol and dried under argon flow.

c) Dialkyne-motor on a gold surface

A solution 10 mM of the di-alkyne molecular motor in ethanol was prepared. A fresh sample of gold on mica was left in the solution for 1 day, and subsequently the samples were rinsed in ethanol and then dried under a stream of argon [22].

5.2.4 X-ray photoelectron spectroscopy measurements

The X-ray photoelectron spectra (XPS) were measured with a small spot photoelectron spectrometer of Surface Science Laboratories as explained in Chapter 2.

5.2.5 Contact angle measurements

The contact angle (CA) measurements were performed as described in detail in Chapter 2.

5.3 Attachment of molecular motors to surfaces via 1,3-dipolar cycloaddition reaction of azides with alkynes

5.3.1 On gold: Dialkyne-motor 5.2 attached to a azide-terminated SAM

a) Using a monolayer of 11-azidoundecane-1-thiol

We prepared an 11-azidoundecanethiol-1-thiol self-assembled monolayer following the procedure described in in Chapter 4. Then the so-called “click reaction” (see section 5.2.3a) was performed on the functionalized gold surface. Figure 5.4 shows a scheme of the copper (I) catalysed 1,3-dipolar cycloaddition reaction to attach the dialkyne-motor **5.2** to the azide monolayer.

The samples were analysed by XPS before and after the attachment of the molecular motor; the data is shown in Figure 5.5. This allowed verifying whether the molecular motor was indeed grafted onto the functionalized gold surface.

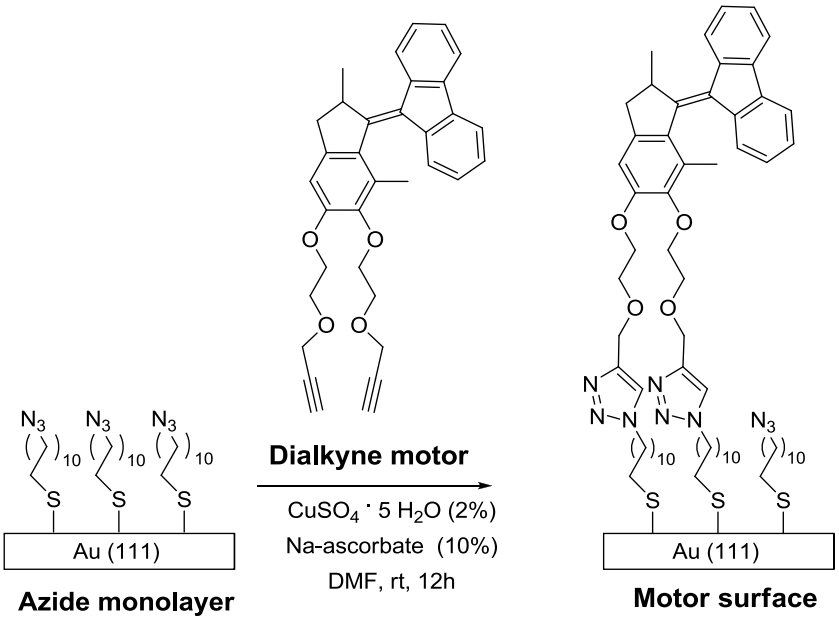

Figure 5.4. Scheme of the copper (I) catalysed 1,3-dipolar cycloaddition reaction to attach the dialkyne-motor **5.2** to the azide monolayer.

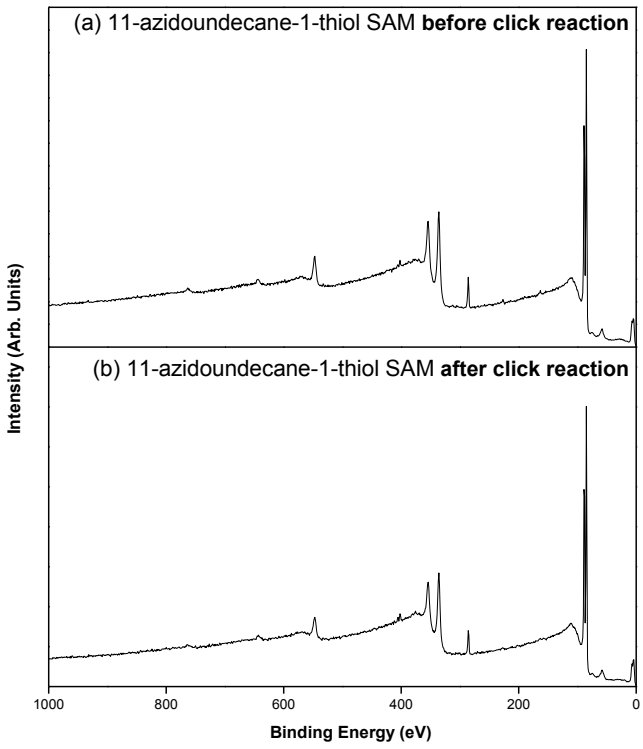

Figure 5.5. X-ray photoelectron survey spectrum of the 11-azidoundecane-1-thiol self-assembled monolayer before (a) and after (b) the click reaction.

As can be seen in Figure 5.5, the spectra of the 11-azidoundecane-1-thiol self-assembled monolayer look the same before and after the click reaction, in particular

the relative intensity of the carbon signal has not increased. This suggests that the click reaction, shown in figure 5.4, did not take place.

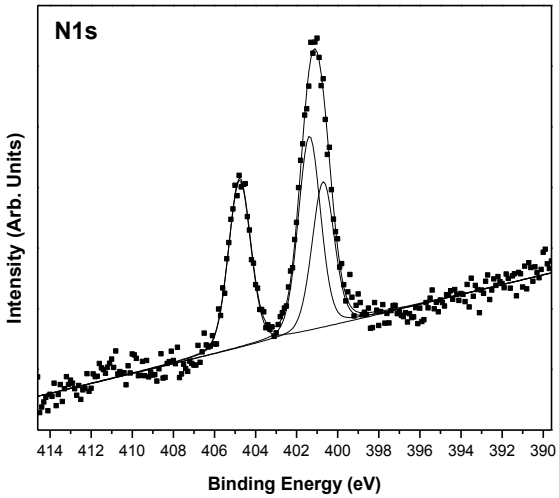

Figure 5.6. X-ray photoelectron spectrum of N 1s core level region of the 11-azidoundecane-1-thiol self-assembled monolayer after the click reaction and fit of the experimental lines.

The detailed spectrum of the N 1s core level region of the XPS spectra is shown in Figure 5.6, where we can see three components. The first peak at 404.5 eV corresponds to the electron-deficient nitrogen atom in azide group (see Figure 5.7). The peaks at 401.1 eV and 400.5 eV correspond to neutral and electron-rich nitrogen atoms, respectively [17, 23-25].

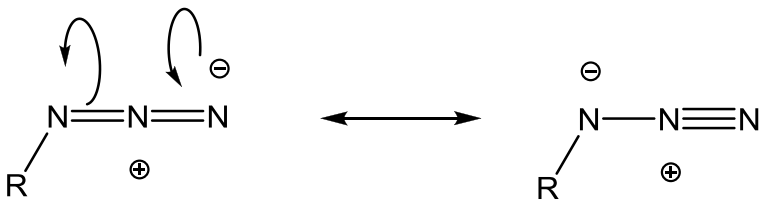

Figure 5.7. Resonance structures of the azide group.

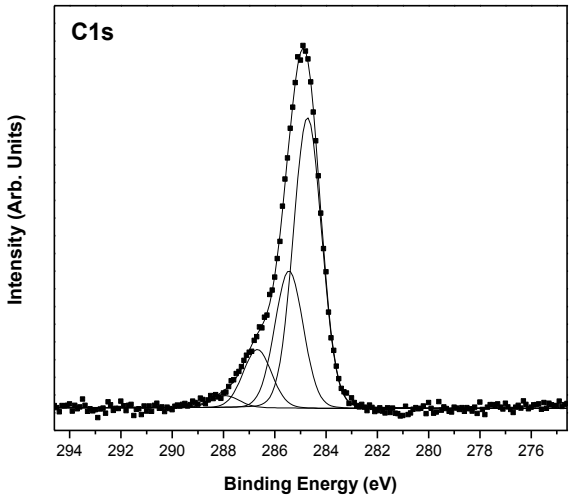

Figure 5.8. X-ray photoelectron spectrum of C 1s core level region of the 11-azidoundecane-1-thiol self-assembled monolayer after the click reaction and fit of the experimental lines.

Figure 5.8 presents instead the detailed view of the C 1s core level region of the XPS spectrum of the same sample. Comparison of the data from Figures 5.7 and 5.8 with that from the as prepared 11-azidoundecane-1-thiol self-assembled monolayer (see Figures 4.2 and 4.3 in Chapter 4) leads to the conclusion that the motor attachment did not take place. Moreover, this conclusion is confirmed by reflective UV absorption experiments (not shown) which did not show any absorption peaks of the motor. The fact that there are no motor molecules attached to the azide-functionalized gold surface can be understood from the densely packed structure of the self-assembled monolayer. In the azide/alkyne "click reaction" there is a formation of 1,2,3-triazoles, therefore in order to create this five-membered ring structure and hence graft the motor (which is a bulky group), we need 'space' on the surface. Due to the density of the self-assembled monolayer this reaction could be sterically hindered.

b) Using a mixed monolayer of 11-azidoundecane-1-thiol and 1-decanethiol with a ratio 1:1.

A way to overcome this steric hindrance is to use a mixed monolayer, as reported in literature [16-17]. For this purpose we prepared a mixed monolayer from a solution of 11-azidoundecane-1-thiol and 1-decanethiol, described in section 5.2.2a. The contact angle was measured and found to be 66±4°. This lower contact angle is characteristic of a less ordered monolayer, as expected for a mixed self-assembled monolayer. The ratio between 11-azidoundecane-1-thiol and 1-decanethiol was 1:1. Once the mixed monolayer was prepared we grafted the dialkyne molecular motor following the procedure described in section 5.2.3a. Figure 5.9 shows a scheme of the copper (I)

catalysed 1,3-dipolar cycloaddition reaction to attach the dialkyne-motor **5.2** to the mixed azide monolayer.

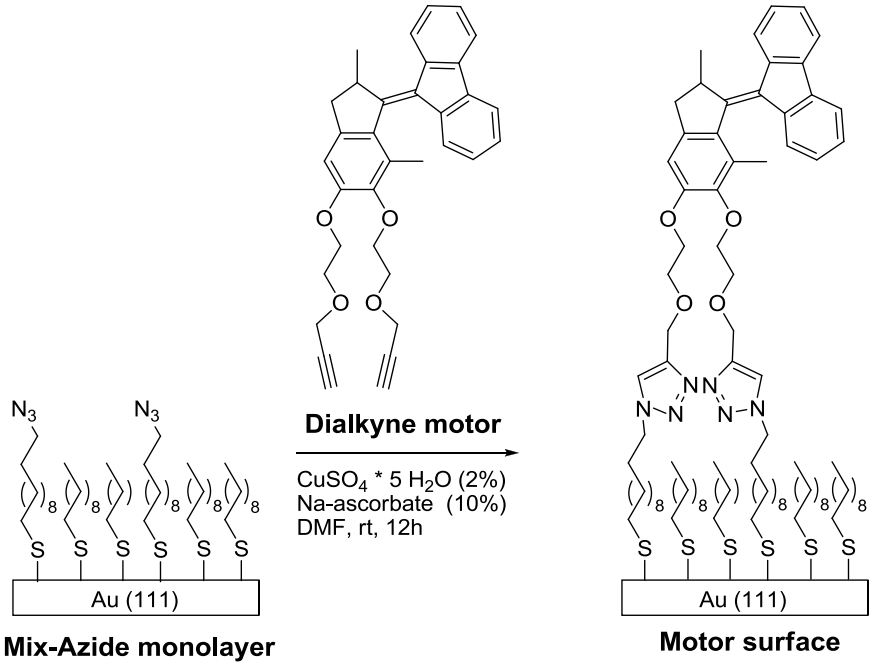

Figure 5.9. Scheme of the copper (I) catalysed 1,3-dipolar cycloaddition reaction to attach the dialkyne-motor **5.2** to the mixed azide monolayer on Au(111).

The X-ray photoelectron spectrum of the N 1s core level region of the mixed monolayer after the copper (I) catalysed 1,3-dipolar cycloaddition with the dialkyne-motor **5.2** is shown in Figure 5.10. The data is identical to the one for the self-assembled monolayer of 11-azidoundecane-1-thiol before attaching the molecular motor (see Figure 4.3 in Chapter 4). As we can see in Figure 5.10 the detailed spectrum of the N 1s core level region shows three components at the following binding energies: 400.6 eV, 401.1 eV and 404.6 eV, the three binding energies correspond to the each of the nitrogen atoms in the azide group [17, 23-25]. This means that as for the pure 11-azidoundecane-1-thiol SAM discussed above, there is no motor attached to the mixed self-assembled monolayer, as there is no signal for the triazole formation.

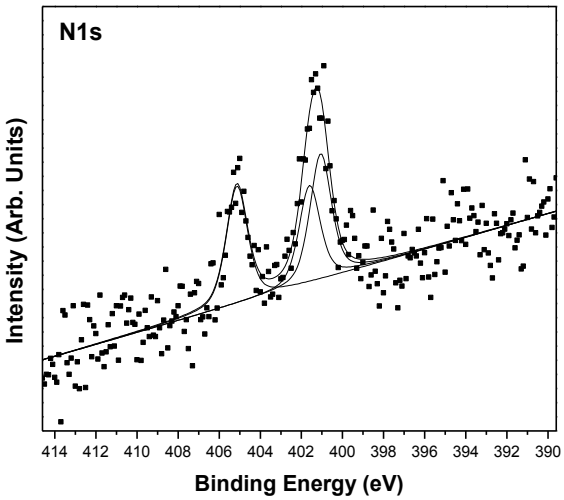

Figure 5.10. X-ray photoelectron spectrum of the N 1s core level region of the 1:1 mixed monolayer of 11-azidoundecane-1-thiol and 1-decanethiol after the click reaction and fit of the experimental lines.

To graft the motor to the self-assembled monolayer on gold, we have to decrease the concentration of azide groups on the surface by changing the ratios in the solution of the mixed monolayer or to change the reaction conditions which are used in the click reaction.

c) Using a mixed monolayer of 11-azidoundecane-1-thiol and 1-decanethiol with a ratio 1:10.

A mixed self-assembled monolayer of 11-azidoundecane-1-thiol and 1-decanethiol with a ratio 1:10 was prepared. In Figure 5.11 we can see the spectrum of the N1s core level region of the 1:10 mixed monolayer of 11-azidoundecane-1-thiol and 1-decanethiol, showing the 3 nitrogen components of the azide group (see Figure 5.6). The intensity of the peaks is lower as we have less azide groups on the surface. Water contact angle measurements were performed on the mixed monolayer functionalized surface, giving a contact angle value of 92±1°. As expected, a higher concentration of 1-decanethiol will lead to a more hydrophobic surface, as the amount of methyl groups with respect to the azide groups is in the order of 1 to 10, respectively, provided both thiols assemble similar.

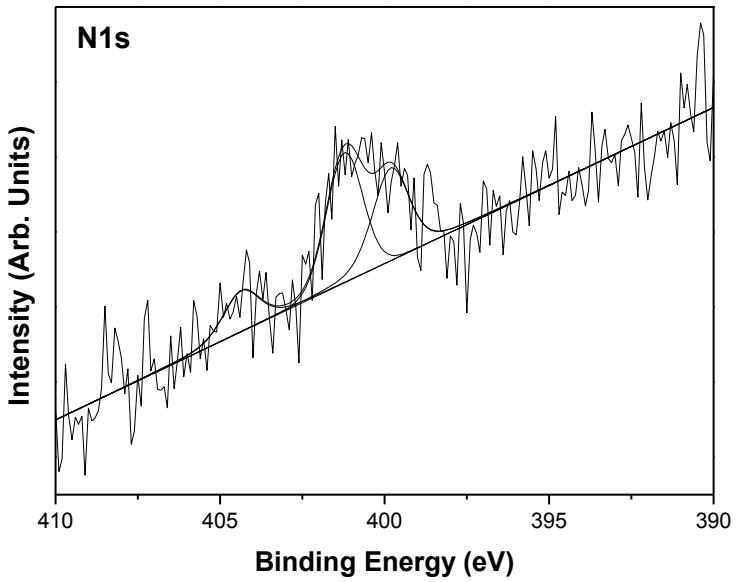

Figure 5.11. X-ray photoelectron spectrum of the N 1s core level region of the 1:10 mixed monolayer of 11-azidoundecane-1-thiol and 1-decanethiol before the click reaction and fit of the experimental lines.

Once the mixed monolayer was prepared we performed the 1,3-dipolar cycloaddition reaction between the mixed azide monolayer and the dialkyne-motor **5.2**. Water contact angle of the motor surface gave a value of 85±1°. XPS data from this motor surface showing the N 1s, S 2p and C 1s core level regions are presented in Figures 5.12, 5.13 and 5.14.

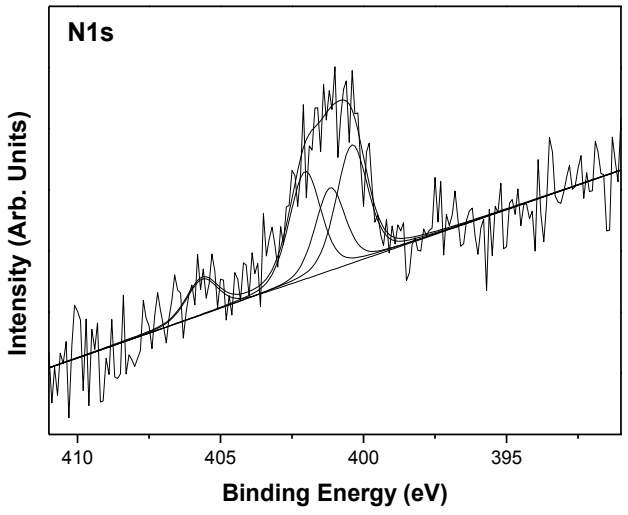

Figure 5.12. X-ray photoelectron spectrum of the N 1s core level region of the 1:10 mixed monolayer of 11-azidoundecane-1-thiol and 1-decanethiol after the click reaction and fit of the experimental lines.

The spectrum of the N 1s core level region for the grafted motor molecule (Figure 5.12) has four components; the first three at binding energies of 400.5 eV, 401.2 eV and

402.1 eV, corresponding to the three nitrogens from the triazole group. In addition there is still a peak at 405.2 eV corresponding to unreacted azides still present on the surface [17, 23-25].

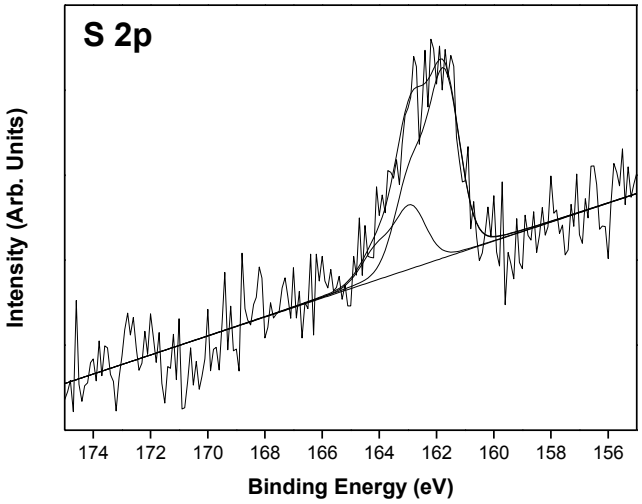

Figure 5.13. X-ray photoelectron spectrum of the S 2p core level region of the 1:10 mixed monolayer of 11-azidoundecane-1-thiol and 1-decanethiol after the click reaction and fit of the experimental lines.

Figure 5.13 presents the S 2p core level region. The fitting of the experimental lines was done by a combination of doublets with a spin-orbit splitting of 1.18 eV [26]. The main peak at a binding energy of 162.0 eV corresponds to sulfur attached to gold [26-28]. The second component at 163.8 eV can be assigned to alkanethiol molecules not bound to the gold surface but only physisorbed [29].

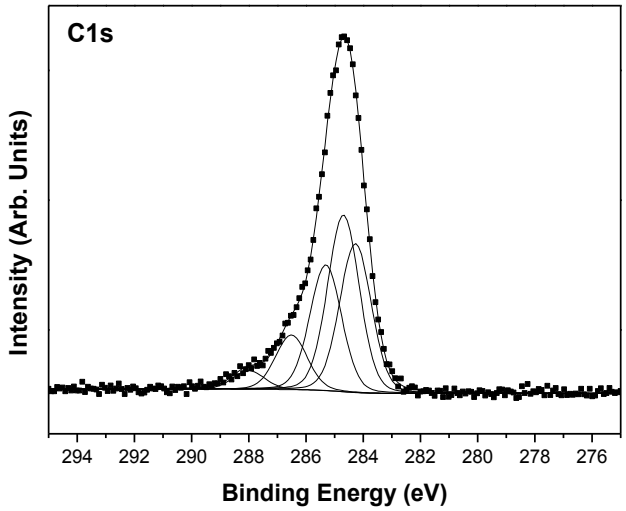

Figure 5.14. X-ray photoelectron spectrum of the C 1s core level region of the 1:10 mixed monolayer of 11-azidoundecane-1-thiol and 1-decanethiol after the click reaction and fit of the experimental lines.

We can clearly see the attachment of the molecular motor onto the functionalized gold surface from the C 1s XPS spectrum shown in Figure 5.14. In fact the C 1s line contains at least five carbon components that we can assign as follows: the peak at the lowest binding energy, 284.6 eV, corresponds to the phenyl groups in the motor molecule. The next peak at 285 eV belongs to the aliphatic carbons from the mixed monolayer and the legs of the motor molecule. The peak with a binding energy of 285.6 eV is assigned to the C-N bonds from the triazole ring and the unreacted azide groups, while the contribution at 286.8 eV arises from carbon attached to sulfur. The peak at the highest binding energy stems from carbon attached to oxygen [26].

The XPS measurements are a clear evidence of the successful attachment of the dialkyne-motor **5.2** to a mixed monolayer of 11-azidoundecane-1-thiol and 1-decanethiol (ratio 1:10) via copper (I) catalysed 1,3-dipolar cycloaddition reaction. However, there is no evidence that the motor is still able to rotate after surface attachment. UV-vis spectroscopy measurements on a semitransparent gold surface did not show any rotation after the motor surface was irradiated for 30 min (365 nm, 253 K, N_2 atmosphere) (data not shown). It could be that the absorption of gold overwhelmed the peak signal of the motor. Despite the careful blanking and sample preparations, UV/Vis spectra of the dialkyne-motor **5.2** grafted to a mixed monolayer of 11-azidoundecane-1-thiol and 1-decanethiol (ratio 1:10) via copper (I) catalysed 1,3-dipolar cycloaddition reaction could not be detected.

5.3.2 On silicon oxide: Dialkyne-motor 5.2 attached to azide-terminated SAM

a) Using a monolayer of 11-azidoundecyltrimethoxysilane

We prepared the monolayer as explained in Chapter 4 and then performed the click reaction (see section 5.2.3a). Immediately after this the sample was analysed by XPS to verify whether the molecular motor was indeed grafted onto the self-assembled monolayer, as sketched below in Figure 5.15.

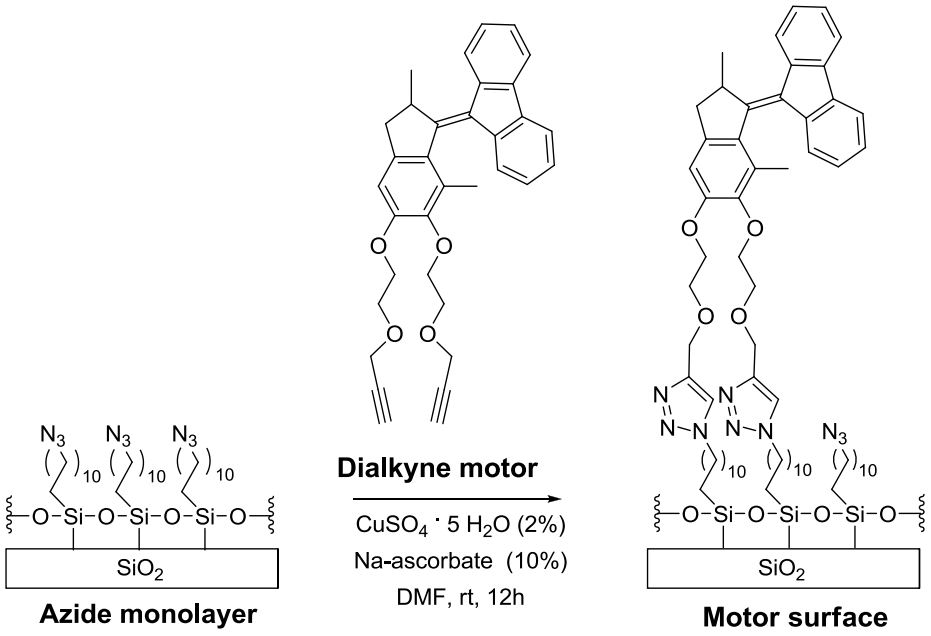

Figure 5.15. Scheme of the copper (I) catalysed 1,3-dipolar cycloaddition reaction to attach the dialkyne-motor **5.2** to the azide monolayer on SiO_2.

The XPS spectrum of N 1s after the reaction of the azide monolayer with the dialkyne-motor **5.2** via the 1,3-dipolar cycloaddition, shown in Figure 5.16a, shows the effective disappearance of the peak at 405.0 eV to the level of noise The broadening of the N1s peak at 400.7 eV testifies to the presence of chemically distinct nitrogen atoms (Figure 5.16a, lower panel).

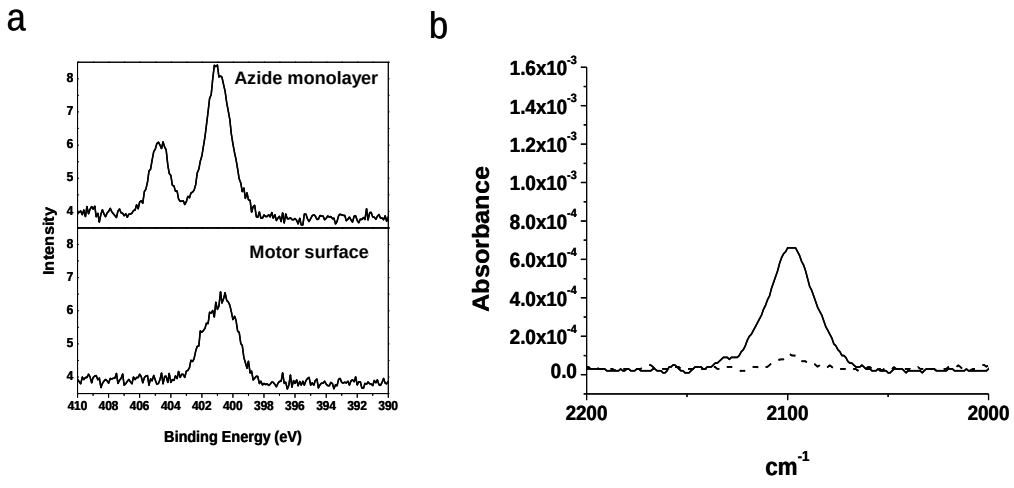

Figure 5.16. (a) XPS spectra of the N1s core level region of 11-azidoundecyltrimethoxysilane self-assembled monolayer on a silicon surface before (upper panel) and after (lower panel) attachment of the dialkyne-motor **5.2**; (b) IR-spectrum of an azide functionalized silica surface before (solid line) and after (dashed line) attachment of dialkyne-motor **5.2**. The attenuation of the azide signal indicates that the interfacial click-reaction has taken place [30].

To further support the covalent attachment, attenuated total reflectance infrared (ATR-FTIR) spectroscopy was performed on the surface with the dialkyne-motor **5.2** attached by "click chemistry". Comparison of the spectra before and after reaction, presented in figure 5.16b, clearly shows a strong decrease in the band at 2095 cm^{-1} which corresponds to the antisymmetric stretching mode of the azide group [31-33].

The combined results of XPS and ATR-FTIR together with the resistance to repeated cycles of sonication and washing strongly indicate that the motors are covalently bound to the interface.

To confirm that the rotary function of the molecules is preserved when they are bound to the surface, the attached dialkyne-motor **5.2** was irradiated with UV light (365 nm, 253 K, N_2 atmosphere). Irradiation for 30 min of the surface with the dialkyne-motor **5.2** attached led to a red shift in the long-wavelength absorption, as shown in Figure 5.17, similarly to what is observed for the dialkyne-motor **5.2** in solution [30]. Allowing the substrate to warm to room temperature restored the original UV-vis spectrum (■ in Figure 5.17), indicating that the thermal helix inversion regenerated stable dialkyne-motor **5.2** attached to the surface. Such observations are consistent with the behaviour of the dialkyne-motor **5.2** in solution [30]. In addition, irradiation (365 nm, MeOH, room temperature, 30 min) of a solution of the dialkyne-motor **5.2** in the presence of 11-azidoundecyltrimethoxysilane did not cause any change in the motor structure [30].

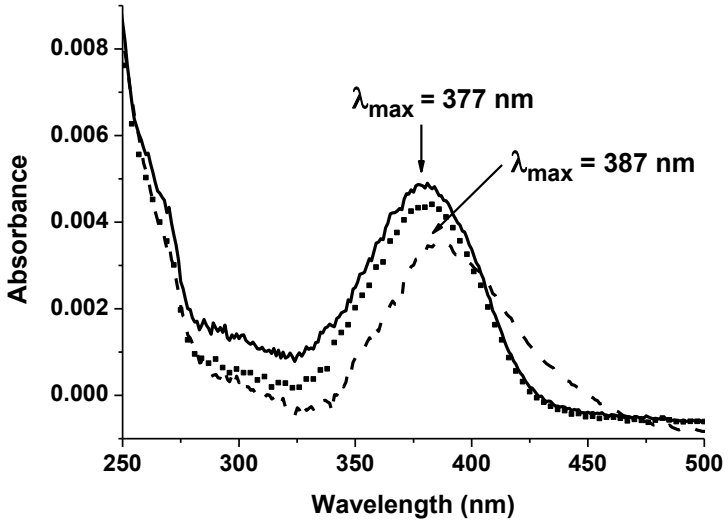

Figure 5.17. UV-vis spectrum of the surface bound dialkyne-motor **5.2** before (solid line) and after (dashed line) irradiation at λ_{max}= 365 nm. The shift in the spectrum upon irradiation and the reversion of the spectrum after standing at room temperature (30 min) (■) indicates that the rotary function is preserved upon surface attachment [30].

The results presented here show that the Cu-catalysed 1,3-dipolar cycloaddition reaction provides a versatile approach to attach molecular motors to silicon oxide surfaces. When azide motors are attached to alkyne surfaces, both XPS and IR signals show the covalent attachment of the dialkyne-motor **5.2**. Moreover, UV-vis spectroscopy proves the rotary function of the dialkyne-motor **5.2** after surface attachment.

5.4 Direct attachment of molecular motors to surfaces

5.4.1 Dialkyne-motor 5.2 on gold

Yoo *et. al* [22] reported triazole formation in self-assembled monolayers of 1,4-diethynylbenzene on Ag and Au surfaces via "click" cyclization. The authors reported that anchoring an aromatic ring via an alkynyl group may have the advantage of providing a p-conjugated linkage to the gold surface [22]. The authors prepared acetylenyl-anchoring and aromatic-terminated self-assembled monolayers (SAMs) of 1,4-diethynylbenzene on gold. After the fabrication of pendent acetylenyl SAMs, the formation of 1,2,3-triazoles was performed via copper (I)-catalysed Huisgen 1,3-dipolar cycloaddition "click chemistry."

We explored the acetylenyl-anchoring to the gold surface, anchoring a di-alkyne molecular motor to the bare gold surface following the procedure of Yoo *et. al* [22] (see section 5.2.3c). The scheme of the procedure is represented in Figure 5.18. To prove the anchoring of the dialkyne-motor to the gold surface XPS measurements were performed before and after the anchoring procedure.

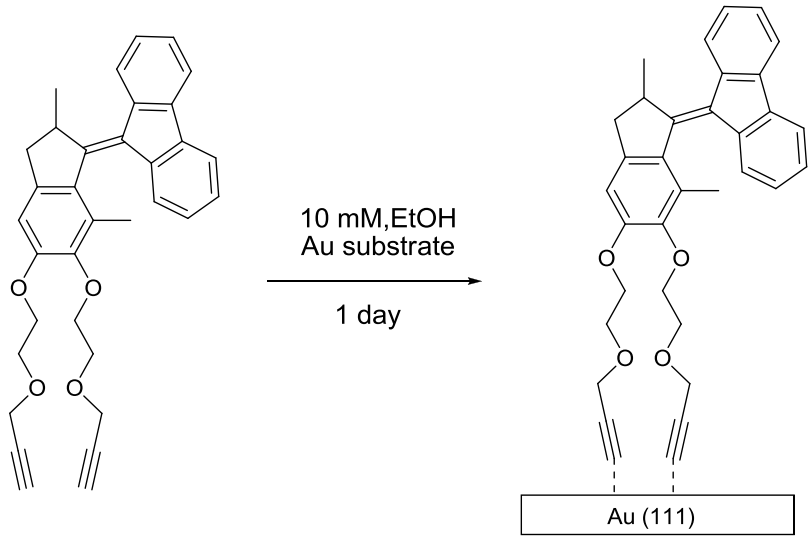

Figure 5.18. Scheme of the direct attachment of the dialkyne-motor on a gold surface.

Figure 5.19 presents the survey spectrum for the as-prepared gold substrate (upper panel) and after the exposure to the dialkyne-motor solution (lower panel). If we compare the spectra, we can see the appearance of a carbon peak after the attachment of the dialkyne-motor to the surface. To prove that this increase in carbon content corresponds to the di-alkyne molecular motor we collected a detailed spectrum of C 1s core level region for the motor functionalized surface, which is shown in Figure 5.20.

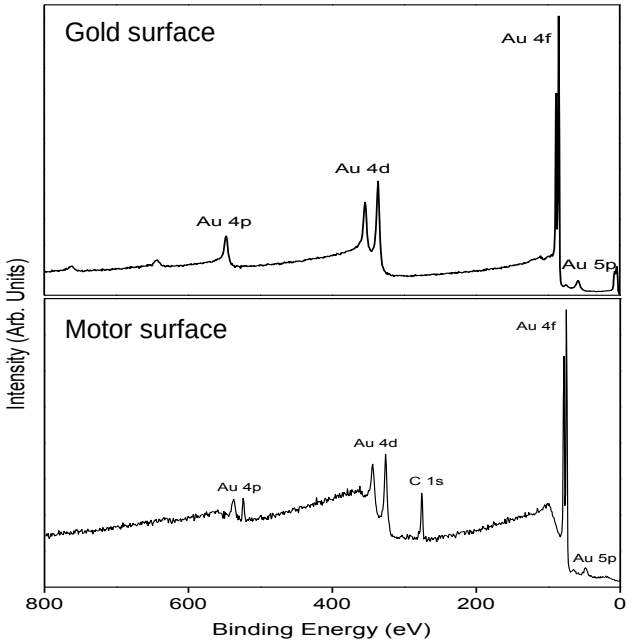

Figure 5.19. XPS survey spectra of a freshly prepared substrate of gold on mica (upper panel) and of the gold substrate after 24h exposure to the dialkyne-motor solution (lower panel).

From the fit of the experimental data we see that the C 1s line contains at least four carbon components (see Figure 5.19): the first at 284.5 eV corresponds to the phenyl groups in the motor molecule, the second at 285.3 eV is attributed to the aliphatic carbons in the motor. The contribution at a binding energy of 286.6 eV is assigned to the C-O bonds from the legs of the molecule and the peak at the highest binding energy of 289.0 eV originates from carbon attached to oxygen from traces of solvent in the sample [26].

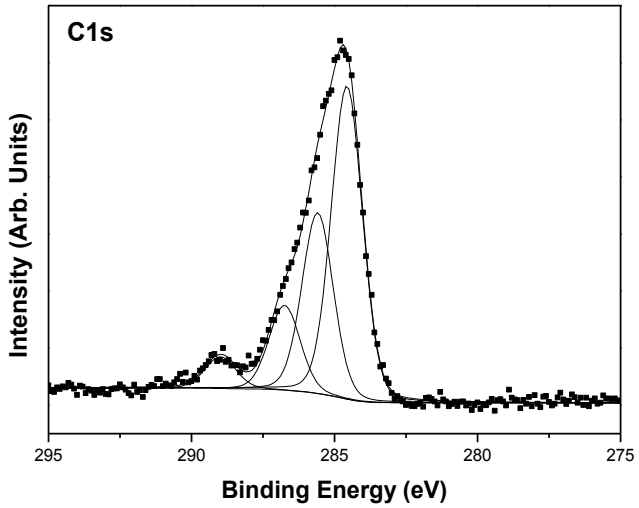

Figure 5.20 X-ray photoelectron spectrum of the C 1s core level region of the dialkyne-motor grafted on a gold substrate.

This clearly proves the attachment of the dialkyne-motor to the gold surface. However, there is no evidence that the motor is still able to rotate after surface attachment. UV-vis spectroscopy measurements on a semitransparent gold surface did not show any rotation after the motor surface was irradiated for 30 min (365 nm, 253 K, N_2 atmosphere) (data not shown). We can make two assumptions: 1) the altitudinal molecular motors monolayer is well packed and due to steric interactions it cannot perform rotation of the upper half. 2) the motors monolayer is not well packed and the molecules cannot stand, not letting the upper half rotate after irradiation.

5.4.2 Diol-motor 5.1 on silicon oxide

Silane compounds used for surface modification of quartz or silicon can undergo side-reactions due to their hydrolytic instability. These side-reactions might lead to the formation of oligomers and polymers and ultimately result in the formation of complex surface structures and multilayered polymer films. Since alcohols cannot undergo such side-reactions, surface modification through alkoxylation is expected to form more uniform monolayers [30].

A number of methods have been described for attachment of alcohols to siliceous surfaces [34-37]. Most involve the activation of the surface through the formation of a Si-X (X= Cl, Br, I, NEt_2) bond as the first step. A common drawback of Si-O-C bonds is their hydrolytic instability [38]. It has been shown that this can be improved by blocking the free surface Si-X (X= Cl, Br, I) groups with hexamethyldisilazane (HMDS) following surface modification or by using alcohols with bulky backbones to sterically hinder attack by water [39].

From the methods available we chose the one applied by Schreiber and coworkers to create microarrays for testing interactions between proteins and small molecules [35]

(Figure 5.21). They found that among the variety of chlorination conditions available the $SOCl_2$/DMF/THF system gives the best results. The method is attractive due to the application of bench-stable chemicals avoiding highly water sensitive or difficult-to-handle reagents such as Cl_2 or $SiCl_4$. This activation method was also used by others to modify porous silica for drug release applications [40-41].

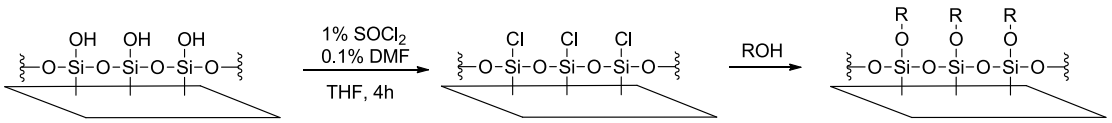

Figure 5.21. Method for surface-modification with primary alcohols via surface activation with $SOCl_2$ [35].

Following the procedure reported in the literature [35] it was expected that diol-motor **5.1** (for the synthesis see section 5.6.1) with two terminal OH-groups will readily react with chlorinated quartz surfaces (Figure 5.22).

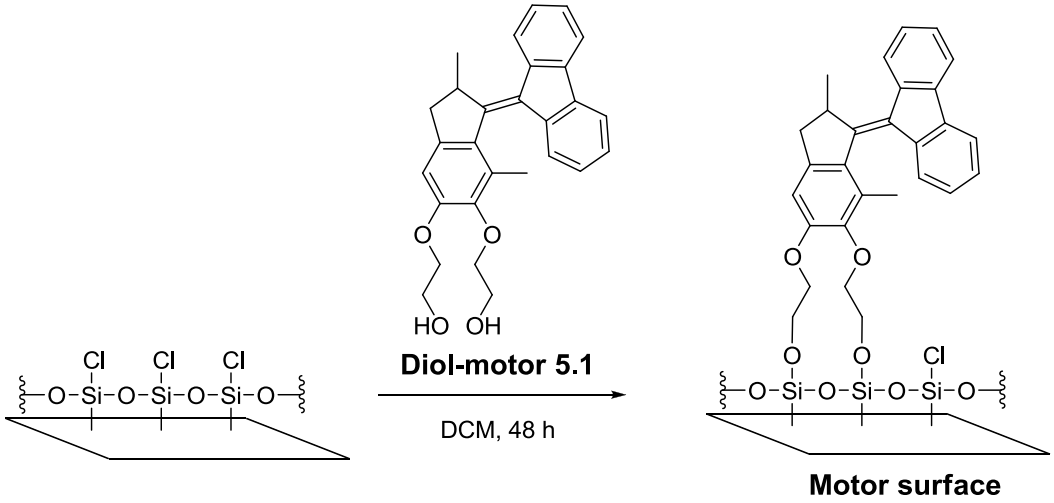

Figure 5.22. Attachment of diol-motor **5.1** to chlorinated quartz and silicon oxide surfaces [30].

Chlorinated surfaces were prepared according to the procedure described by Schreiber and coworkers [35]. Piranha-cleaned quartz slides were immersed in a THF solution of $SOCl_2$ (1 %) and catalytic amount of DMF (0.1 %) for 5 h followed by rinsing with dry THF (3 times).

Slides were immersed in a DCM solution of diol-motor **5.1** for 40-48 h then rinsed with DCM (3 times) and dried in a stream of argon.

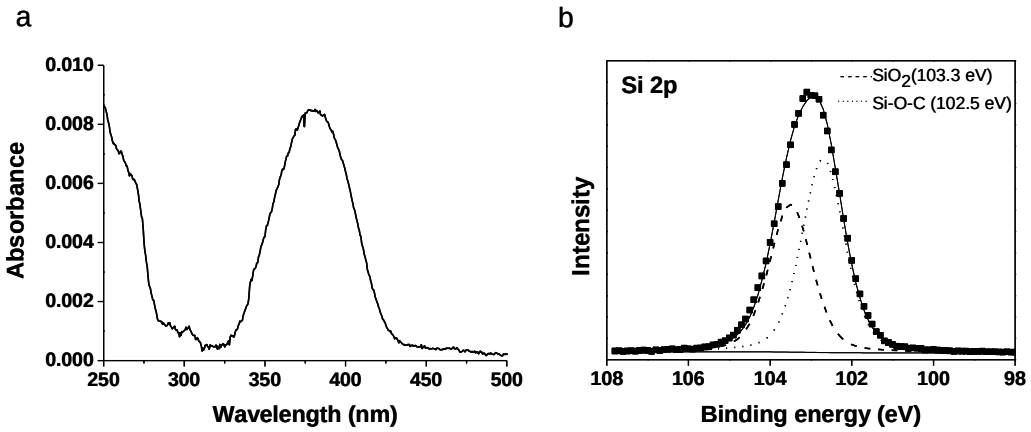

Figure 5.23. UV-vis (a) and XPS (b) spectra of quartz and silicon surfaces after the attachment of diol-motor **5.1**. Although the presence of motors could be detected by these methods, the procedure for surface modification turned out to be irreproducible.

The UV-vis absorption spectrum of the slide showed the absorption spectrum expected for the motor (Figure 5.23a). Furthermore XPS measurements support the motor attachment also (Figure 5.23b). However, despite these promising initial results, the assembly was difficult to reproduce and not suitable for routine use. Further attempts to prepare motor-modified slides in this way mostly resulted in UV-vis signals only slightly above the detection limit indicating the lack of well packed monolayers.

The difficulties could be due to the hydrolytic instability of either the motor monolayer or the chlorinated surface or both.

As a control experiment assembly of 1-octadecanol on quartz was performed under identical conditions. The water contact angle of the resulting layer was around 50-60° instead of ~110°, which is the characteristic contact angle for well-packed octadecyl-monolayers [37].

Based on these results different surface-activation methods [36-37] should be considered for the preparation of high-coverage monolayers of alcohol-functionalized molecular motors.

5.5 Conclusions

Molecular motors were grafted to surfaces via 1,3 dipolar cycloaddition reaction of azides with alkynes. Dialkyne-motor **5.2** was successfully grafted on gold surfaces, previously covered with a mixed self-assembled monolayer of 11-azidoundecane-1-thiol and 1-decanethiol with a ratio 1:10. After surface attachment the motor surface preserved the rotary function. This grafting method can therefore be considered a versatile approach to assemble motors on surfaces.

We also attempted to assemble dialkyne-motor **5.2** directly on gold surfaces but the acetylenyl-anchoring to the gold surface was not successful for these molecules. Direct attachment of diol-motor **5.1** on silicon oxide using chlorinated functionalized surfaces was difficult to reproduce and not suitable for routine use.

5.6 Appendix: Synthesis of compounds (by Dr. G. London)

a) Synthesis Diol-motor 5.1

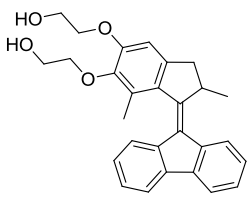

A solution of diester-motor [30] (90 mg, 0.21 mmol) in THF (5 mL) was added to a suspension of $LiBH_4$ (22 mg, 1 mmol) in THF (3 mL) and the mixture was stirred at rt for 20 h. The reaction was quenched with aqueous HCl solution (5 mL, 0.1 M) and the mixture was extracted with EtOAc until the aqueous phase was colourless. The combined organic layers were washed with water (20 mL) and brine (20 mL) and dried (Na_2SO_4). The solvent was evaporated under reduced pressure and the crude product was recrystallized from toluene : *n*-heptane (5 : 1) to give yellow crystals (70 mg, 0.14 mmol, 67 %). M.p. 187.5-188.0°C. ^{1}H NMR (500 MHz, DMSO-d_6) δ 1.26 (d, *J* = 6.5 Hz, 3H), 2.10 (s, 3H), 2.55 (d, *J* = 15.0 Hz, 1H), 3.24 (dd, *J* = 5.8, 14.8 Hz, 1H), 3.71 (q, *J* = 5.5 Hz, 2H), 3.80 (q, *J* = 5.5 Hz, 2H), 3.92-3.96 (m, 1H), 4.03 (quin, *J* = 6.5 Hz, 1H), 4.06-4.10 (m, 1H), 4.12-4.17 (m, 2H), 4.80 (t, *J* = 5.0 Hz, 1H, O*H*), 4.93 (t, *J* = 5.0 Hz, 1H, O*H*), 7.06 (s, 1H), 7.17 (t, *J* = 7.8 Hz, 1H), 7.26-7.31 (m, 2H), 7.35-7.40 (m, 2H), 7.83 (d, *J* = 7.0 Hz, 1H), 7.87 (d, *J* = 7.5 Hz, 1H), 7.91-7.93 (m, 1H); ^{13}C NMR (APT, 125 MHz, $CDCl_3$) δ 15.9, 18.9, 41.5, 44.8, 61.0, 62.1, 70.5, 108.0, 119.2, 119.6, 123.2, 123.7, 126.4, 126.7, 126.8, 126.9, 129.1, 131.9, 134.0, 137.8, 139.3, 139.5, 139.6, 143.9, 145.4, 151.5, 152.3. (1 C not observed due to overlap.) HRMS (EI) calcd for $C_{28}H_{28}O_4$ 428.1987, found 428.1998 [30].

b) Synthesis of Dialkyne-motor 5.2

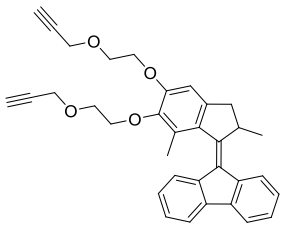

A suspension of NaH (30 mg, 1.3 mmol) in THF (3 mL) was cooled to 0°C and a solution of diol-motor **5.1** (67 mg, 0.16 mmol) in THF (7 mL) was added dropwise (under N_2 atmosphere). To this mixture propargyl bromide (50 µL, 0.45 mmol, 80 % in toluene) was added. The solution was stirred at rt for 12 h. The reaction was quenched with water (10 mL) and the mixture was extracted with EtOAc until the yellow colour of the aqueous phase had disappeared. The organic phase was washed with water (10 mL) and brine (10 mL) and dried (Na_2SO_4). The solvent was evaporated under reduced pressure and the crude product was recrystallized from *n*-heptane to give yellow crystals (55 mg, 0.11 mmol, 69 %). M.p. 138.0-139.0°C; ^{1}H NMR (400 MHz, $CDCl_3$) δ 1.32 (d, *J* = 6.8 Hz, 3H), 2.20 (s, 3H), 2.43 (t, *J* = 2.0 Hz, 1H), 2.49 (t, *J* = 2.4 Hz, 1H), 2.53 (d, *J* = 14.8 Hz, 1H), 3.29 (dd, *J* = 5.8, 14.6 Hz, 1H), 3.91 (t, *J* = 4.6 Hz, 2H), 3.98 (t, *J* = 4.2 Hz, 2H), 4.09-4.16 (m, 2H), 4.21-4.36 (m, 3H), 4.31 (dd, *J* = 0.6, 2.2 Hz, 2H), 4.32 (dd, *J* = 0.8, 2.4 Hz, 2H), 6.84 (s, 1H), 7.11 (t, *J* = 7.4 Hz, 1H), 7.23 (t, *J* = 7.4 Hz, 1H), 7.33-7.37 (m, 3H), 7.75 (d, *J* = 7.2 Hz, 1H), 7.80-7.82 (m, 1H), 7.85-7.87 (m, 1H); ^{13}C NMR (APT, 100 MHz, $CDCl_3$) δ 16.0, 19.0, 41.5, 44.8, 58.3, 58.6, 68.00, 68.2, 69.3, 71.5, 74.5, 74.7, 108.3, 119.1, 119.6, 123.5, 123.6, 126.5, 126.5, 126.7, 128.9, 131.9, 133.8, 137.8, 139.1, 139.6, 143.2, 145.7, 152.0, 152.6. (4 C not observed due to overlap.) HRMS (EI) calcd for $C_{34}H_{32}O_4$ 504.2301, found 504.2286 [30].

5.7 References

1. B.L. Feringa, *J. Org. Chem.* **2007**, *72*, 6635.
2. C. Vericat, M.E. Vela, G.A. Benitez, J.A. Martin Gago, X. Torrelles, R.C. Salvarezza, *J. Phys.-Condens. Mat.* **2006**, *18*, R867.
3. C.D. Bain, E.B. Troughton, Y.T. Tao, J. Evall, G.M. Whitesides, R.G. Nuzzo, *J. Am. Chem. Soc.* **1989**, *111*, 321.
4. M. Zharnikov, M. Grunze, *J. Phys.-Condens. Mat.* **2001**, *13*, 11333.
5. V. Balzani, A. Credi, M. Venturi, European Journal of Chemical Physics and Physical Chemistry **2008**, *9*, 202.
6. J. Berná, D. A. Leigh, M. Lubomska, S. M. Mendoza, E. M. Pérez, P. Rudolf, G. Teobaldi and F. Zerbetto, *Nature Materials* **2005**, *4*, 704.
7. M. M. Pollard, M. Lubomska, P. Rudolf, B. L. Feringa, *Angew. Chem., Int. Ed.* **2007**, *46*, 1278.
8. M. K. J. ter Wiel, B. L. Feringa, *Synthesis* **2005**, 1789
9. D. H. Qu, B. L. Feringa, *Angew. Chem. Int. Ed.* **2010***, 49*, 1107.
10. M. M. Pollard, A. Meetsma, B. L. Feringa, *Org. Biomol. Chem.* **2008***, 6*, 507.
11. Koumura, N., Geertsema, E.M., Meetsma, A., Feringa, B.L., *J. Am. Chem. Soc.* **2000**, 12005.
12. C. Kolb, H. K. B. Sharpless, *Drug Discov. Today* **2003**, *8*, 1128.

13. W. H. Binder, C. Kluger, *Curr. Org. Chem.* **2006**, *10*, 1791.
14. W. H. Binder, R. Sachsenhofer, *Macromol. Rapid Commun.* **2007**, *28*, 15.
15. H. Nandivada, X. W. Jiang, J. Lahann, *Adv. Mater.* **2007**, *19*, 2197.
16. J. P. Collman, N. K. Devaraj, C. E. D. Chidsey, *Langmuir* **2004**, *20*, 1051.
17. J. P. Collman, N. K. Devaraj, T.P.A. Eberspacher, C.E.D. Chidsey, *Langmuir* **2006**, 2457.
18. J. K. Lee, Y. S. Chi, I. S. Choi, *Langmuir* **2004**, *20*, 3844.
19. M. A. White, J. A. Johnson, J. T. Koberstein, N. J. Turro, *J. Am. Chem. Soc.* **2006**, *128*, 11356.
20. S. Prakash, T. M. Long, J. C. Selby, J. S. Moore, M. A. Shannon, *Anal. Chem.* **2007**, *79*, 1661.
21. R. Chelmowski, D. Kafer, S. D. Koster, T. Klasen, T. Winkler, A. Terfort, N. Metzler-Nolte, C. Woll, *Langmuir* **2009**, *25*, 11480.
22. B. K. Yoo, S.-W Joo, *J. Colloid Interface Sci.* **2007**, *311*, 491.
23. London, G., Carroll, G.T., Fernández Landaluce, T., Pollard, M.M., Rudolf, P., Feringa, B.L., *Chem. Commun.* **2009**, *13*, 1712.
24. Wollman, E.W., Kang, D., Frisbie, C.D., Lorkovic, I.M., Wrighton, M.S., *J. Am. Chem. Soc.* **1994**, 4395.
25. A. Devadoos, C.E.D. Chidsey, *J. Am. Chem. Soc.* **2007**, *129*, 5370.
26. J. F. Moulder, W. F. Stickle, P. E. Sobol, and K. D. Bomben, *"Handbook of X-ray photoelectron Spectroscopy"*, **1995**, Physical Electronics Inc. Eden Prairie, Minnesota.
27. P. E. Laibinis, C. D. Bain, G. M. Whitesides, *J. Phys. Chem.* **1997**, *95*, 7017.
28. A.-S. Duwez, J. Electron Spectrosc. Relat. Phenom. **2004**, *134*, 97.
29. R. Arnold, W. Azzam, A. Terfort, C. Wöll, *Langmuir* **2002**, *18*, 3980.
30. G. London, "*Light-driven molecular motors and switches in confined environments*", Ph.D. thesis, University of Groningen, **2011**.
31. C.R. Kessel, S. Granick, *Langmuir* **1991**, *7*, 532.
32. G. E. Fryxell, P. C. Rieke, L. L. Wood, M. H. Engelhard, R. E. Williford, G. L. Graff, A. A. Campbell, R. J. Wiacek, L. Lee, A. Halverson, *Langmuir* **1996**, *12*, 5064.
33. A. Heise, M. Stamm, M. Rauscher, H. Duschner, H. Menzel, *Thin Solid Films* **1998**, *327*, 199.
34. D. K. Aswal, S. Lenfant, D. Guerin, J. V. Yakhmi, D. Vuillaume, *Anal. Chim. Acta* **2006**, *568*, 84.
35. P. J. Hergenrother, K. M. Depew, S. L. Schreiber, *J. Am. Chem. Soc.* **2000**, *122*, 7849.
36. C. M. Yam, S. S. Y. Tong, A. K. Kakkar, *Langmuir* **1998**, *14*, 6941.
37. X. Y. Zhu, V. Boiadjiev, J. A. Mulder, R. P. Hsung, R. C. Major, *Langmuir* **2000**, *16*, 6766.
38. H. Utsugi, H. Horikoshi, T. Matsuzawa, *J. Colloid Interface Sci.* **1975**, *50*, 154.
39. G. C. Ossenkamp, T. Kemmitt, J. H. Johnston, *Langmuir* **2002**, *18*, 5749.
40. C. Eckertlill, N. A. Lill, H. Rupprecht, *Coll. Polym. Sci.* **1987**, *265*, 1001.
41. C. Eckertlill, N. A. Lill, W. Endres, H. Rupprecht, *Drug Dev. Ind. Pharm.* **1987**, *13*, 1511.

Chapter 6

Towards ultrafast light-driven molecular motors on surfaces

In this chapter the synthesis and surface assembly of ultrafast light-driven azimuthal molecular motors is presented. Several grafting pathways were explored for the attachment of these ultrafast rotary molecular motors on silicon oxide and gold surfaces. The in-depth analysis provides a useful guide for future assembly of light-driven molecular motors on surfaces.

6.1 Introduction

One of the crucial steps towards the use of motion generated by synthetic light-driven rotary molecular motors to perform useful tasks is to make their rotary action fast enough to compete with the surrounding Brownian motion and convert energy into controlled motion. As explained in Chapter 3 the design of the molecular motor structure is a key factor to achieve a high rotation speed [1-5].

In the study reported in this chapter the basic ultrafast azimuthal motor structure (Figure 6.1) was designed building on the ultrafast motor with a tetra-substituted carbon stator which was measured to have a speed of 45 MHz [6]. For ease of synthesis, the stator was extended with ester legs. These legs are good handles for modifications in different grafting routes and various surfaces. The first pathway (Figure 6.1 left) is based on the "click" chemistry between azide-modified surfaces either on silicon oxide or gold with alkyne-legged motor. The click chemistry saves synthetic steps for potential attachment of functionalized motors as explained in Chapter 5.

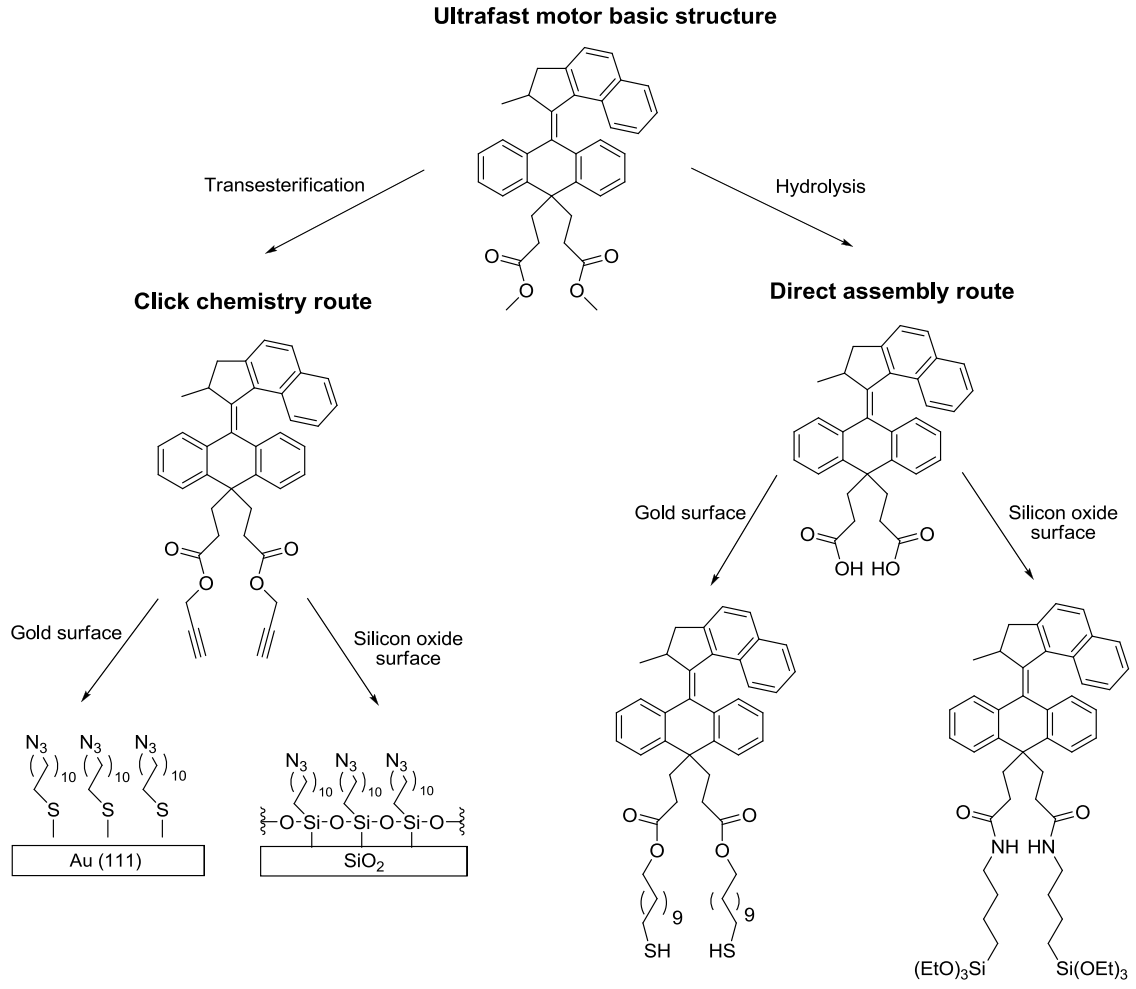

Figure 6.1. Different methods for grafting ultrafast motors on gold and silicon oxide surfaces.

The other pathway (Figure 6.1 right) is the direct attachment route. While the number of synthetic steps is increased the attachment is more direct, meaning that simple literature-based conditions are enough to graft the molecules to the surface as long as the correct legs are synthesized. Direct self-assembly of thiols on gold and of silanes on silicon oxide will be reported here as new routes for surface attachment of rotary molecular motors.

6.2 Experimental Procedures

6.2.1 Substrate preparation

The gold and silicon substrates were prepared as explained in Chapter 2.

6.2.2 Preparation of self-assembled monolayers

a) 11-azidoundecane-1-thiol self-assembled monolayer

The 11-azidoundecane-1-thiol SAMs on Au were prepared as described in Chapter 5.

b) 11-azidoundecyltrimethoxysilane self-assembled monolayer

The 11-azidoundecyltrimethoxysilane SAMs on silica substrates were prepared as described in Chapter 4.

6.2.3 Motor attachment

a) Copper (I) catalysed azide-alkyne cycloaddition

Copper (I) catalysed azide-alkyne cycloadditions reactions were performed as described in Chapter 5.

b) Self-assembly of dithiol-motor 6.10 on a gold surface

A solution 1 mM of the dithiol-motor **6.10** (see synthesis in appendix 6.7.5) in a mixture ratio 1:2 of ethanol:DCM was prepared. Freshly prepared gold substrates were left in the solution for 2 days. The samples were taken out of the solution just before further use. They were rinsed in fresh ethanol and dried under argon flow.

c) Assembly of diacid-motor 6.8 on a silicon oxide surface

Diacid-motor **6.8** (see synthesis in appendix 6.7.3) was reacted with triethoxysilane-propylamine with PyBop and DIPEA in DMF/DCM overnight. A freshly cleaned quartz/SiO_2 surface was then immersed into the reaction mixture overnight. Thorough rinsing with DCM and ethanol to remove any adsorbed molecules, and drying with a stream of argon afforded the motor functionalized quartz/SiO_2 surface.

6.2.4 X-ray photoelectron spectroscopy measurements

The X-ray photoelectron spectra **(**XPS) were measured in a small spot photoelectron spectrometer of Surface Science Laboratories as explained in Chapter 2.

6.2.5 Contact angle measurements

The contact angle (CA) measurements were performed as detailed in Chapter 2.

6.3 Ultrafast motor: synthesis and solution characterization

The synthesis of the light-driven rotary molecular motors presented in this chapter was performed by Dr. T. Sasaki. The synthetic pathway of the basic structure of ultrafast azimuthal motor **6.6** is shown in Figure 6.2.

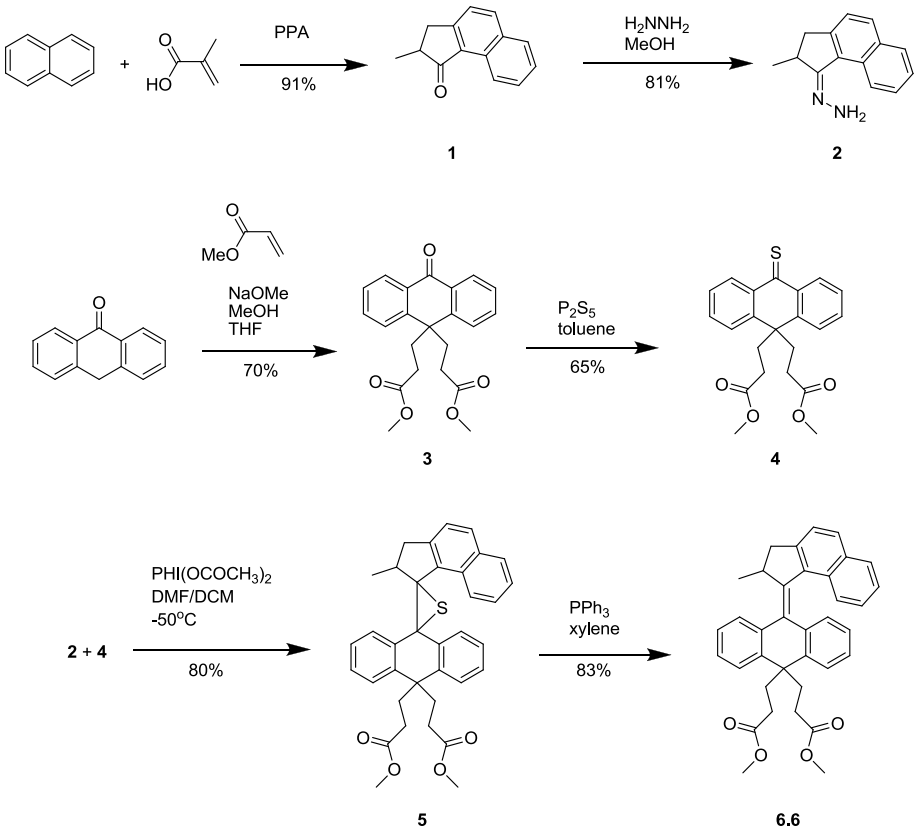

Figure 6.2. Synthetic route of the basic ultrafast azimuthal motor structure **6.6**.

As with the syntheses of many other light-driven motors, the design was divided up into two parts, the rotor and the stator. Rotor **2** was synthesized in a one-pot Friedel-Crafts acylation followed by a Nazarov cyclization from naphthalene to form the ketone **1**. This was then treated with a hydrazine monohydrate solution to form **2**. Stator **4** was designed and synthesized to have two ester groups as “legs” for surface

attachment. Having two "legs" allows the stator to be stationary relative to the spinning of the motor on surfaces. Using Barton-Kellog coupling conditions, **2** and **4** were coupled successfully to obtain episulfide **5** which was subsequently desulfurized to afford the final product **6.6**.

The rotational speed in solution was investigated for molecule **6.6**. A typical experiment involves low-temperature UV/Vis spectroscopy to trap the unstable-**6.6** form after the irradiation step before the stable-**6.6** form is regenerated. Given structural similarities between ultrafast motor **6.6** and ultrafast motors reported in literature [1], that temperatures in the range of 80 ~ 90 K are needed to trap the unstable-**6.6** form. Propane (melting point 85.5 K) is usually an appropriate solvent for low-temperature measurements but unfortunately when we tried it for our measurements, the ultrafast motor **6.6** precipitated out at low temperatures. We therefore tried with a mixed solvent obtained by adding a drop of DCM to propane; this mixed solvent dissolved the molecule but melted 90 ~ 100 K. This convinced us to change the strategy for measuring the rotational speed (t½ half-life). The approach used was ns-pulsed laser transient absorption (TA) spectroscopy[*], a technique typically employed to probe photoexcited state dynamics [7,7].

For the transient absorption experiment, we used a Nd:YAG laser delivering 3.6 mJ per pulse; the repetition rate of the laser pulses was 5 Hz, while the probe lamp was chopped at 10 Hz. In this way, the absorption of sample is measured before the laser pulse and a certain time after the laser pulse. The difference between the two spectra is calculated by the program, resulting in the transient absorption spectra. The time after the pulse was set to 1 ns steps (increment) and the spectra were collected for 98 steps. Each time interval was measured 50 times (accumulation) and then averaged to give the transient absoption spectra shown below in Figure 6.3a. The laser light was filtered out by using a 375 nm filter in front of the detector.

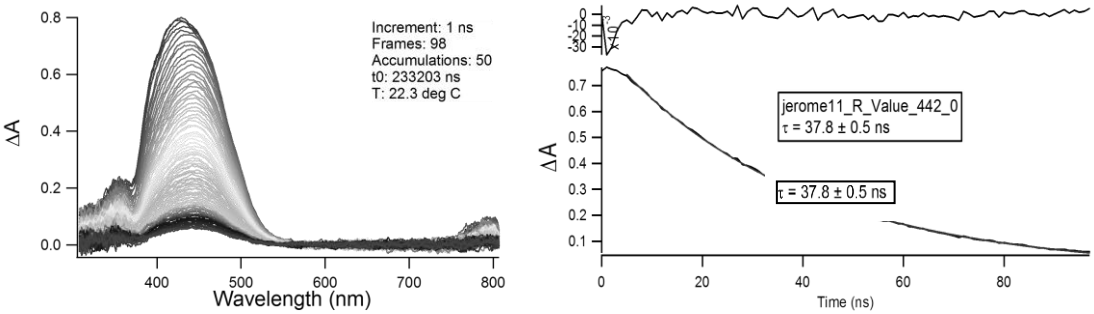

Figure 6.3. Transient absorption spectra of ultrafast motor **6.6** in *n*-hexane (a). Cut-through at 442 nm showing the decay of the transient absorption in time fitted mono-exponentially (b).

[*] Measurements performed by J. Siekierzycka at the group of Molecular Photonics at the University of Amsterdam.

Ultrafast motor **6.6** was dissolved in *n*-hexane (3 x 10^{-6} M) and λ_{max} was determined to be 355 nm (A_{355} = 1.07). After irradiation of **6.6**, the transient of the unstable-**6.6** form was observed. The half-life ($t_{½}$) was determined to be 40 ns, comparable to ultrafast motors reported in literature [6]. Decomposition was barely observed during the process providing evidence that ΔA were changes due to isomerisation changes and not due to photodegradation.

The functional basic ultrafast motor **6.6** was then modified with the desired ester legs for further grafting on the surface. While further synthetic changes are possible (rotor) for added solubility, the ultrafast motor **6.6** is a good base for the study of surface grafting processes.

6.4 Surface attachment: "click chemistry"

6.4.1 Ultrafast dialkyne-motor 6.7 on silicon oxide

We prepared an 11-azidoundecyltrimethoxysilane monolayer as explained in Chapter 4 and then performed the click reaction (see section 5.2.3a). Immediately after this the sample was analysed by XPS and contact angle measurements to verify whether the molecular motor was indeed grafted onto the self-assembled monolayer, as shown below in Figure 6.4.

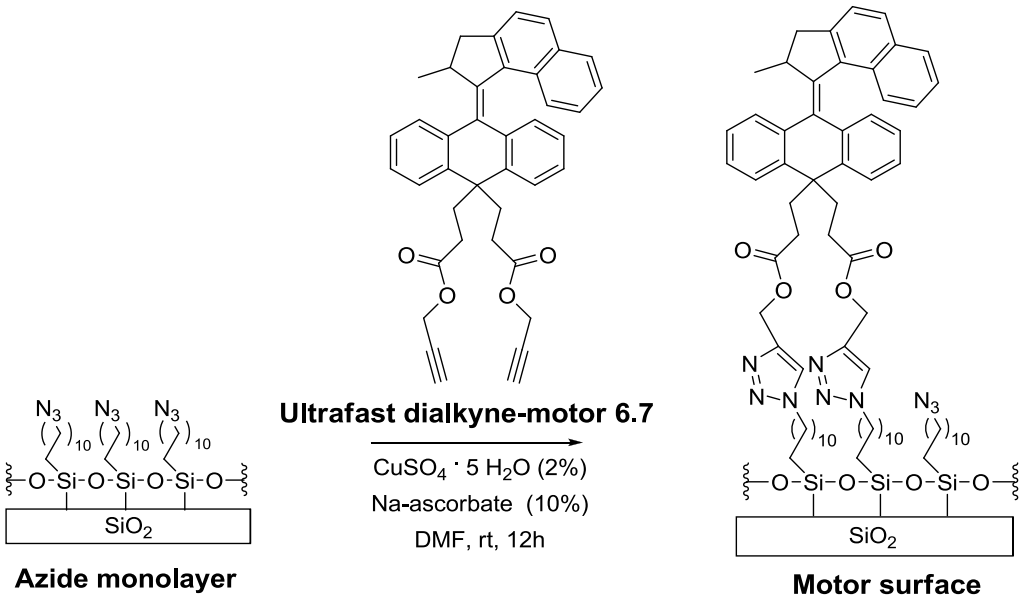

Figure 6.4. Scheme of the copper (I) catalysed 1,3-dipolar cycloaddition reaction to attach the ultrafast dialkyne-motor **6.7** to the azide monolayer on silicon oxide.

The measured contact angle of the azide surface was 77±1°; after the click reaction we observed a decrease in the contact angle to 65±2°, in agreement with reported values in the literature [9].

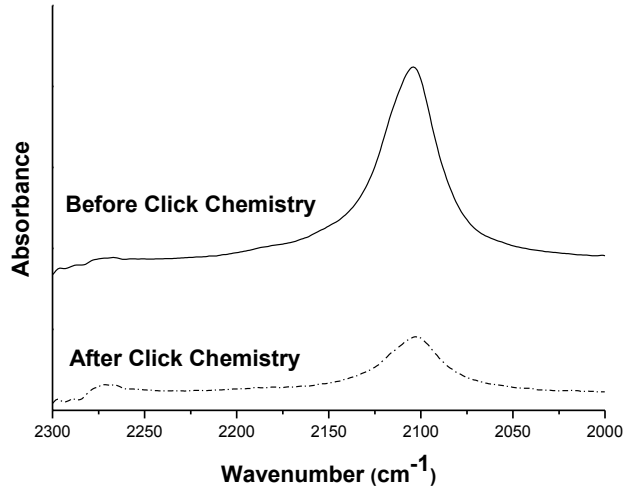

Figure 6.5. IR-spectrum of an azide functionalized silica surface before (solid line) and after (dotted line) attachment of ultrafast dialkyne-motor **6.7**. The attenuation of the azide signal indicates that the interfacial click-reaction has taken place.

Attenuated total reflectance infrared (ATR-FTIR) spectroscopy was performed on azide-terminated surface and on the surface with the ultrafast dialkyne-motor **6.7**. For the 11-azidoundecyltrimethoxysilane monolayer, the peak at 2100 cm^{-1} indicates the azide stretch vibration. On the surface modified by the motor, *i.e.* after the click chemistry reaction, the same peak had decreased significantly indicating that only very few unreacted azides remain on the surface. The comparison of the spectra (Figure 6.5) before and after reaction clearly indicates that the quartz surface was functionalized, and the click chemistry reaction was successfully performed with the ultrafast dialkyne-motor **6.7**.

XPS measurements were performed on the 11-azidoundecyltrimethoxysilane monolayer and on the motor surface after the click reaction. Note that a different substrate was prepared for the XPS measurements, since quartz surfaces are not conductive. The disadvantage of using a silicon wafer is that despite being the same functionalized surface, it is not transparent, so UV/Vis, IR, and CD measurements which are usually performed in transmission cannot be carried out.

The X-ray photoelectron spectrum of N 1s core level region of the 11-azidoundecyltrimethoxysilane monolayer is shown in Figure 6.6. The fit of the experimental lines shows three components. The peaks at 400.5 eV and at 401.1 eV correspond to neutral and electron-rich nitrogen atoms, respectively. The third component at 404.5 eV corresponds to the electron-deficient nitrogen atom in the azide group. The spectrum of the N 1s core level region for the grafted dialkyne-motor molecule (Figure 6.7) shows three components at binding energies of 399.9 eV, 400.7 eV and 401.9 eV, corresponding to the three nitrogens from the triazole group [10-13].

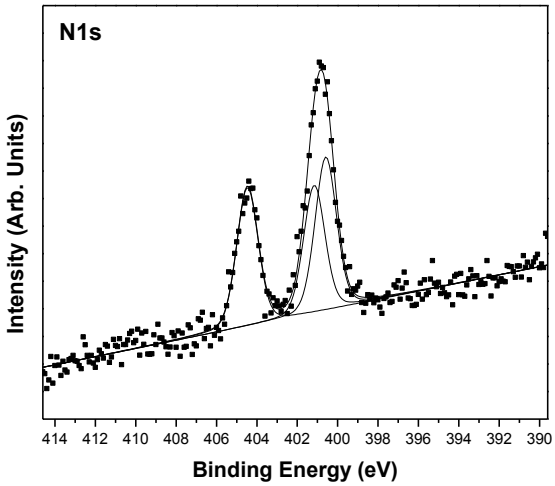

Figure 6.6. X-ray photoelectron spectrum of N 1s core level region of the 11-azidoundecyltrimethoxysilane monolayer and fit of the experimental lines.

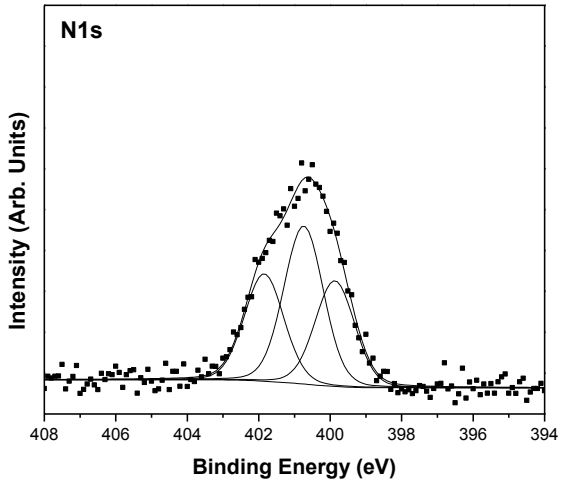

Figure 6.7. X-ray photoelectron spectrum of N 1s core level region of the motor surface on silicon oxide and fit of the experimental lines.

In contrast to the IR results, there is no fingerprint of traces of unreacted azides in the N1s region of the XPS spectrum for the motor-functionalized surface. The XPS data suggest that all the free azides reacted on the surface. These different conclusions drawn from the ATR-FTIR and XPS results regarding the efficiency of the click reaction can be explained by the fact that the area measured in ATR-FTIR is much larger than that probed by XPS. Thus if the surface is not completely uniform ATR-FTIR gives a different result from XPS.

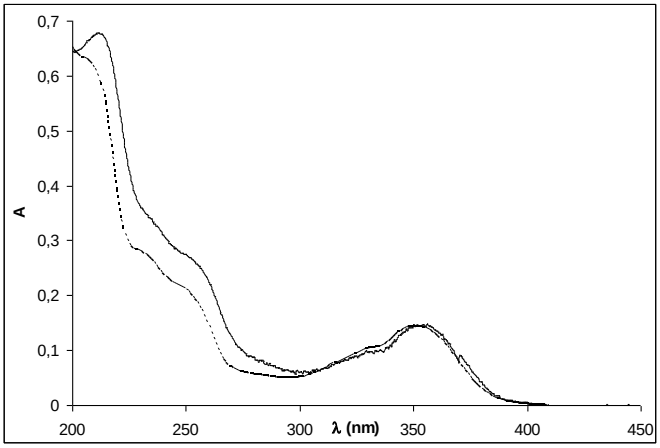

Figure 6.8. UV/Vis spectra of the dialkyne-motor **6.7** in solution (solid line) and grafted onto a quartz surface (dotted line) via a click reaction.

Figure 6.8 presents a comparison of UV/Vis spectra of the ultrafast dialkyne-motor **6.7** in solution and after being grafted onto a quartz surface. No significant differences in the spectra were observed. The motor absorption (λ_{max}=350 nm) was retained even after the surface assembly. When the sample was kept at temperatures in the range -20~20°C, photoirradiation with a 365 nm UV lamp induced no changes in the UV/Vis spectra; this is a good initial indication that molecular motor retains its rotational speed when grafted to the surfaces [10].

6.4.2 Ultrafast dialkyne-motor 6.7 on gold

We prepared a mixed self-assembled monolayer of 11-azidoundecane-1-thiol and 1-decanethiol with a ratio 1:10 as explained in Chapter 5. Subsequently the ultrafast dialkyne-motor **6.7** was grafted onto the surface via the copper (I) catalysed 1,3-dipolar cycloaddition reaction as illustrated in Figure 6.9.

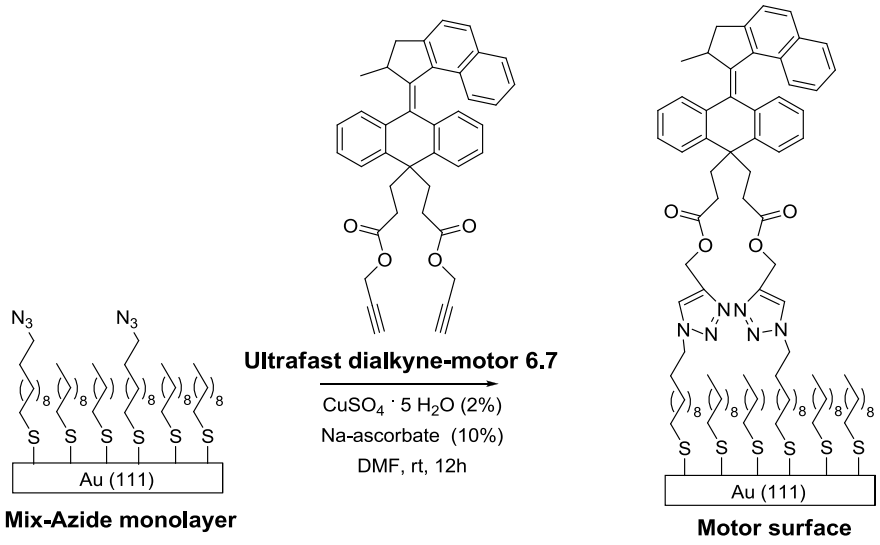

Figure 6.9. Scheme of the copper (I) catalysed 1,3-dipolar cycloaddition reaction to attach the ultrafast dialkyne-motor **6.7** to the azide monolayer on gold.

Contact angle measurements of the as-prepared mixed-azide functionalized surface gave a value of 68±1°, after the click reaction we observed a decrease in the contact angle to 64±2°, in agreement with reported values in the literature [14-16].

XPS measurements were performed in order to prove the surface attachment of the ultrafast dialkyne-motor **6.7**. The XPS characterization of the mixed monolayer proving the presence of the azide and the thiol bound to the gold surface was reported in Chapter 5 (see section 5.3.1c).

The N 1s core level XPS spectrum of the motor surface (see Figure 6.10) after the click reaction shows four components: the first three at binding energies of 400.4 eV, 401.2 eV and 402.0 eV, correspond to the three nitrogens of the triazole group. The forth peak at 405.5 eV corresponds to unreacted azides still present on the surface [10-13].

Several attempts were made to obtain UV/Vis and CD spectra of this surface but reproducibility problems did not allow us to prove the rotary motion of the light-driven molecular motor after surface attachment.

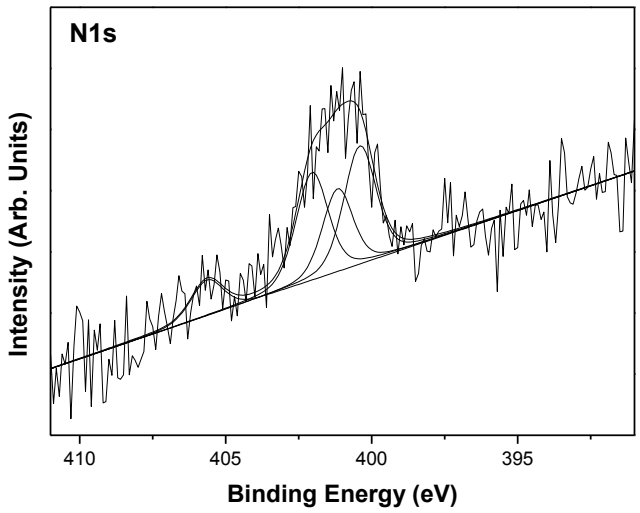

Figure 6.10. X-ray photoelectron spectrum of N 1s core level region of the motor surface after the click reaction.

6.5 Surface attachment: direct assembly

6.5.1 Diacid-motor 6.8 on silicon oxide

To improve the surface assembly and at the same time maximize the surface coverage, a direct assembly route was envisioned. The surface assembly of the motor on silicon oxide was performed *in situ* as described in detail in section 6.2.3c. Figure 6.11 illustrates the amidation reaction between diacid-motor **6.8** and the amine modified surface.

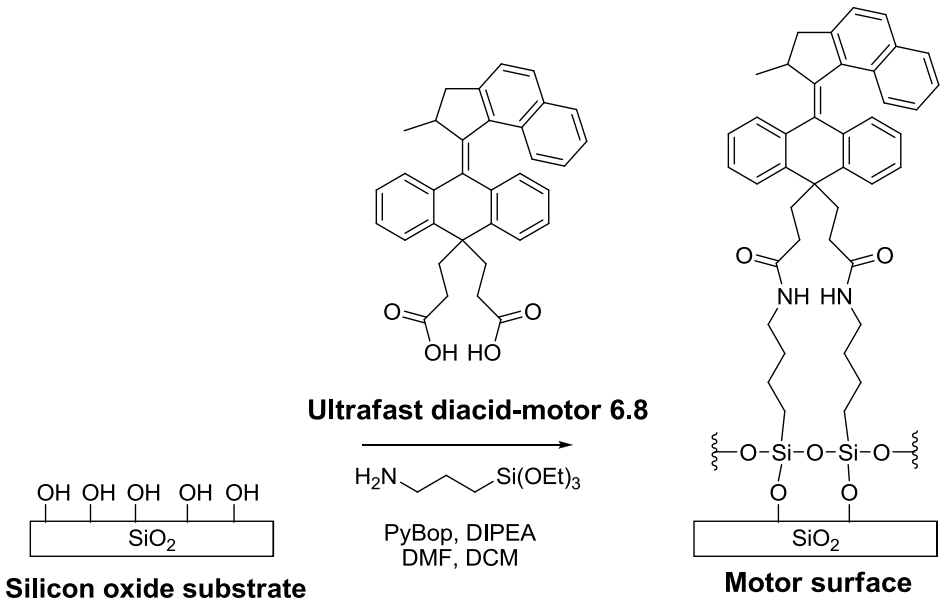

Figure 6.11. Scheme of the direct assembly on silicon oxide by *in situ* amidation of ultrafast diacid-motor **6.8**.

Figures 6.12, 6.13 and 6.14 show the results of the XPS analysis of the motor functionalized SiO_2 surface. Figure 6.12 corresponds to the spectrum of the Si 2p core level region, where we can assign three components as described in detail in Table 6.1. The peak at 103.3 eV corresponds to the silicon from the silicon oxide substrate. The two contributions at 102.6 eV and 104.1 eV are assigned to the silicon at the attachment point of the motor molecule which is bound to carbon and three oxygens, respectively [17]. This indicates the attachment of the motor to the surface.

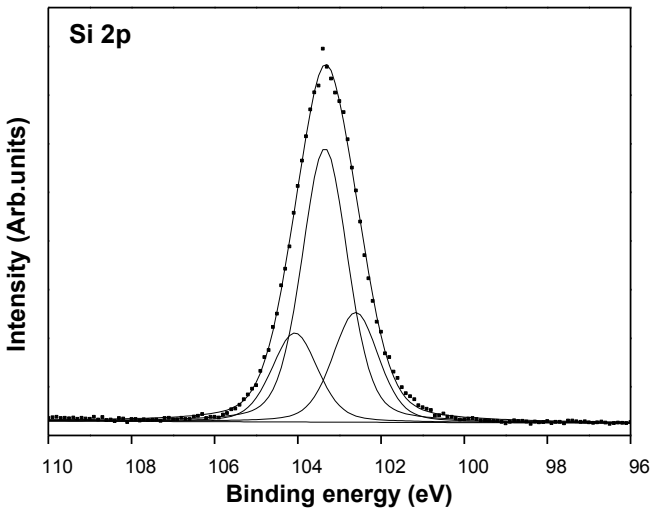

Figure 6.12. X-ray photoelectron spectrum of the Si 2p core level region of the motor surface on silicon oxide and fit of the experimental lines.

Binding energy	Relative area (sum = 100%)	Assignment
102.6 eV	23%	Si-C
103.3 eV	58%	SiO_2
104.1 eV	19%	SiO_3

Table 6.1. Components of the Si 2p core level photoemission line of the motor surface.

The peak at 401 eV in the N 1s core level photoemission spectrum in Figure 6.13 is due to the amide nitrogen from the *in situ* amidation reaction between the diacid-motor and the amine-leg. The carbon 1s XPS signals (Figure 6.14 and Table 6.2) match the overall structure of the motor assembled on the surface. The peak at 285 eV corresponds to the carbon in the phenyl groups. The contribution of aliphatic carbon is found at 285.8 eV, while the contribution at 286.5 eV stems from carbon bound to nitrogen in the amide group. The peak at 287.7 eV is attributed to the carbonyl groups and a final peak at 289 eV is assigned to shake-up satellites (explained in Chapter 2).

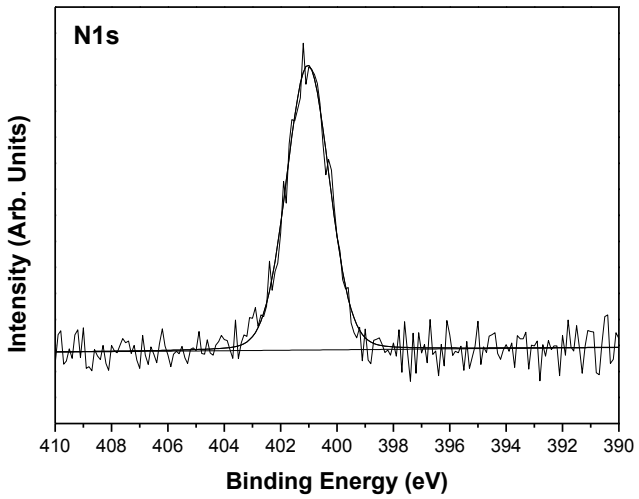

Figure 6.13. X-ray photoelectron spectrum of the N 1s core level region of the motor modified surface on silicon oxide and fit of the experimental line.

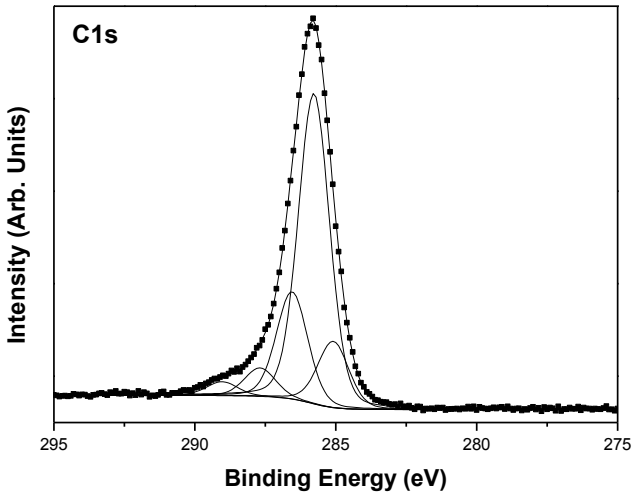

Figure 6.14. X-ray photoelectron spectrum of the C 1s core level region of the motor surface on silicon oxide and fit of the experimental lines.

Binding energy	Relative area (sum = 100%)	Assignment
285 eV	13%	-Phenyl
285.8 eV	59%	$-CH_2-$
286.5 eV	20%	C-N
287.7 eV	5%	C=O
289 eV	3%	Shake-up

Table 6.2. Components of the C 1s core level photoemission line of the surface modified with molecular motor.

The surface contact angle of the motor assembly was 67±2°, *i.e.* very similar to the motor assembly obtained via the click attachment method on the same surface [14-16]. From the surface analysis by XPS and contact angle measurements, we can conclude that the *in situ* amidation reaction worked and that the motor molecules were assembled on the surface.

UV/Vis spectroscopy was performed on a motor functionalized quartz surface. As shown in Figure 6.15 the UV/Vis spectrum revealed a typical motor absorption peak at λ_{max} = 350 nm. Irradiation with a 365 nm UV lamp showed no changes at room temperature.

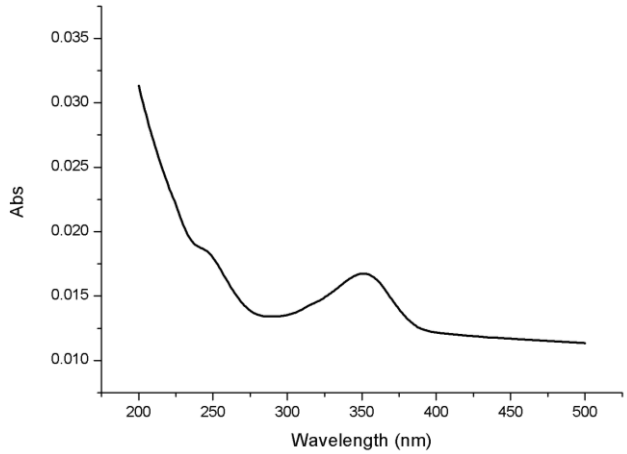

Figure 6.15. UV/Vis spectra of diacid-motor **6.8** on quartz surface after direct assembly by *in situ* amidation process.

Surface irradiation experiments of the motor-functionalized quartz surface were performed using the UV/Vis spectrometer equipped with a cryostat at 84 K, to prove the rotation of the light-driven rotary molecular motor after surface attachment. However, no changes were observed after thermal isomerization. The sensitivity of the spectrometer did not allow us to record spectra from the assembled surface, as it is very challenging to perform these experiments at such low temperatures.

In conclusion, we demonstrated that we have a motor monolayer on the silicon oxide surface but we were not able to perform UV/Vis and CD spectroscopy measurements to prove the rotary performance of the light-driven ultrafast molecular motors due to equipment limitations.

6.5.2 Dithiol-motor 6.10 on gold

Assembly of azide or alkyne monolayers via click chemistry on gold surfaces has been extensively studied. When considering a gold substrate thiol groups are always the easiest way to anchor a molecule. In the work presented here we attached a molecular motor with thiol-terminated legs to a gold substrate by self-assembly. The samples were prepared as explained in section 6.2.3b.

Figure 6.16 shows a schematic representation of the self-assembly process of the dithiol-motor **6.10** on a gold surface.

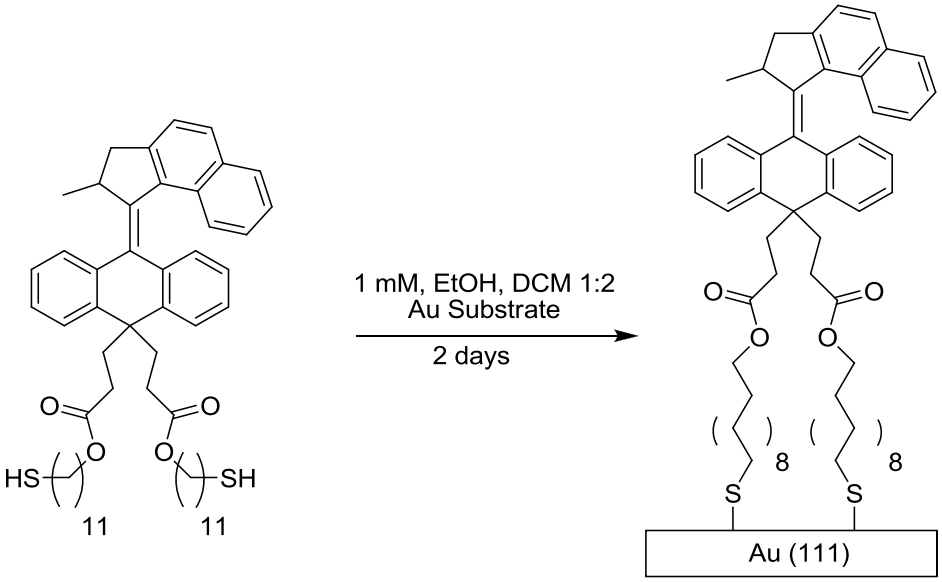

Figure 6.16. Scheme of the direct attachment of the dithiol-motor **6.10** on gold surfaces.

XPS measurements were carried out to find evidence for the dithiol-motor attachment to the gold surface. Figure 6.17 shows two components in the XPS spectrum of the S 2p core level region. The first one is peaked at a binding energy of 162.0 eV and originates from sulfur bound to gold. The second much smaller component at a binding energy of 164.1 eV stems from free thiol groups and therefore indicates the presence of unbound legs of the molecular motors [17-20]. Quantitative analysis of the XPS data reveals that 14% of the thiol groups have not reacted. Figure 6.18 shows the C 1s core level region for the motor functionalized surface. The peaks in the carbon region can be assigned as follows: the component at 285.1 eV corresponds to the phenyl rings in the motor, the one at 285.4 eV arises from aliphatic carbons, carbon-sulfur bonds contribute at 286.4 eV and the carbonyl groups in the legs of the motor are responsible for the spectral intensity at 287.8 eV.

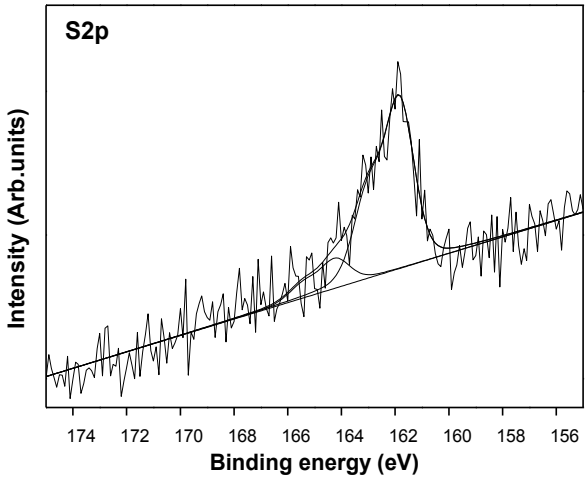

Figure 6.17. X-ray photoelectron spectrum of the S 2p core level region of the dithiol-motor **6.10** assembled on a gold substrate.

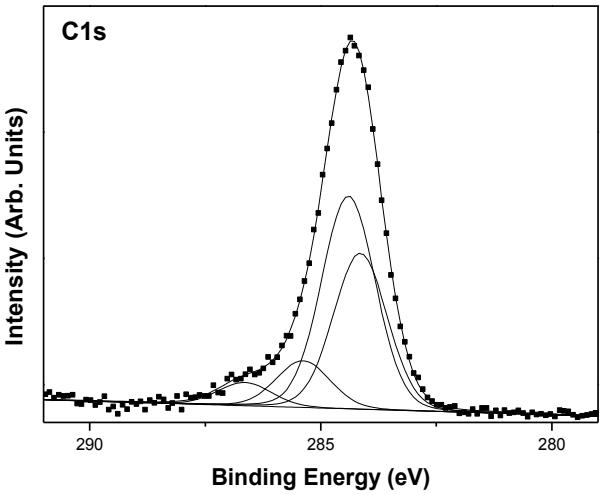

Figure 6.18. X-ray photoelectron spectrum of the C 1s core level region of the dithiol-motor **6.10** assembled on a gold substrate.

We can clearly state that a self-assembled monolayer of azimuthal molecular motors was formed. UV-vis spectroscopy was performed in order to verify if the motor is still able to rotate after surface attachment. For this purpose we prepared semitransparent gold on mica (see Chapter 2), and following the same procedure as for the samples discussed above, we prepared a self-assembled monolayer of dithiol-motor **6.10**.

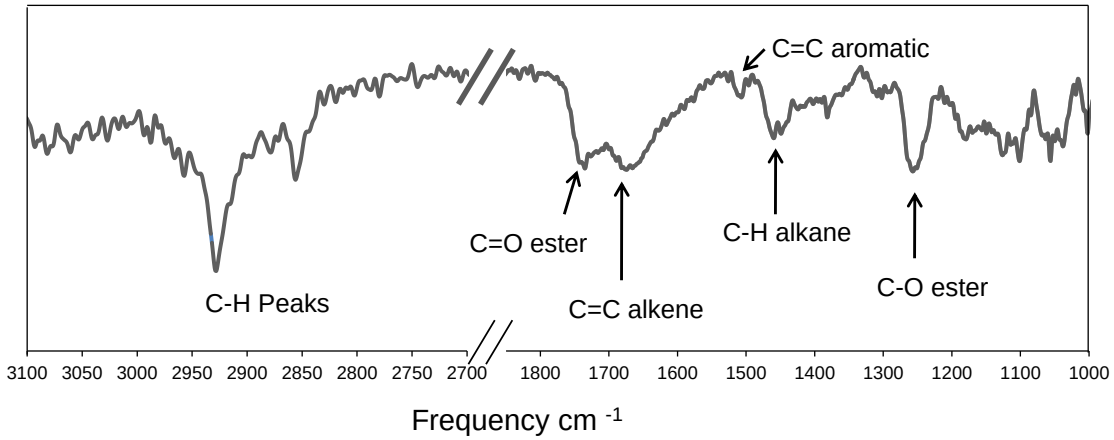

Figure 6.19. IR spectrum of the gold surface functionalized with dithiol-motor **6.10**.

After surface modification with the dithiol-motor **6.10** infrared spectroscopy confirmed the presence of the motor on the surface. The IR spectrum shown in Figure 6.19 can be assigned as follows: the band at 1250 cm^{-1} corresponds to the stretching mode of the C-O groups, the absorption band at 1450 cm^{-1} arises from the scissoring mode of the CH_2 groups, the symmetric stretching modes of aromatic C=C bonds appear at 1500 cm^{-1} and 1700 cm^{-1}, the band at 1750 cm^{-1} corresponds to the stretching mode of C=O, and finally the peaks at 2850 cm^{-1} and 2925 cm^{-1} can be assigned to the symmetric

and antisymmetric stretching modes of the C-H of the methyl groups, respectively. This clearly shows the fingerprint of the motor on the surface.

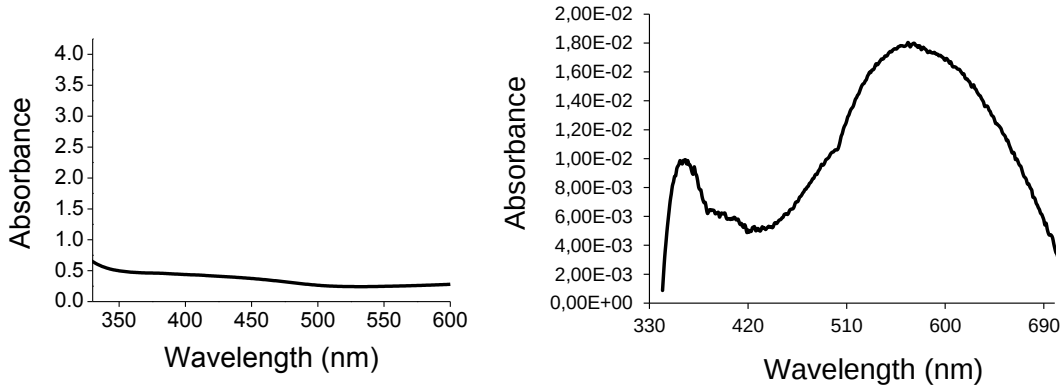

Figure 6.20. UV-vis spectra of the gold surface before (left) and after dithiol-motor **6.10** attachment (right).

Figure 6.20 shows the UV-vis spectra acquired before and after exposure of the Au surface to the solution with the motor molecules. The spectrum collected on the Au surface with the motors anchored to it is clearly different from that of the bare semitransparent gold surface. We then repeated the measurements after irradiating the surface for 30 min with UV light (365 nm, 253 K, N_2 atmosphere) and found the spectra obtained before and after irradiation were the same, which means that the upper half of the dithiol-motor **6.10** molecules did not undergo a rotation. We can attribute the loss in dynamic function to the fact that self-assembled monolayers of thiols are very dense. If we assume that the monolayer is well packed, the azimuthal molecular motor cannot perform the rotation of the upper half due to steric interactions [21].

A way to overcome this problem could be to create a mixed monolayer of molecular motors and alkanethiols, thereby increasing the space between the motor molecules to allow them to rotate after surface attachment.

6.6 Conclusions

Ultrafast motors were synthesized and using a variety of techniques, assembled on surfaces. Many synthetic routes and surface characterization techniques were explored. The in-depth analysis provides a useful guide for future surface motor assembly. Unfortunately the rotational behaviour of the ultrafast motor was not recorded, due to equipment limitations in some cases. For the only assembly where UV/Vis absorption spectrum could be recorded, no changes could be detected after irradiation with UV light pointing to a loss of dynamical function due to hindrance in the densely packed monolayer. Considering the utilization of functional nanomachines in the future, one needs to focus on control and accessibility; a slower motor that can be monitored and

controlled provides a brighter future perspective in terms of moving towards materials that are really useful.

6.7 Appendix: Synthesis of compounds (by Dr. T. Sasaki)

a) Motor 6.6 (basic structure)

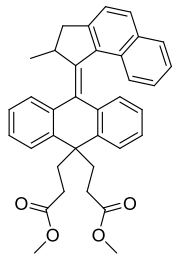

A solution of triphenylphosphine (80 mg, 0.305 mmol) and episulfide **5** (100 mg, 0.155 mmol) was heated in *p*-xylene (5 mL) at reflux for 14 h under inert atmosphere. The xylene was removed *in vacuo* and the material purified by flash chromatography (25% EtOAc:pentane) to give **6.6** as a white solid (89 mg, 94%). ^{1}H-NMR (400 MHz, $CDCl_3$) δ 7.92 (m, 1H), 7.71 (t, *J* = 7.0 Hz, 2H), 7.45 (m, 3H), 7.30 (m, 2H), 7.17 (t, 1H, *J* = 7.0 Hz), 7.11 (t, 1H, *J* = 8.0 Hz), 6, 89 (d, 1H, *J* = 7,7 Hz), 6.83 (t, *J* = 7.7 Hz, 1H), 6.75 (d, *J* = 7.0 Hz, 1H), 6.62 (t, *J*= XX Hz, 1H), 4.47 (quint, *J* = 6.2 Hz, 1H), 3.71 (s, 3H), 3.64 (dd, J_1 = 15.3 Hz, J_2 = 6.3 Hz, 1H), 3.45 (s, 3H), 2.81 (q, *J* = 8.6 Hz, 2H), 2.60 (d, *J* = 15.3 Hz, 1H), 2.46 (m, 4H), 2.18 (t, *J* = 6.3 Hz, 2H), 0.75 (d, *J* = 6.6 Hz, 3H); ^{13}C-NMR (100 MHz, $CDCl_3$) δ 174.3, 173.4, 146.0, 144.8, 141.2, 140.2, 139.6, 139.4, 135.7, 133.0, 129.8, 128.9, 128.3, 127.8, 127.5, 127.2, 126.4, 126.4, 126.4, 126.3, 126.1, 125.9, 125.7, 125.6, 125.3, 124.2, 124.0, 123.9, 51.6, 51.4, 46.8, 39.5, 37.7, 35.5, 30.4, 29.4, 27.4, 18.7.

b) Dialkyne-motor 6.7

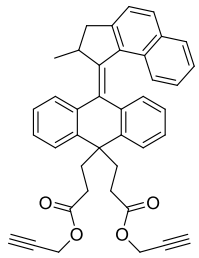

To a 2-necked round bottom equipped with a condenser was charged with **6.6** (250 mg, 0.471 mmol), freshly distilled propargylic alcohol (5 mL) and NaCN (10 mol%) was added. Under N_2, the solution was stirred to reflux overnight. After cooling it back to room temperature, the solution was passed through a short silica gel plug. The crude material was purified by flash chromatography (1:5 EtOAc:Heptane) to give a slightly yellowish solid (220 mg, 77%). ^{1}H-NMR (400 MHz, $CDCl_3$) δ 8.00 – 7.86 (m, 1H), 7.71 (dd, *J* = 8.0, 5.2 Hz, 2H), 7.44 (t, *J* = 7.6 Hz, 3H), 7.37 – 7.28 (m, 2H), 7.15 (td, *J* = 14.0, 6.9 Hz, 2H), 6.88 – 6.79 (m, 1H), 6.74 (t, *J* = 7.1 Hz, 1H), 6.69 – 6.54 (m, 2H), 4.72 (d, *J* = 2.5 Hz, 2H), 4.48 (m, 3H), 3.64 (dd, *J* = 15.6, 6.1 Hz, 1H), 2.82 (dd, *J* = 12.8, 7.2 Hz, 2H), 2.66 – 2.40 (m, 6H), 2.34 – 2.12 (m, 3H), 0.75 (d, *J* = 6.7 Hz, 3H). ^{13}C-NMR (100 MHz, $CDCl_3$) δ 173.3, 172.3, 146.4, 145.2, 141.3, 140.6, 139.6, 139.7, 136.0, 133.3, 130.2, 129.3, 128.6, 128.2, 128.1, 127.7, 127.6, 126.7, 126.5, 126.3, 125.9, 125.5, 124.6, 124.3, 124.23, 124.18, 75.2, 75.1, 74.94, 74.91, 52.3, 52.1, 47.1, 39.9, 38.0, 35.6, 30.7, 29.9, 29.7, 19.1.

c) Diacid-motor 6.8

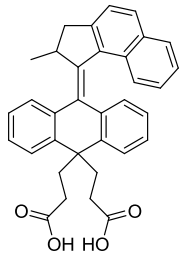

A solution of **6.6** (153 mg, 0.289 mmol) and LiOH (28 mg, 1.15 mmol) in a mixture of EtOH/H_2O/THF 1:1:1 (6 mL) was reflux for 3 h. The resulting solution was acidified with a 1 M solution of HCl (aq.) and the resulting precipitate was collected by filtration, washed with MeOH, Et_2O, and dried under vacuum to afford 100 mg (69%) as a white solid. ^{1}H-NMR (400 MHz, $CDCl_3$) *Peaks broadened due to hydrogen bond dimerization from acid legs and low solubility* δ 8.00 (1H), 7.79 (2H), 7.51 (3H), 7.33 (2H), 7.18 (2H), 6.65 (4H), 4.44 (1H), 3.66 (1H), 3.17 (1H), 2.75 (2H), 2.32 (4H), 1.95 (2H), 0.62 (3H).

d) Dithioacetate-motor 6.9

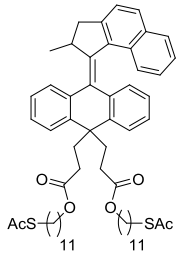

A mixture of diacid motor **6.8** (134 mg, 0.402 mmol), K_2CO_3 (222 mg, 1.605 mmol), and dry DMF (10 mL) was stirred at room temperature under inert atmosphere for 15 min. Then S-4-bromobutyl ethanethioate (373 mg, 1.206 mmol) and tetrabutylammonium iodide (100 mg) was added and the mixture was stirred at room temperature under inert atmosphere overnight. The resulting mixture was diluted with ethyl acetate and the organic layer was washed with brine, water and dried over sodium sulfate. The crude mixture was purified by flash chromatography (30% EtOAc/Hept) to afford **6.8** (339 mg, 88%) as a yellowish oil. ^{1}H-NMR (400 MHz, $CDCl_3$) δ 8.00–7.86 (m, 1H), 7.71 (dd, *J* = 8.0, 5.2 Hz, 2H), 7.44 (t, *J* = 7.6 Hz, 3H), 7.37 – 7.28 (m, 2H), 7.15 (td, *J* = 14.0, 6.9 Hz, 2H), 6.88 – 6.79 (m, 1H), 6.74 (t, 1H, *J* = 7.1 Hz), 6.69 – 6.54 (m, 2H), 4.72 (d, 2H, *J* = 2.5 Hz), 4.48 (m, 3H), 3.64 (dd, *J* = 15.6, 6.1 Hz, 1H), 2.82 (dd, *J* = 12.8, 7.2 Hz, 2H), 2.66 – 2.40 (m, 6H), 2.34–2.12 (m, 3H), 0.75 (d, *J* = 6.7 Hz, 3H). ^{13}C-NMR (100 MHz, $CDCl_3$) δ 173.3, 172.3, 146.4, 145.2, 141.3, 140.6, 139.6, 139.7, 136.0, 133.3, 130.2, 129.3, 128.6, 128.2, 128.1, 127.7, 127.6, 126.7, 126.5, 126.3, 125.9, 125.5, 124.6, 124.3, 124.23, 124.18, 75.2, 75.1, 74.94, 74.91, 52.3, 52.1, 47.1, 39.9, 38.0, 35.6, 30.7, 29.9, 29.7, 19.1.

e) Dithiol-motor 6.10

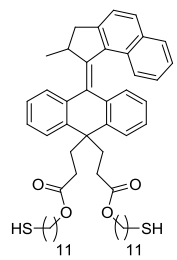

A solution of motor **6.9** (40 mg, 0.042 mmol), piperidine (1 ml), and methanol (10 mL) was stirred while heated at reflux overnight. The reaction mixture was cooled back to room temperature, solvent removed, and purified by flash column chromatography (25% EtOAc/Hept). The purified orange oil **6.10** (34 mg, 93%) solidified over time into a white solid. ^{1}H-NMR (400 MHz, $CDCl_3$) δ 8.00 – 7.86 (m, 1H), 7.71 (dd, *J* = 8.0, 5.2 Hz, 2H), 7.44 (t, *J* = 7.6 Hz, 3H), 7.37 – 7.28 (m, 2H), 7.15 (td, *J* = 14.0, 6.9 Hz, 2H), 6.88 – 6.79 (m, 1H), 6.74 (t, *J* = 7.1 Hz, 1H), 6.69 – 6.54 (m, 2H), 4.72 (d, *J* = 2.5 Hz, 2H), 4.48 (m, 3H), 3.64 (dd, *J* = 15.6, 6.1 Hz, 1H), 2.82 (dd, *J* = 12.8, 7.2 Hz, 2H), 2.66 – 2.40 (m, 6H), 2.34 – 2.12 (m, 3H), 0.75 (d, *J* = 6.7 Hz, 3H). ^{13}C-NMR (100

MHz, $CDCl_3$) δ 173.3, 172.3, 146.4, 145.2, 141.3, 140.6, 139.6, 139.7, 136.0, 133.3, 130.2, 129.3, 128.6, 128.2, 128.1, 127.7, 127.6, 126.7, 126.5, 126.3, 125.9, 125.5, 124.6, 124.3, 124.23, 124.18, 75.2, 75.1, 74.94, 74.91, 52.3, 52.1, 47.1, 39.9, 38.0, 35.6, 30.7, 29.9, 29.7, 19.1.

6.8 References

1. D. H. Waldeck, *Chem. Rev.* **1991**, *91*, 415.
2. H. Meier, *Angew. Chem.,Int. Ed.* **1992**, *31*, 1399.
3. R. W. J. Zijlstra, P. T. van Duijnen, B. L. Feringa, T. Steffen, K. Duppen, D. A. Wiersma, *J. Phys. Chem. A* **1997**, *101*, 9828.
4. W. Schuddeboom, S. A. Jonker, J. M. Warman, M. P. de Haas, M. J. W. Vermeulen, W. F. Jager, B. de Lange, B. L. Feringa, R. W. Fessenden, *J. Am. Chem. Soc.* **1993**, *115*, 3286.
5. J. Conyard, K. Addison, I. A. Heisler, A. Cnossen, W. R. Browne, B. L. Feringa, S. R. Meech, *Nature Chem.* **2012**, *4*, 547.
6. M. Klok, "*Motors for use in molecular nanotechnology"*, Ph.D. thesis, University of Groningen, **2009**.
7. V. Sundström, T. Pullerits,R. van Grondelle, *J Phys Chem B* **1999**, *103*, 2327.
8. R. Berera, R. van Grondelle, J. T. M. Kennis, *Photosynth. Res.* **2009**, *101*, 105.
9. J.P. Collman, N.K. Devaraj, T.P.A. Eberspacher, C.E.D. Chidsey, *Langmuir* **2006**, 2457.
10. London, G., Carroll, G.T., Fernández Landaluce, T., Pollard, M.M., Rudolf, P., Feringa, B.L., *Chem. Commun.* **2009**, *13*, 1712.
11. J. P. Collman, N. K. Devaraj, T.P.A. Eberspacher, C.E.D. Chidsey, *Langmuir* **2006**, 2457.
12. E.W. Wollman, D. Kang, C.D. Frisbie, I.M. Lorkovic, M.S. Wrighton, *J. Am. Chem. Soc.* **1994**, 4395.
13. A. Devadoos, C.E.D. Chidsey, *J. Am. Chem. Soc.* **2007**, *129*, 5370.
14. S. Prakash, T. M. Long, J. C. Selby, J. S. Moore, M. A. Shannon, *Anal. Chem.* **2007**, *79*, 1661.
15. G. E. Fryxell, P. C. Rieke, L. L. Wood, M. H. Engelhard, R. E. Williford, G. L. Graff, A. A. Campbell, R. J. Wiacek, L. Lee, A. Halverson, *Langmuir* **1996**, *12*, 5064.
16. A. Heise,M. Stamm, M. Rauscher, H. Duschner, H. Menzel, *Thin Solid Films* **1998**, *199*, 327.
17. J. F. Moulder, W. F. Stickle, P. E. Sobol, K. D. Bomben, *"Handbook of X-ray photoelectron Spectroscopy"*, **1995**, Physical Electronics Inc. Eden Prairie, Minnesota.
18. P. E. Laibinis, C. D. Bain, G. M. Whitesides, *J. Phys. Chem.* **1997**, *95*, 7017.
19. A.-S. Duwez, *J. Electron Spectrosc. Relat. Phenom.* **2004**, *134*, 97.
20. R. Arnold, W. Azzam, A. Terfort, C. Wöll, *Langmuir* **2002**, *18*, 3980.
21. H. Logtenberg, *"Molecular systems for smart materials: Spectroscopic and electrochemical studies, from solution to surfaces"*, Ph.D. thesis, University of Groningen, **2013**.

Summary

Biomolecular motors are omnipresent in nature where they are used for different tasks. Much of the mechanical work in biological systems is performed by supramolecular structures using the coherent motion of these motors. The grafting of biological or synthetic rotary motors onto solid substrates is considered to be a key step towards the fabrication of nanomechanical devices that exploit the rotational motion generated by the action of these molecules. To mimic these biological systems, synthetic molecular motors are molecular machines capable of rotation under energy input; in the case of light-driven molecular rotors this energy input is light.

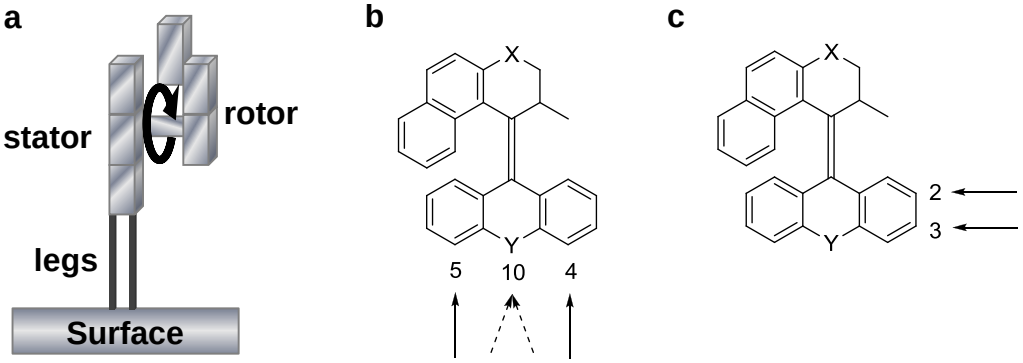

Figure 1. Scheme of a rotary molecular motor (a). Azimuthal (b) and altitudinal (c) substitution pattern on second generation molecular motors.

Our research focused on synthetic light-driven unidirectional molecular rotary motors based on over-crowded alkenes that undergo photoisomerization followed by thermal helix inversion. In pursuit of designing systems that can use the photo-induced rotary movement, one half of the motor is attached to the surface of a gold or silicon substrate. In such systems different orientations of the rotating part (rotor) relative to the stationary part (stator) can be envisioned. In altitudinal motors the axis of rotation is parallel to the surface, while in azimuthal it is perpendicular to the surface (Figure 1).

A major hurdle to apply such systems to perform complex tasks is to develop a versatile and stable method to graft them onto surfaces. “Click chemistry” reactions are expected to be a useful tool for functionalization of surfaces with rotary molecular motors. The term “click chemistry” refers to copper (I) catalysed 1,3-dipolar cycloadditions in which an azide and an alkyne form a five-membered ring (Figure 2). In this thesis we investigate surface attachment of altitudinal and azimuthal rotary molecular motors via click chemistry reactions.

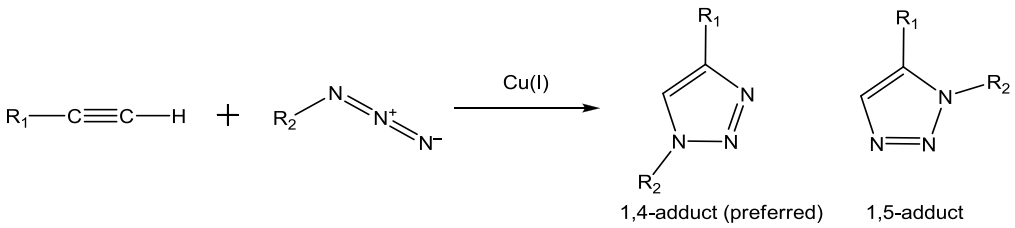

Figure 2. General scheme of 1,3 dipolar cycloaddition ("click reaction").

As the molecular structure and function of the rotor is controlled by UV irradiation and the rotor function has to be exploited on a solid surface, the stability of the surface-anchoring part for the rotor under UV irradiation needs be demonstrated. We found that the azide-terminated self-assembled monolayers on gold and on silicon oxide without molecular motors are stable for at least 1 hour under UV-light and this proves that these systems provide indeed a promising surface for copper (I) catalysed 1,3-dipolar cycloadditions reactions. Crucially a combination of surface analysis techniques demonstrates the success of the interfacial reaction as well as the fact that the surface-bound motors preserve their light-induced rotary movement. Although we focused on gold and silicon substrates, this facile procedure is expected to be suitable also for other materials, including polymers, gels and various self-assembled systems.

We demonstrated that molecular motors can be grafted to surfaces via “click reaction” of azides with alkynes. Altitudinal dialkyne-motors were successfully grafted on gold and silicon oxide surfaces, previously covered with an azide-terminated self-assembled monolayer. After surface attachment the motor surface preserved the rotary function. This grafting method can therefore be considered a versatile approach to assemble motors on surfaces. We also attempted the direct assemble of altitudinal dialkyne-motors via acetylenyl-anchoring to the gold surface, but it was not successful for these molecules. Direct attachment of altitudinal diol-motors on silicon oxide using chlorinated functionalized surfaces was difficult to reproduce and not suitable for routine use.

We also compared two routes for surface attachment of azimuthal light-driven molecular motors. The first pathway is based on the “click” chemistry between azide-modified surfaces either on silicon oxide or gold with alkyne-legged motor. The second pathway is the direct attachment route. While the number of synthetic steps is increased the attachment is more direct, meaning that simple literature-based conditions are enough to graft the molecules to the surface as long as the correct legs are synthesized. Direct self-assembly of thiols on gold and of silanes on silicon oxide is reported here as new routes for surface attachment of rotary molecular motors.

In this thesis many synthetic routes and surface characterization techniques were explored. The in-depth analysis provides a useful guide for future surface motor assembly. Considering the utilization of functional nanomachines in the future, one needs to focus on control and accessibility; a slower motor that can be monitored and controlled provides a brighter future perspective in terms of moving towards materials that are really useful.

Samenvatting

Biomoleculaire motoren zijn alom aanwezig in de natuur waar ze gebruikt worden voor verschillende taken. Het merendeel van de mechanische arbeid in biologische systemen wordt uitgevoerd door supramoleculaire structuren gebruikmakend van de coherente beweging van deze motoren. Het koppelen van biologische of synthetische roterende motoren op solide oppervlakken wordt beschouwd als een cruciale stap op weg naar de fabricatie van nanomechanische apparaten die een voordeel halen uit de rotationele beweging gegenereerd door de werking van deze moleculen. Om deze biologische systemen te simuleren, maakt men gebruik van synthetische moleculaire motoren, hetgeen moleculaire motoren betreft met de mogelijkheid te roteren indien er een energetische stimulans plaatsvindt; in het geval van licht- aangedreven moleculaire rotoren is deze energiebron licht.

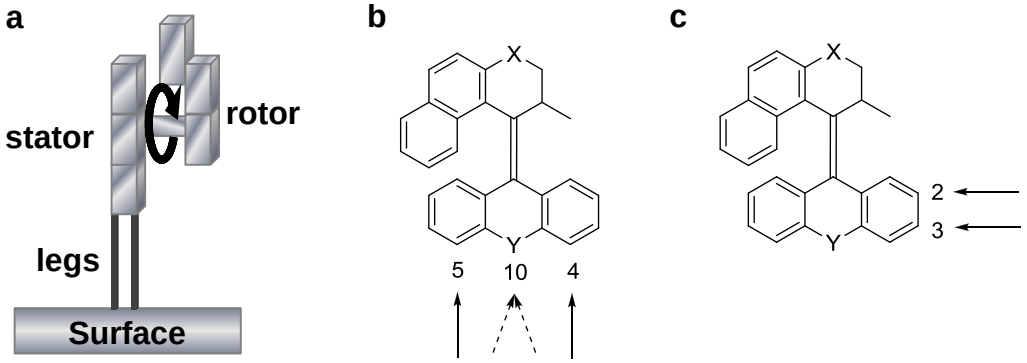

Figuur 1. Schema van een roterende moleculaire motor (a). Verticaal (b) en horizontaal (c) substitutiepatroon in tweede generatie moleculaire motoren.

Dit onderzoek richtte zich op synthetische lichtaangedreven éénrichtings roterende moleculaire motoren gebaseerd op een overpopulatie van alkenen die fotoisomerisaties ondergaan, gevolgd door thermische helix-inversie. Met het oog op het ontwikkelen van systemen, gebruikmakend van foto-geïnduceerde rotaties, is één helft van de motor gekoppeld aan een goud -of siliciumoppervlak. In zulke systemen kunnen verschillende oriëntaties van het roterende deel (rotor) ten opzichte van het statische deel (stator) beoogd worden. Voor verticaal roterende motoren bevindt de rotatie-as zich parallel aan het oppervlak, terwijl deze voor horizontaal roterende motoren loodrecht op het oppervlak gepositioneerd is (Figuur 1).

Een belangrijke horde die genomen moet worden alvorens dergelijke systemen toe te kunnen passen voor het uitvoeren van complexe taken is de ontwikkeling van een veelzijdige en stabiele methode voor de koppeling van deze moleculaire motoren aan oppervlakken. Het toepassen van “klik-chemische” reacties wordt verwacht een handig middel te zijn om de functionalisatie van oppervlakken met roterende moleculaire motoren te verwezenlijken. De term “klik-chemie” verwijst hierbij naar koper (I)

gekatalyseerde 1,3-dipolaire cycloaddities waarin een azide en alkyne een vijf-ledige ring vormen (Figuur 2). In deze thesis onderzoeken we de koppeling van verticaal en horizontaal roterende moleculaire motoren aan oppervlakken via “klik-chemische” reacties.

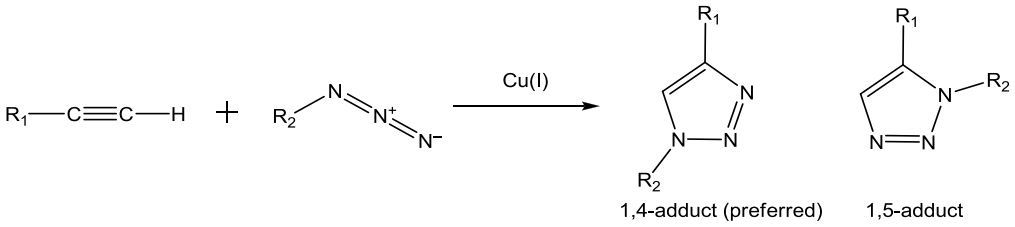

Figuur 2. Algemeen schema van een 1,3-dipolaire cycloadditie ("klik reactie").

Aangezien de moleculaire structuur en functie van de rotor gecontrolleerd wordt door UV bestraling en het voordeel van de rotorfunctie gehaald kan worden aan een solide oppervlak, moet de stabiliteit van het aan het oppervlak gekoppelde verbindingsdeel, de stator, onder UV bestraling aangetoond worden. In dit werk is aangetoond dat de azide-getermineerde zelf-assemblerende monolagen op goud en siliciumoxide, in afwezigheid van moleculaire motoren, stabiel blijven voor minstens 1 uur onder UV bestraling, hetgeen bewijst dat deze systemen inderdaad een veelbelovend oppervlak bieden voor koper (I) gekatalyseerde 1,3-dipolaire cycloadditie reacties. Een doorslaggevende factor is de combinatie van oppervlakte analyse technieken die zowel het succes van de intermediaire reacties aantonen alsook het feit dat de oppervlak-gebonden motoren hun licht-geïnduceerde rotatiebeweging behouden. Hoewel de focus op goud -en siliciumoppervlakken lag, is de verwachting dat deze eenvoudige procedure ook geschikt is voor andere materialen, inclusief polymeren, gels en verscheidene zelf-assemblerende systemen.

Voorts is aangetoond dat moleculaire motoren gekoppeld kunnen worden aan oppervlakken via een “klik reactie” van azides met alkynen. Verticaal roterende dialkyne-motoren zijn met success gekoppeld aan goud en siliciumoxide oppervlakken, dewelke vooraf gecoat zijn met een azide-getermineerde zelf-assemblerende monolaag. Na de oppervlakte-koppeling behield de motor zijn roterende functie. Deze koppelingsmethode mag daarom beschouwd worden als een veelzijdige aanpak om motoren op oppervlakken aan te brengen. Eveneens is er getracht om verticaal roterende dialkyne-motoren rechtstreeks aan te brengen op het goudoppervlak via acetylenyl-verankering in het goudoppervlak, maar deze aanpak kon niet succesvol worden bevonden voor dergelijke moleculen. Rechtstreekse koppeling van verticaal roterende diol-motoren op siliciumoxide, gebruikmakend van gechloreerde gefunctionaliseerde oppervlakken, bleek lastig te reproduceren en is daarom niet geschikt voor standaard gebruik.

Twee mogelijke methodes voor oppervlakte-koppeling van horizontaal roterende lichtaangedreven moleculaire motoren hebben we verder met elkaar vergeleken. De

eerste methode is gebaseerd op de “klik chemie” tussen azide-gemodificeerde oppervlakken op hetzij siliciumoxide, hetzij goud met alkyne-benige motoren. De tweede methode betreft de rechtstreekse koppeling. Hoewel het aantal synthetische stappen toeneemt, is de koppeling directer, hetgeen betekend dat eenvoudige literatuur-gebaseerde condities volstaan om de moleculen aan het oppervlak te koppelen ten minste indien de juiste “benen” gesynthetiseerd worden. Het rechtstreekse zelf-assembleren van thiolen op goud en van silanen op siliciumoxide wordt hier gerapporteerd als nieuwe methodes leidend tot de oppervlakte-koppeling van roterende moleculaire motoren.

In deze thesis zijn meerdere synthetische methodes en oppervlakte karakterisatie technieken geëxploreerd. De diepgaande analyse levert een handige gids op voor het tot stand komen van toekomstige oppervlakte motoren. Betreffende het gebruik van functionele nanomachines in de toekomst is het van belang om aandacht te besteden aan de controle en toegankelijkheid van de methodes; een langzamere motor waarop men kan toezien en controle kan uitoefenen, zal resulteren in een helderder toekomst perspectief betreffende een verschuiving naar materialen die echt bruikbaar zijn.

Acknowledgements-Agradecimientos

I would like to thank the people that helped me throughout the four years and a half that I spend in Groningen doing my Ph.D.

First of all I would like to thank my promotors Prof. Petra Rudolf and Prof. Ben L. Feringa for giving me the opportunity of working in a challenging project. Thank you for all the scientific discussions, the support and the guidance to finalize this thesis. I would like to thank specially Petra for her daily supervision and her “open door policy”; you are always available for your group members.

I am grateful to the members of the reading committee: Prof. Steven De Feyter, Prof. Wybren Jan Buma and Prof. Katharina J. Franke for their willingness to read and approve this thesis.

There are many people that helped me to pursuit all the results presented in this dissertation. Most of the work in this thesis was done with the assistance and collaboration of Gábor London, thank you for your hard work, all the hours in the lab and the scientific discussions, we did a good job! I would also like to thank Dr. Takashi Sasaki with whom I worked to obtain all the results in Chapter 6 of this thesis. I am very thankful to Peter van Abswoude who did his bachelor thesis project with me and some of his results are part of Chapter 4 in this thesis.

Doing a Ph.D. is a learning process and I had the pleasure to learn from two remarkable people, Dr. Michael M. Pollard and Dr. Monika Lubomska. Mike, you left us too early, but your guidance and knowledge will never be forgotten. Monika, thanks for sharing all your knowledge with me, you were a great mentor.

During my Ph.D. I was working within two groups, the group of Surfaces and Thin Films and the group of Synthetic Organic Chemistry; in those two groups I met an incredible amount of amazing people that made my life in Groningen unforgettable. Thank you all!

Es difícil expresar en palabras la cantidad de maravillosos momentos que he vivido durante mi estancia en Groningen. A nivel personal ha sido una experiencia inolvidable e increíblemente enriquecedora que nunca olvidaré. Todo gracias a las increíbles personas que he conocido y las innumerables vivencias que he tenido el placer de compartir. A todos vosotros, gracias de todo corazón.

Por último gracias a mi familia, son ya muchos años lejos de vosotros, pero siempre estáis ahí. La distancia no es el olvido, os tengo presentes cada día.

Tatiana

List of Publications

C.M. Whelan, A.-C. Demas, A. Romo Negreira, T. Fernández Landaluce, J. Schuhmacher, L. Carbonell, and K. Maex, "Surface engineering using self-assembled monolayers: model substrates for atomic-layer deposition," in Materials for Information Technology, Eds. E. Zschech, C. Whelan, and T. Mikolajick, Springer-Verlag (London) Ltd. **2005**. Book chapter.

A. Martin Hoyas, J. Schuhmacher, C. M. Whelan, T. Fernández Landaluce, D. Vanhaeren, and K. Maex, "Using scaling laws to understand the growth mechanism of atomic layer deposited WNxCy films on methyl-terminated surfaces," *J. Appl. Phys.* **2006**, *100*, 4903.

Y. Zhang, A. A. Broekhuis, M. C. A. Stuart, T. Fernández Landaluce, D. Fausti, P. Rudolf and F. Picchioni, "Cross-Linking of Multiwalled Carbon Nanotubes with Polymeric Amines," *Macromolecules* **2008**, *41*, 6141.

P. Wesenhagen, J. Areephong, T. Fernández Landaluce, N. Heureux, N. Katsonis, J. Hjelm, P. Rudolf, W. R. Browne and B. L. Feringa, "Photochromism and electrochemistry of a dithienylcyclopentene electroactive polymer," *Langmuir* **2008**, *24*, 6334.

T. Fernández Landaluce, G. London, G.T. Carroll, M. M. Pollard, B. L. Feringa and P.Rudolf, "From windmill to nanomill: altitudinal molecular motors on surfaces," *SynForm* **2008**, 11, A124.

G. London, G.T. Carroll, T. Fernández Landaluce, M. M. Pollard, P.Rudolf and B. L. Feringa, "Light-Driven Altitudinal Molecular Motors on Surfaces," *Chem. Commun.* **2009**, *13*, 1712.

W. van Zoelen, S. Bondzic, T. Fernández Landaluce, J. Brondijk, K. Loos, A.-J. Schouten, P. Rudolf and G. ten Brinke, "Nanostructured polystyrene-block-poly(4-vinyl pyridine)(pentadecylphenol) thin films as templates for polypyrrole synthesis," *Polymer* **2009**, *50*, 3617.

T. Kudernac, N. Saendig, T. Fernández Landaluce, B. J. van Wees, P. Rudolf, N.Katsonis, F. Zerbetto and B. L. Feringa, "Intermolecular repulsion through interfacial attraction: towards engineering of polymorphs," *J. Am. Chem. Soc.* **2009**, *131*, 15655.

T. Fernández Landaluce, G. London, M. M. Pollard, P.Rudolf and B. L. Feringa, "A faster rotary molecular motor: A large increase in speed through a small change in design," *J. Org. Chem.* **2010**, *75*, 5323.

G. T. Carroll, G. London, T. Fernández Landaluce, P. Rudolf and B. L. Feringa, "Adhesion of Photon-driven Molecular Motors to Surfaces via 1,3-Dipolar Cycloadditions: Effect of Interfacial Interactions on Molecular Motion," *ACS Nano* **2011**, *5*, 622.